Clemson University
TigerPrints

All Theses Theses

8-2011

A HISTORY-DEPENDENT NONWETTING PHASE TRAPPING MODEL FOR MULTIPHASE FLOW CHARACTERISTIC CURVES

Christopher Patterson
Clemson University, patter6@clemson.edu

Follow this and additional works at: http://tigerprints.clemson.edu/all_theses

Part of the Environmental Engineering Commons

Recommended Citation
Patterson, Christopher, "A HISTORY-DEPENDENT NONWETTING PHASE TRAPPING MODEL FOR MULTIPHASE FLOW CHARACTERISTIC CURVES" (2011). *All Theses.* Paper 1188.

This Thesis is brought to you for free and open access by the Theses at TigerPrints. It has been accepted for inclusion in All Theses by an authorized administrator of TigerPrints. For more information, please contact awesole@clemson.edu.

A HISTORY-DEPENDENT NONWETTING PHASE TRAPPING MODEL FOR MULTIPHASE FLOW CHARACTERISTIC CURVES

A Thesis
Presented to
the Graduate School of
Clemson University

In Partial Fulfillment
of the Requirements for the Degree
Master of Science
Hydrogeology

---

by
Christopher Patterson
August 2011

Accepted by:
Dr. Ronald W. Falta, Committee Chair
Dr. Lawrence C. Murdoch
Dr. D. E. Stevenson
Scott E. Brame

ABSTRACT

Characteristic curves used in numerical multiphase flow simulators describe relative permeability-saturation and capillary pressure-saturation relationships for flow simulations. Characteristic curves are typically non-hysteretic; meaning they are monotonic functions of saturation and are limited to a single value for residual saturation. Implications of residual saturation are important for environmental, petroleum, and geologic carbon sequestration modeling. However, hysteretic characteristic curves predict that trapped residual saturation depends on the local saturation history. The use of hysteretic characteristic curves is critical to predicting the residual saturation and ultimately the mobility of a nonwetting phase such as supercritical CO_2 or a nonaqueous phase liquid (NAPL). Previous hysteretic formulations often have discontinuous derivatives of relative permeability and capillary pressure at turning point saturations, which can cause numerical difficulties during Newton-Raphson iterations. A straight forward hysteretic model for nonwetting phase trapping is presented and assessed by comparison to both experimental and published simulation results. This constitutive model produces smooth, continuously differentiable relative permeability and capillary pressure curves at drainage-imbibition turning points, which eases numerical performance during the Newton-Raphson iteration technique used to solve the non-linear governing equations used to analyze multiphase flow. In addition, hysteresis is included in the characteristic functions without requiring any additional parameters. An assessment of the new model is made by simulating an experiment published by Johnston and Adamski (2005) that explored the relationship of residual- and maximum- non-

wetting phase saturations using an undisturbed soil sample. Another assessment is made by comparing the results of the new model to an analysis by Doughty (2007) when simulating the injection and migration of a supercritical CO_2 plume in a deep storage formation. The simulated results compare favorably and confirm that the new model can duplicate essential features of more complicated hysteretic models.

DEDICATION

My mother and father have supported me throughout my entire life, and without that support I would have never had the opportunity to achieve what I have achieved today. Other family members Jeffrey, Kimberly, and Kelly have always been a source of enjoyment and love.

I can always count on friends Elizabeth and Jason for support and balance in life. I am grateful for Charles and Frank who continuously encourage me regardless of the distance between us. Friends like these are invaluable and I consider them to also be a part of my family.

With love and gratitude, this thesis is dedicated to my family.

ACKNOWLEDGMENTS

I'd like to express profound appreciation to Dr. Ronald Falta for his patience with me throughout the course of this project. His knowledge and character inspired me to undertake a task of such high stature. It was a distinct privilege to receive guidance from him. I'd also like to thank Dr. Larry Murdoch for the inspiration he provided during my years at Clemson University. I hold the expertise of both Dr. Falta and Dr. Murdoch in the highest regard.

I am indebted to Christine Doughty of Berkeley Lab's Earth Sciences Division for contributing the means necessary for the two-dimensional simulations presented in this thesis and for her invaluable assistance through some of the complications of this research project. I'd also like to thank Colin Johnston of CSIRO, Australia, for contributing laboratory data essential to the model assessment presented in this thesis.

Special thanks to fellow student Catherine Ruprecht for introducing me to the geospatial modeling capabilities of iTOUGH2-GSLIB. I am also thankful to David Hisz for his support throughout many aspects of my research.

I'd like to acknowledge Dr. Eugene Perry and Dr. Melissa Lenczewski at Northern Illinois University for advising me as an undergraduate student and first introducing me to the world of scientific research.

I'd also like to thank Mr. Randy Locke at the Illinois State Geological Survey in Champaign, IL for his understanding and the accommodations he has made during my first weeks working with him.

This work was supported by the U.S. EPA STAR Grant # 834383.

TABLE OF CONTENTS

Page

TITLE PAGE i

ABSTRACT ii

DEDICATION iv

ACKNOWLEDGMENTS v

LIST OF TABLES viii

LIST OF FIGURES x

CHAPTER

I. INTRODUCTION 1

1.1 Mechanisms for trapping CO_2 2
1.2 Characteristic curves 4
1.3 Hysteretic characteristic curves 10
1.4 Motivation and purpose of study 14

II. OBJECTIVES AND APPROACH 15

III. MATHEMATICAL METHODS 16

3.1. Relative permeability models 16
3.2 Capillary pressure models 17
3.3 Calculation of residual saturation 18
3.4 Hysteretic extensions to characteristic curves 21
3.5 New hysteretic model 28

IV. NUMERICAL SIMULATORS AND NEW MODEL IMPLEMENTATION 38

4.1 Governing equations 38
4.2 New model implementation into TOUGH2 40

Table of Contents (Continued)

Page

V. MODEL ASSESSMENT 41

5.1 One-dimensional simulations 41
5.2 Two-dimensional simulations 49
5.3 Three-dimensional simulations 71
5.4 Recommended work 88

VI. CONCLUSIONS 89

REFERENCES 90

LIST OF TABLES

Table Page

3.1 Model parameters for the non-hysteretic relative permeability curves used in figure 1.1. 18

3.2 Parameters for van Genuchten capillary pressure curve used in figure 1.3. 19

3.3 Hysteretic non-wetting phase relative permeability curve parameters used in figure 3.2. 23

3.4 Hysteretic capillary pressure curve parameters used in figure 3.3. 24

3.5 Relative permeability curve parameters used in figure 3.5. 31

3.6 Hysteretic relative permeability curve parameters used in figure 3.6. 34

3.7 Hysteretic relative permeability curve parameters used in figure 3.7. 35

3.8 Hysteretic capillary pressure curve parameters used in figure 3.8. 36

3.9 Hysteretic non-wetting phase capillary pressure curve parameters used in figure 3.9. 37

5.1 Model parameters for the materials used to simulate experiment by Johnston and Adamski (2005). 45

5.2 Characteristic curve parameters for the material types used in the simulation of Johnston and Adamski (2005). 46

5.3 Hysteretic capillary pressure curve parameters for both the fitted curve and the curve used in Doughty (2007). 54

List of Tables (Continued)

Table Page

5.4 Hysteretic relative permeability curve parameters for both the fitted curve and the curve used in Doughty (2007). 54

5.5 Hydraulic properties for the materials used in the 3-dimensional model. 72

5.6 Non-wetting phase relative permeability curve parameters for the 3 3-dimensional simulation cases. 74

LIST OF FIGURES

Figure Page

1.1 Examples of non-hysteretic relative permeability curves by Mualem (1976). The two curves are modeled using an S_{nr} value of 0 (solid line) and another with an S_{nr} value of 0.25 (dashed line)..... 6

1.2 Example of a wetting phase relative permeability curve. The wetting phase is immobile ($k_{rw} = 0$) at $S_w = S_{lr}$. 7

1.3 Non-hysteretic capillary pressure curves from van Genuchten (1980) showing aqueous phase saturation as a function of capillary pressure (P_c)..... 9

1.4 A hysteretic non-wetting phase relative permeability curve from Doughty (2007). The numerical model will follow the main drainage branch upwards during wetting phase drainage, and will follow a secondary imbibition path downwards during wetting phase imbibition. The path of the imbibition branch depends on the turning-point saturation. This example shows multiple potential turning-points each with a separate imbibition branch. The value of S_{nr} is represented by ($1-S_w$) at $k_{rn} = 0$. 12

1.5 A hysteretic version of van Genuchten (1980) capillary pressure curve. The numerical model will follow the main drainage branch upwards during wetting phase drainage, but will follow a secondary imbibition path downwards during wetting phase imbibition. The path of the imbibition branch depends on the turning-point saturation. This example shows multiple potential turning-points each with a separate imbibition branch. The value of S_{nr} is represented by ($1-S_w$) at $P_c = 0$..... 13

3.1 Plot of Snr vs Snmax for both the Land (1968) trapping model (solid line) and the linear trapping model (dashed line). The maximum S_{nr} value is 0.25..... 20

List of Figures (Continued)

Figure Page

3.2 Example of a hysteretic non-wetting phase relative permeability function used by Doughty (2007). Multiple potential wetting phase imbibition branches are shown for arbitrary turning-point saturations. 22

3.3 Hysteretic capillary pressure curve from Kaluarachchi and Parker (1992) showing multiple imbibition branches for arbitrary turning-point saturations. 24

3.4 Example of Mualem (1976) relative permeability with a constant S_{nr} value of 0 (solid line) and a constantly updated value of S_{nr} based on the linear trapping model (eq 3.6) with an f_r value of 0.3125 (dashed line). 30

3.5 Example of an adjusted relative permeability curve with a continuously updated S_{nr} value to a curve with a constant S_{nr} value of 0. 31

3.6 Example of the new hysteretic non-wetting phase relative permeability curve using the linear trapping model. Multiple potential wetting phase imbibition branches are shown for different turning-point saturations. 33

3.7 Example of the new hysteretic non-wetting phase relative permeability curve using the trapping model by Land (1968). Multiple potential wetting phase imbibition branches are shown for arbitrary turning-point saturations. 34

3.8 Example of the new hysteretic capillary pressure curve using a linear trapping model. Multiple potential wetting phase imbibition branches are shown for different turning-point saturations. 36

3.9 Example of the new hysteretic capillary pressure curve using the Land (1968) trapping model. Multiple potential wetting phase imbibition branches are shown.. 37

List of Figures (Continued)

Figure Page

5.1 Experimental set up for Johnston and Adamski (2005) (adapted from Steffy et al. 1997). 42

5.2 Results from a non-hysteretic simulation of the experiment by Johnston and Adamski (2005) using a single S_{nr} value of 0. 46

5.3 Results from a non-hysteretic simulation of the experiment by Johnston and Adamski (2005) using a single S_{nr} value of 0.15. 47

5.4 Simulation results plotted with experimental results from Johnston and Adamski (2005). Data from the experiment are shown by the measurements of water flowing out of the retention cell. 48

5.5 Main wetting phase drainage capillary pressure curve based on van Genuchten (1980) (dashed line) that best fit the main wetting phase drainage capillary pressure curve (solid line) from Doughty (2007). 52

5.6 Main wetting phase drainage non-wetting phase relative permeability curve based on Charbeneau (2007) (dashed) that best fit the main wetting phase drainage non-wetting phase relative permeability curve (solid line) from Doughty (2007). 53

5.7 Non-hysteretic simulations with S_{gr} = 0 (on left) and S_{gr} = 0.25 (on right). (a-l) 56-61

5.8 Simulation results from Doughty (2007) on left, and the new hysteretic simulation on right (a-l). 63-68

5.9 Plot of CO_2 saturation over time at a depth of 700 m on the radial axis of the simulation grid. 69

5.10 Plot of CO_2 saturation over time at a depth of 900 m on the radial axis of the simulation grid. 69

List of Figures (Continued)

Figure Page

5.11 Plot of CO_2 saturation over time at 1,000 m depth 100 m from the radial axis of the simulation grid. 70

5.12 Permeability modifiers mapped onto TOUGH2 grid using iTOUGH2 GSLIB. 73

5.13 Non-wetting phase relative permeability curves for Case 1(a), Case 2(b), and Case 3(c). 75-77

5.14 Results from the 3-D simulations using a hysteretic model using the linear trapping model (top left), hysteretic model using the Land trapping model (top right), and a non-hysteretic model (bottom). 87

1.0 INTRODUCTION

Current annual anthropogenic emissions of CO_2 exceed 27 billion metric tons worldwide and the combustion of fossil fuels is responsible for more than 80% of the increase in atmospheric CO_2 since the start of the industrial revolution (IPCC 2007). Stationary sources of CO_2 are responsible for approximately 3.8 billion metric tons of the estimated 5.6 billion metric tons emitted annually by the United States (U.S. DoE 2008). Electricity generation accounts for 83% of the CO_2 emitted from stationary sources in the United States (U.S. DoE 2008).

Although the transition from fossil fuels to alternative fuel sources will eventually lead to the reduction of greenhouse gas emissions, it is expected to occur slowly. Fossil fuels are abundant, relatively cheap, easy to store, and due to the well-established infrastructure, will continue to be a significant source of energy through the rest of the century. Geologic carbon sequestration is an attractive choice for reducing CO_2 emissions.

Geologic carbon sequestration involves injecting dissolved or supercritical phase CO_2 into a deep geologic unit where it is intended to stay indefinitely. The ideal targets for geologic carbon sequestration are large, stationary sources such as fossil-fuel or biomass energy facilities, natural gas production, or any major CO_2-emitting industries. The process of geologic carbon sequestration involves the separation and compression of CO_2 from the flue gas that results from the industrial process, then transportation and injection of the captured CO_2 into a deep geologic unit for permanent storage. Deep brine formations hold the greatest storage potential for CO_2 disposal in the U.S., an estimated

range of 3,300 to 12,000 billion metric tons (U.S. DoE 2008). This potential storage volume is an attractive target for the annual 3.8 billion metric tons of CO_2 emitted from stationary sources in the U.S. (U.S. DoE 2008).

1.1 Mechanisms for trapping CO_2

In order for successful storage to occur, the CO_2 must be effectively trapped within the geologic unit. In order of increasing security and increasing storage time requirements, trapping of the CO_2 occurs by structural, capillary, solubility, and mineralization processes.

1.1.1 Structural trapping

For ease of transportation and injection in most cases, CO_2 will be compressed and injected to depths greater than 800 meters. At these depths hydrostatic pressure and geothermal temperature typically exceed the critical point for CO_2 (7.38 MPa, 31°C). Because the surrounding brine is denser than supercritical CO_2, buoyancy forces will tend to drive the injected fluid toward the surface. The first mechanism under which supercritical CO_2 is trapped in the subsurface is structural trapping, which is the impediment of the upward flow of CO_2 by a low-permeability caprock.

1.1.2 Capillary trapping

The injection and migration of supercritical CO_2 in a deep saline aquifer involves simultaneous flow of two immiscible fluids: CO_2 and brine. Conventional multiphase flow assumptions consider one phase (typically water) to preferentially adhere to solid surfaces (known as a wetting phase) while other phases, such as gas or NAPL (non-aqueous phase liquid), are referred to as a non-wetting phase. During supercritical CO_2

injection, the pressure difference (known as capillary pressure) between the non-wetting phase (CO_2) and the wetting phase (native brine) will drive the CO_2 phase into the largest pores of the rock first, pushing the brine out of the pores. Smaller pores can be invaded by the non-wetting phase following increasing differential pressure between wetting and non-wetting phases (known as capillary pressure). Once the injection stops, the CO_2 continues to migrate due to buoyancy and regional groundwater flow. At the leading edge of the migrating CO_2 plume, the CO_2 phase continues to displace the brine while at the trailing edge of the plume the brine displaces the CO_2 as capillary pressure decreases (Juanes et al. 2006). The brine imbibition process leads to snap-off at the pore-scale and the trapping of the CO_2 phase (Juanes et al. 2010). This pore-scale trapping is known as capillary trapping and the amount of trapped CO_2 phase in the pore space is referred to as residual saturation.

1.1.3 Solubility trapping

As the immiscible CO_2 phase comes into contact with the brine, some of the CO_2 will dissolve into the aqueous phase (1.45E-3 kg/L). The CO_2-saturated brine is slightly denser than the native brine, therefore eliminating the upward buoyant flow of CO_2. This process is known as solubility trapping. A potential mechanism under which the CO_2 dissolution process is enhanced is the increased amount of contact area between the CO_2 and the brine as the CO_2 plume grows and migrates and as the CO_2-saturated brine sinks away and allows native brine to re-establish contact with the CO_2 plume.

1.1.4 Mineral trapping

Following a very long storage time, the CO_2 can eventually react with the aquifer materials to form a carbonate mineral precipitate. This natural process is considered to be the most secure form of CO_2 trapping.

1.2 Characteristic curves

Multiphase flow numerical models, those used in the petroleum and environmental industries and those used for CO_2 sequestration, use characteristic curves to describe the interactions of the separate phases. Characteristic curves are functions that describe relative permeability-saturation and capillary pressure-saturation relationships at the grid-block scale, and ultimately control the multiphase flow. Characteristic curves are dependent upon the properties of the material each grid-block represents.

1.2.1 Relative permeability curves

A relative permeability curve is a function that controls the ease at which fluids may flow in a multiphase model. Relative permeability (k_r) is a scaling factor (0-1), and it is the ratio of the effective β phase permeability, $k_{e\beta}$, to the intrinsic permeability, k.

$$k_{r\beta} = \frac{k_{e\beta}}{k}, \qquad \textbf{(1.1)}$$

It is used to adapt the single phase flow Darcy equation to multiphase flow;

$$q_\beta = \frac{-k_{r\beta}k}{\mu_\beta}\left(\nabla P_\beta + \rho_\beta g \nabla z\right), \qquad \textbf{(1.2)}$$

where q_β is the darcy flux in phase β, μ_β is the viscosity of phase β, ∇P_β is the pressure gradient in phase β, ρ_β is the density of phase β, g is gravitational acceleration, and ∇z is the elevation gradient.

To clarify the idea of relative permeability, a porous medium will have a specific fluid conductivity value for a given fluid, e.g. water, under single-phase conditions. But the presence of a second fluid phase, e.g. NAPL (non-aqueous phase liquid), in the pores of the medium will decrease the ease at which the water flows through the medium. Therefore it is necessary to scale the fluid conductivity of the medium for each fluid phase to represent the competition of multiple phases for pore space fluid pathways.

Non-hysteretic characteristic curves can only use one value of residual non-wetting phase saturation (S_{nr}), which represents the amount of non-wetting fluid trapped in the pores of a medium due to capillary forces. Figure 1.1 shows non-hysteretic non-wetting phase relative permeability curves modeled with non-wetting phase residual saturation (S_{nr}) values of 0 and 0.25. As the non-wetting phase invades the pore space, wetting phase drainage occurs and the relative permeability of the non-wetting phase (k_{rn}) increases. The wetting phase drainage process can continue until the value of aqueous saturation reaches S_{lr}, which represents the irreducible wetting phase saturation (S_{lr} = 0.2 for both curves). At this point in the curve the non-wetting phase has its highest mobility. Replacement of the non-wetting phase by the wetting phase leads to the model following the curve back downwards as the non-wetting phase relative permeability decreases. The value of S_{nr} represents the non-wetting phase saturation at a k_{rn} value of zero — meaning it is immobile, or trapped in the pores of the medium. A non-hysteretic krn model can

only use one of these curves, so it tends to either under-predict or over-predict the non-wetting phase trapping.

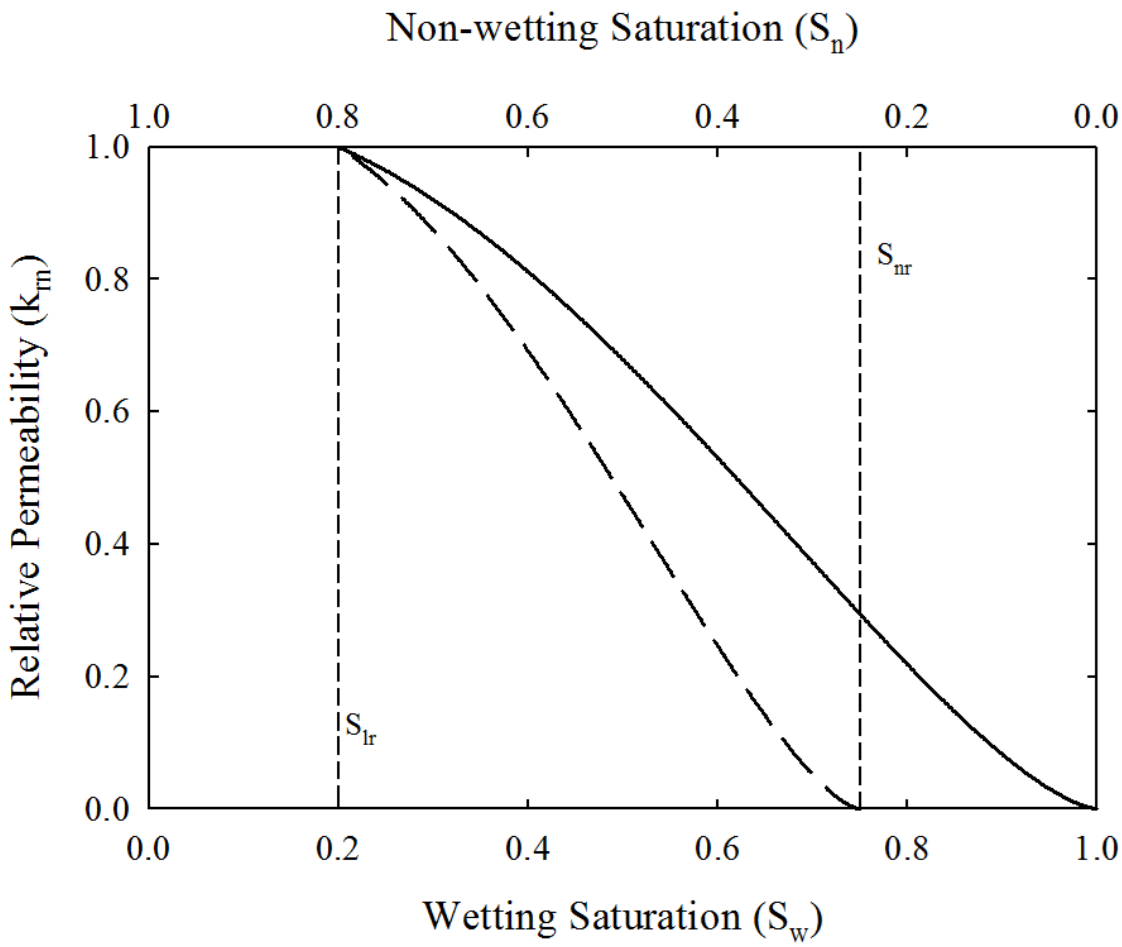

Figure 1.1 Examples of non-hysteretic relative permeability curves by Mualem (1976). The two curves are modeled using an S_{nr} value of 0 (solid line) and another with an S_{nr} value of 0.25 (dashed line).

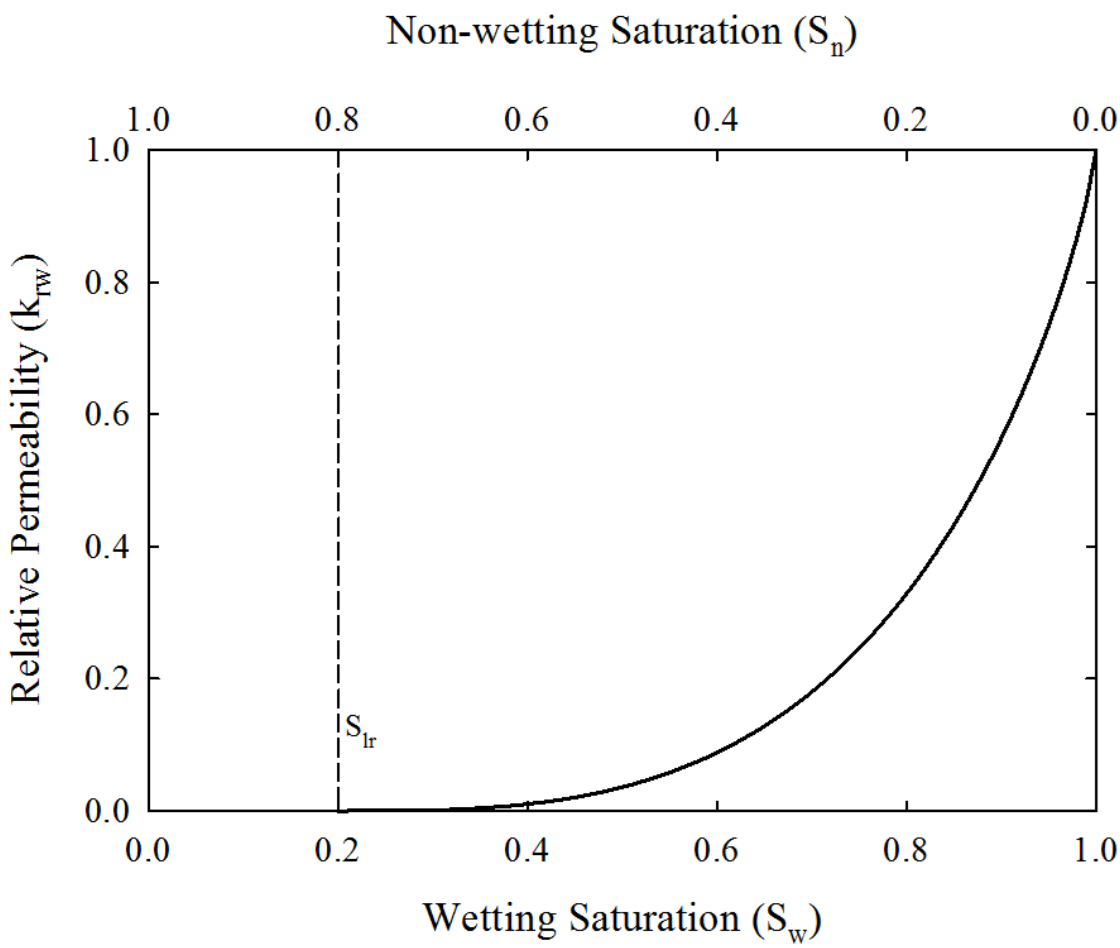

Figure 1.2 Example of a nonhysteretic wetting phase relative permeability curve. The wetting phase is immobile ($k_{rw} = 0$) at $S_w = S_{lr}$.

Figure 1.2 shows an example of a non-hysteretic wetting phase relative permeability curve with an irreducible wetting phase saturation of 0.2. Although relative permeability curves exist for both wetting and non-wetting phases, the non-wetting phase relative permeability curves are more critical to predicting the mobility of NAPL or CO_2 during multiphase flow.

1.2.2 Capillary pressure curves

In a system consisting of two immiscible fluids in a porous medium, there exists an interface that distinguishes the two fluids as separate phases. This interface can shift through the pores as a response to pressure differences between the two phases, or capillary pressure (P_c). Increases in capillary pressure can drive the non-wetting phase (the phase that does not preferentially adhere to solid surfaces) to advance into the pores, expelling the wetting-phase (the phase that preferentially adheres to solid surfaces) while decreases in capillary pressure reverse the process.

Figure 1.3 shows a set of typical non-hysteretic capillary pressure curves. The curves shown in this figure were modeled with a single value of residual non-wetting phase saturation set to 0 and 0.25. As an increase in capillary pressure occurs, the model follows the branch upwards (a wetting-phase drainage process) and non-wetting phase saturation (S_n) can increase until the irreducible wetting-phase saturation (S_{lr}) is reached (signifying a complete wetting-phase drainage). A subsequent decrease in capillary pressure will cause the model to follow the branch back downwards (a wetting-phase imbibition process) as S_n decreases. During wetting phase imbibition, the model can only follow the capillary pressure curve as far as the residual non-wetting phase saturation set in the relative permeability function. At this point the non-wetting fluid is immobile (k_{rn} = zero) and the capillary pressure at S_{nr} does not necessarily equal zero. If the zero S_{nr} capillary pressure curve in figure 1.3 was used in conjunction with the 0.25 S_{nr} relative permeability curve in figure 1.1, wetting phase imbibition could only continue to a non-

wetting phase saturation of 0.25, which is the value of residual non-wetting phase saturation set in the relative permeability curve.

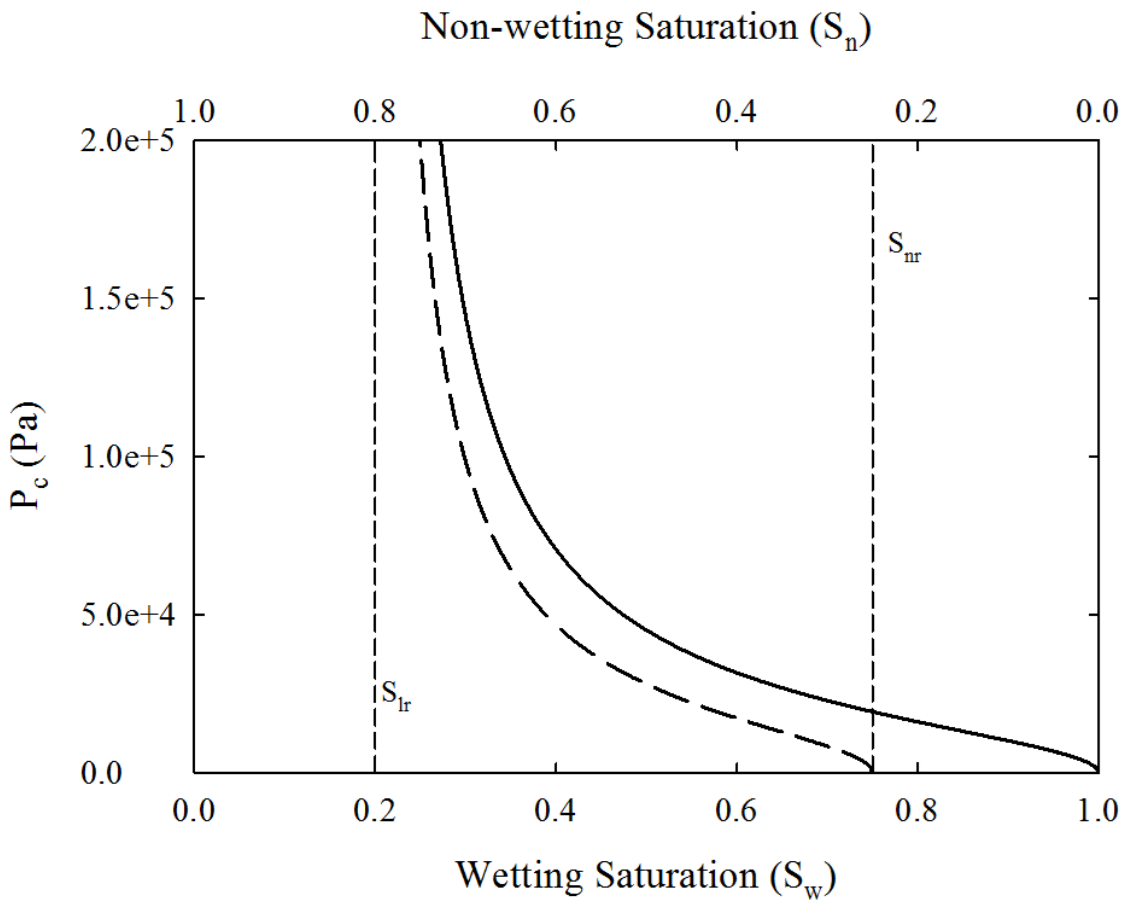

Figure 1.3 Two non-hysteretic capillary pressure curves from van Genuchten (1980) showing aqueous phase saturation as a function of capillary pressure (P_c).

Non-hysteretic characteristic curves use only a single value of S_{nr} and do not have the ability to capture the accurate saturation sequence for a dynamic flow process. A system of pores is complex and the saturation path upon wetting phase drainage is not the same as that upon wetting phase imbibition (Charbeneau 2007). For useful estimates of residual non-wetting phase saturation, the maximum value of non-wetting phase

saturation needs to be considered (Charbeneau 2007). The reasoning for this is that regions with greater non-wetting phase saturations during wetting phase drainage will retain greater non-wetting phase saturations during subsequent wetting phase imbibition processes (Lenhard and Parker 1987, Lenhard 1992, Kueper et al. 1993, Steffy et al. 1997, Johnston and Adamski 2005, Charbeneau 2007). Hysteresis refers to irreversible saturation paths for multiphase flow interactions.

Relative permeability curves that do not consider hysteresis tend to underpredict the non-wetting phase relative permeability when the phase first invades a water filled system, and they can over predict the mobility if the non-wetting phase is being displaced by water (Parker and Lenhard 1987, Lenhard and Parker 1987, Niemi and Bodvarsson 1988, Kaluarachchi and Parker 1992, Fagerlund et al. 2008). If a non-hysteretic relative permeability curve with a residual non-wetting phase saturation of 0.25 (like that shown in figure 1.1) is used, non-wetting phase saturation must build to 0.25 before becoming mobile. However, if the non-hysteretic relative permeability curve with a residual non-wetting phase saturation of 0 (like that shown in figure 1.1) is used, then there is no trapping of the non-wetting phase upon wetting phase imbibition.

1.3 Hysteretic characteristic curves

The characteristic curves in Figures 1.4 and 1.5 are hysteretic, meaning they describe relative permeability and capillary pressure based not only on the current saturation but also on the history of saturation at the respective grid-block. These curves attempt to recreate the physical phenomenon known as hysteresis, where the amount of trapped fluid in the pores of a medium is dependent on the maximum amount of that fluid

that initially entered the pores of the medium (Parker and Lenhard 1987, Lenhard and Parker 1987, Niemi and Bodvarsson 1988, Kaluarachchi 1992, Van Geel 2002, Fagerlund et al. 2008). Note that there are multiple wetting phase imbibition scanning curves for different turning-point saturations (the saturation value at the point where the process changes from wetting phase drainage to wetting phase imbibition). The arrows on the curve represent the direction in which the model follows the curve during wetting phase drainage and imbibition. Probably the most important aspect of hysteretic characteristic curves is the calculation of S_{nr}- represented as the value of S_n at which a wetting phase imbibition branch has led to a capillary pressure or relative permeability value of zero—which varies depending on the maximum value of S_n reached during the wetting phase drainage process. Greater values of S_n reached during wetting phase drainage correspond to greater values of S_{nr}.

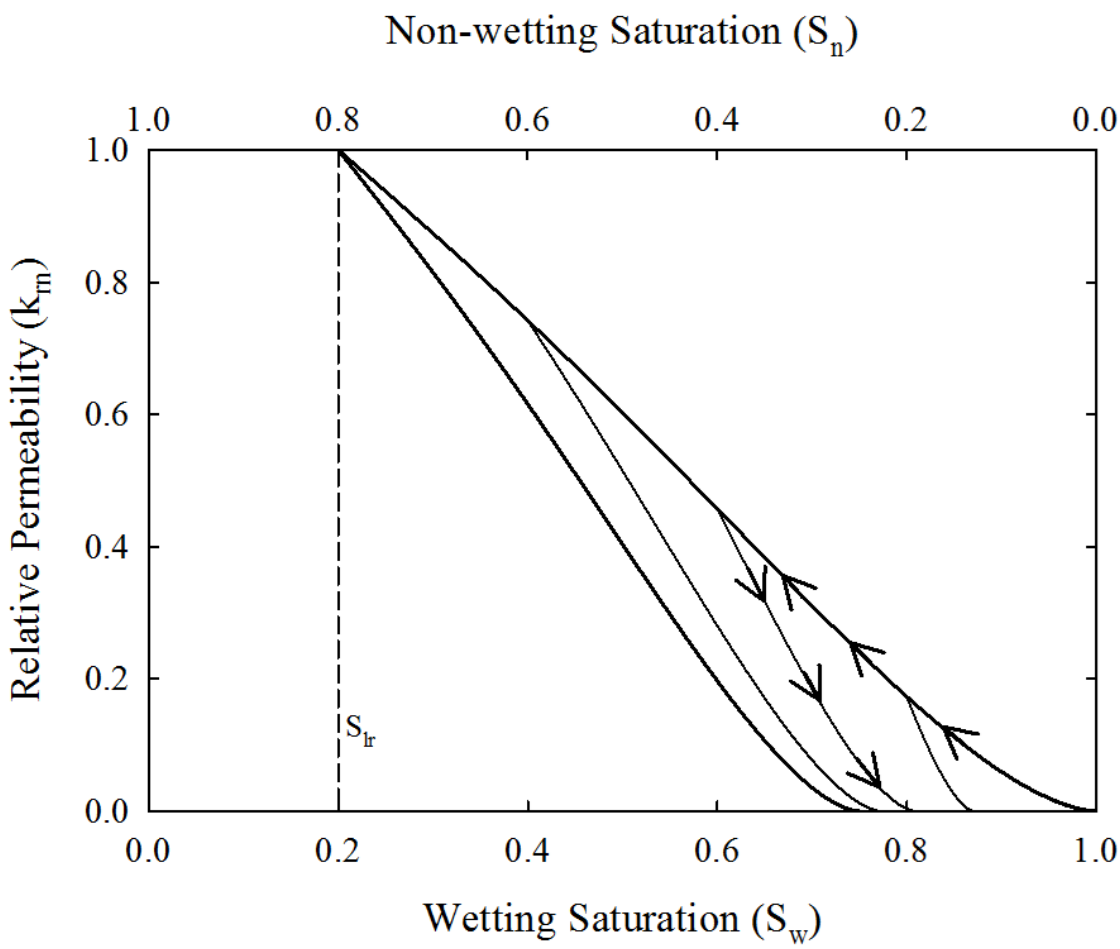

Figure 1.4 A hysteretic non-wetting phase relative permeability curve from Doughty (2007). The numerical model will follow the main drainage branch upwards during wetting phase drainage, and will follow a secondary imbibition path downwards during wetting phase imbibition. The path of the imbibition branch depends on the turning-point saturation. This example shows multiple potential turning-points each with a separate imbibition branch. The value of S_{nr} is represented by $(1-S_w)$ at $k_{rn} = 0$.

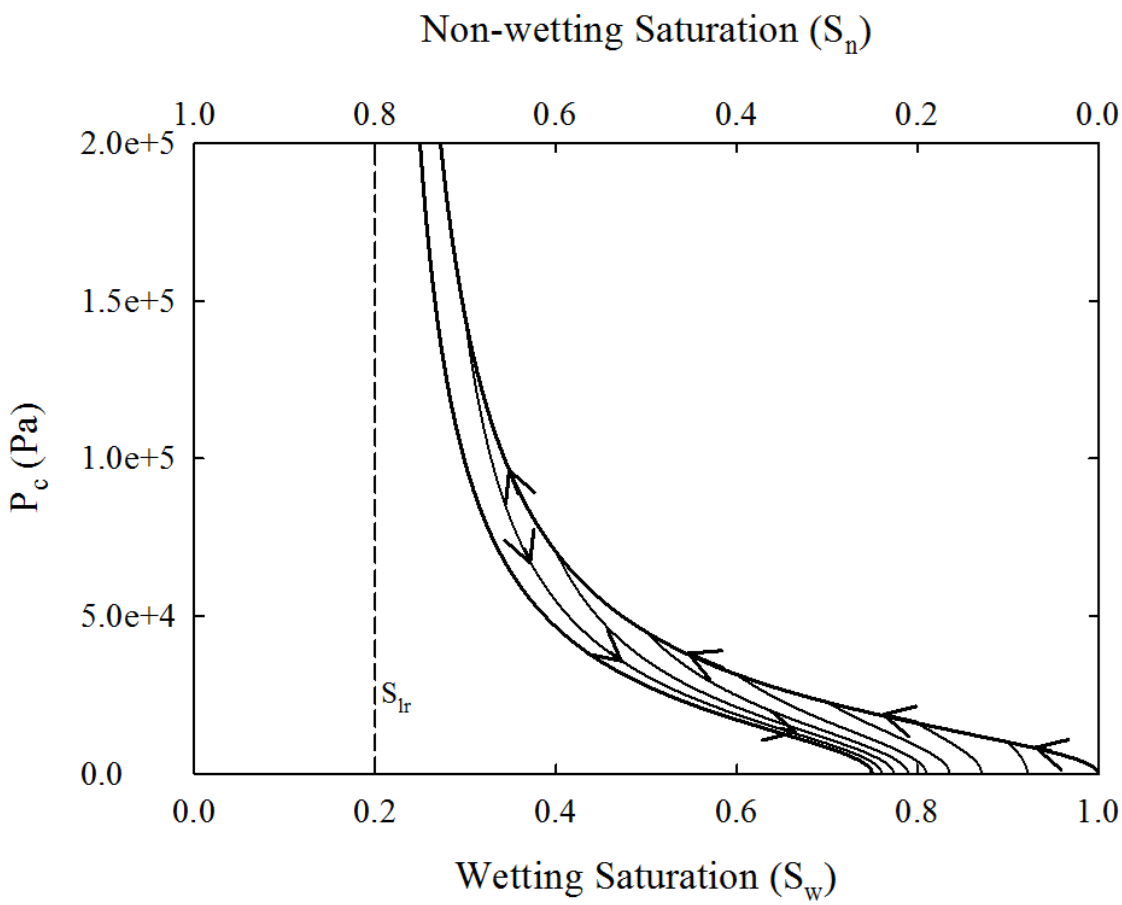

Figure 1.5 A hysteretic version of van Genuchten (1980) from Doughty (2007) capillary pressure curve. The numerical model will follow the main drainage branch upwards during wetting phase drainage, but will follow a secondary imbibition path downwards during wetting phase imbibition. The path of the imbibition branch depends on the turning-point saturation. This example shows multiple potential turning-points each with a separate imbibition branch. The value of S_{nr} is represented by $(1-S_w)$ at $P_c = 0$.

1.4 Motivation and Purpose of Study

The amount of fluid trapped at the pore scale affects the overall mobility of the fluid in the subsurface. Where there exists both drainage- and imbibition processes, e.g. during buoyancy-driven flow of supercritical CO_2, or during NAPL transport through geologic media, the use of hysteretic values for residual saturation is critical to the prediction of fluid movement. Hysteresis has been observed experimentally in problems involving NAPLs (Lenhard and Parker 1987, Lenhard 1992, Kueper et al. 1993, Steffy et al. 1997, Johnston and Adamski 2005) and a number of hysteretic extensions to characteristic curves have been devised for predicting phase saturations in multiphase flow simulations for environmental and petroleum applications (Parker and Lenhard 1987, Lenhard and Parker 1987, Niemi and Bodvarsson 1988, Kaluarachchi and Parker 1992, Van Geel 2002, Fagerlund et al. 2008). However the incorporation of these hysteretic models into codes such as TOUGH2 (Pruess 1999) can become quite complex, requiring more parameters for the hysteretic model than for the non-hysteretic model.

The purpose of this study is to provide a simple and numerically stable hysteretic model that can be applied to predicting phase saturations in multiphase flow simulations of carbon sequestration or NAPL transport.

2.0 OBJECTIVES AND APPROACH

The objective of this study is to test the capability of a numerically stable hysteretic model that can be used to simulate the multiphase flow non-wetting trapping processes as a CO_2 or NAPL plume migrates through the subsurface. First a mathematical review of characteristic functions used to predict phase saturations for multiphase flow is presented. Included in the review are some previous extensions to consider hysteresis within the characteristic functions, as well as a comparison to and a discussion of the new hysteretic model. Modified versions of TOUGH2- ECO2N (Pruess 2005) and TOUGH2-TMVOC (Pruess 2002) are used to assess the capability of the new numerical hysteretic model. A brief explanation of the implementation of the new hysteretic model into the numerical code is provided. The following sections detail the assessment of the new hysteretic formulation by simulations of multiphase flow for 1-, 2-, and 3- dimensional models. The new hysteretic model is compared against both experimental and published simulation results. The importance of using hysteretic curves for multiphase numerical models is emphasized in a comparison of simulations using both hysteretic and non-hysteretic curves.

3.0 MATHEMATICAL METHODS

3.1. Relative permeability models

NAPL relative permeability curves can be measured in the laboratory, but this is often not done because of experimental difficulties and cost (Charbeneau 2007). Instead, model equations are used to associate relative permeability with capillary pressure curve parameters (Charbeneau 2007). The two most commonly used models are those by Burdine (1953) and Mualem (1976). Van Genuchten and Nielsen (1985) found that the permeability model by Mualem is applicable to a wider variety of soils than Burdine's model. For a 2-phase system, Mualem's permeability model is

$$k_{rn}\left(S_n\right)=\sqrt{1-\overline{S}_w}\left(1-\overline{S}_w^{\,1/m}\right)^{2m} \tag{3.1}$$

where $m=1-1/n$, n is curve-fitting parameter, S_n is the saturation of the non-wetting phase and $\overline{S}_w$ represents an effective wetting phase saturation which is the actual wetting phase saturation (S_w) scaled with respect to irreducible wetting phase saturation (S_{lr}) and residual non-wetting phase saturation (S_{nr}) (Charbeneau 2007);

$$\overline{S}_w=\frac{S_w-S_{lr}}{1-S_{nr}-S_{lr}} \tag{3.2}$$

Examples of the Mualem relative permeability curve are shown in figure 1.1 while the curve parameters are shown in table 3.1, with S_{nr} = 0 and S_{nr} = 0.25.

3.2 Capillary pressure models

Capillary pressure-saturation relationships are frequently determined experimentally by measuring changes in wetting and non-wetting fluid saturation within a porous medium vs. changes in capillary pressure (van Geel 2002). These relationships for 2-phase fluid systems can often be fit by the van Genuchten (1980) equation.

$$\overline{S}_w = \left[1 + \left(\alpha h_c\right)^n\right]^{-m} \tag{3.3}$$

for Pc $>$ 0, and

$$\overline{S}_w = 1$$

for Pc $\leq$ 0, where h_c is capillary head, and α and n are fitting parameters with $m = 1 - 1/n$.

Rearranging the van Genuchten equation in terms of capillary pressure gives

$$P_c(S_w) = \frac{\rho_w g}{\alpha}\left[\overline{S}_w^{\,-1/m} - 1\right]^{1-m} \tag{3.4}$$

where P_c is capillary pressure, α and m are the fitting parameters, ρ_w is the density of water, and g is gravitational acceleration. An example of van Genuchten's capillary pressure curve is presented in figure 1.3 and the parameters for the function are in table 3.2.

Relative permeability curve parameters	Parameter value
n	2
S_{lr}	0.2
S_{nr}	0, 0.25

Table 3.1: Model parameters for the non-hysteretic relative permeability curves used in figure 1.1.

3.3 Calculation of residual saturation

The residual non-wetting phase saturation (S_{nr}) is a measure of the capacity of a porous medium to retain non-wetting fluid during wetting phase imbibition for a 2-phase system (Charbeneau 2007). This is important to consider for environmental, petroleum, and carbon sequestration modeling as the amount of trapped non-wetting fluid is of particular interest. Laboratory experiments show that the amounts of trapped non-wetting phase increase with maximum non-wetting phase saturation (Kueper et al. 1993, Steffy et al. 1997, Johnston and Adamski 2005). The maximum non-wetting phase saturation can be thought of as the non-wetting phase saturation at the point in which the process changes from wetting phase drainage to wetting phase imbibition (a turning-point). A popular method of estimating residual non-wetting phase saturation is an equation from Land (1968):

$$S_{nr} = \frac{S_n^{\max}}{1 + R(S_n^{\max})} \qquad \textbf{(3.5)}$$

where

$$R = \frac{1}{S_{nr}^{\max}} - 1 \quad ,$$

where $S_n^{\max}$ is the maximum non-wetting phase saturation achieved at a particular location throughout the history of wetting phase drainage and imbibition, and $S_{nr}^{\max}$ is the maximum S_{nr} reached following complete wetting phase drainage.

Capillary pressure curve parameter	**Parameter value**
n	**2**
S_{lr}	**0.2**
α	**0.539**
S_{ls}	**1**

Table 3.2: Parameters for van Genuchten capillary pressure curve used in figure 1.3.

Experimental results from Kueper et al. (1993) and Johnston and Adamski (2005) suggest that residual non-wetting phase saturation values increase linearly with turning-point saturations. A simple alternative to eq. 3.5 relating the residual non-wetting phase saturation and turning-point saturation for a 2-phase fluid system is

$$S_{nr} = f_r (1 - S_w^{\min}) = f_r S_n^{\max} \qquad \textbf{(3.6)}$$

where f_r is the slope of the linear relationship between maximum- and residual non-wetting phase saturation.

Figure 3.1 shows S_{nr} plotted as a function of $S_n^{\max}$ with a value of 0.2 for S_{lr} and 0.25 for the maximum value of S_{nr} for both the Land (1968) trapping model and the linear trapping model. Although the maximum value of S_{nr} is the same between the two

trapping models, the Land (1968) trapping model calculates higher values of S_{nr} below the maximum value of S_{nr}.

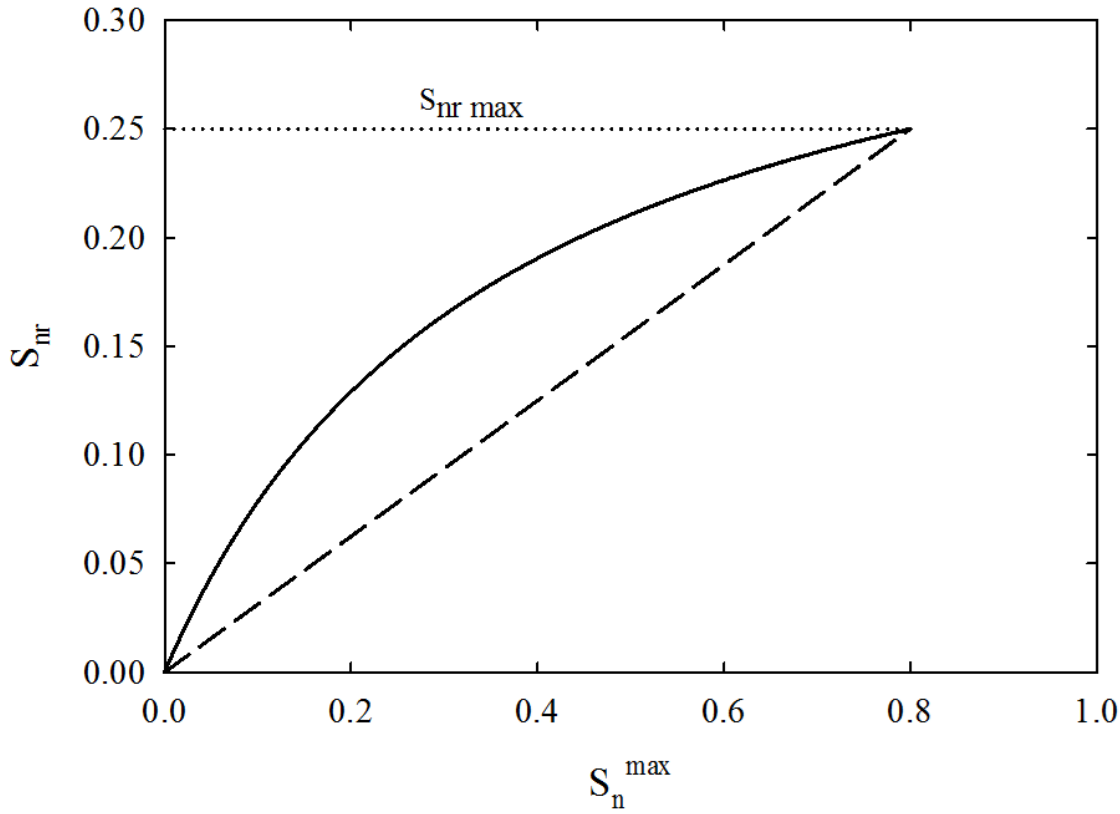

Figure 3.1 Plot of S_{nr} vs S_{nmax} for both the Land (1968) trapping model (solid line) and the linear trapping model (dashed line). The maximum S_{nr} value is 0.25.

3.4 Hysteretic extensions to characteristic curves

Doughty (2007) considers hysteresis in the non-wetting phase relative permeability curve adapted from the non-hysteretic van Genuchten expression by Lenhard and Parker (1987):

$$k_{rn} = \sqrt{1-(\overline{S}_w + \overline{S}_{nt})}\left[1-(\overline{S}_w + \overline{S}_{nt})^{1/m}\right]^{2m} \qquad \textbf{(3.7)}$$

where

$$\overline{S}_{nt} = \frac{S_{nr}(S_w - S_w^{\min})}{(1-S_{lr})(1-S_w^{\min} - S_{nr})} \qquad \textbf{(3.8)}$$

S_{nr} is equal to 0 for the main wetting phase drainage branch, then calculated according to Land (1968) (eq. 3.5) for imbibition. Figure 3.2 shows an example of the non-wetting phase relative permeability curve used by Doughty (2007) and the model parameters are shown in table 3.3.

Two-phase systems considered by Kaluarachchi and Parker (1992) and Doughty (2007) treat capillary pressure as a function described by van Genuchten (eq. 3.4). The effective wetting phase saturation term (eq. 3.2) includes a value for S_{nr}, although for primary wetting phase drainage S_{nr} is equal to 0. Once the process changes from wetting phase drainage to wetting phase imbibition, S_{nr} is calculated by the Land equation (eq. 3.5) by Kaluarachchi and Parker (1992) and by a slightly modified version of the Land equation by Doughty (2007):

$$S_{nr} = \frac{S_n^{\max}}{1+\left[1/S_{nr}^{\max} - 1/(1-S_{lr})\right]S_n^{\max}} \qquad \textbf{(3.9)}$$

Refer to figure 3.3 for an example of a capillary pressure curve used by Kaluarachchi and Parker (1992) and to table 3.4 for the model parameters.

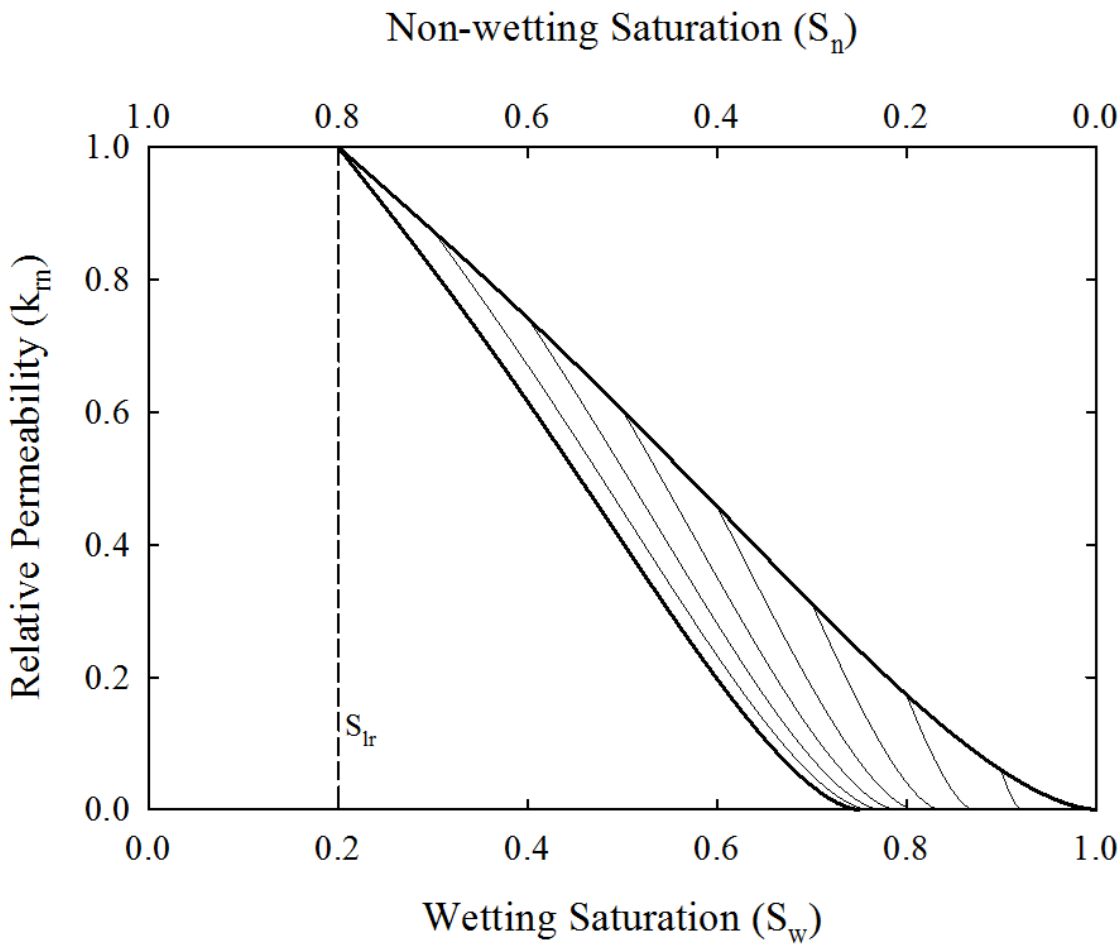

Figure 3.2 Example of a hysteretic non-wetting phase relative permeability function used by Doughty (2007). Multiple potential wetting phase imbibition branches are shown for arbitrary turning-point saturations.

Relative permeability curve parameters	Parameter value
n	2
S_{lr}	0.2
S_{nr} max	0.266667

Table 3.3: Hysteretic non-wetting phase relative permeability curve parameters used in figure 3.2.

A significant characteristic of the hysteretic models shown in Figures 3.2 and 3.3 is that the derivatives of the relative permeability and the capillary pressure with respect to saturation are discontinuous at the turning points. The discontinuity is caused by an abrupt switch from a value of zero for S_{nr} to a non-zero value for S_{nr}. In codes such as TOUGH2, which are based on a residual minimization method using Newton-Raphson iteration, discontinuous functions can cause a multiphase flow code to take short time steps and run very slowly (Fagerlund et al. 2008). To alleviate the numerical difficulties, the characteristic curves can be artificially smoothed as the turning points are approached (Doughty 2007, Fagerlund et al. 2008).

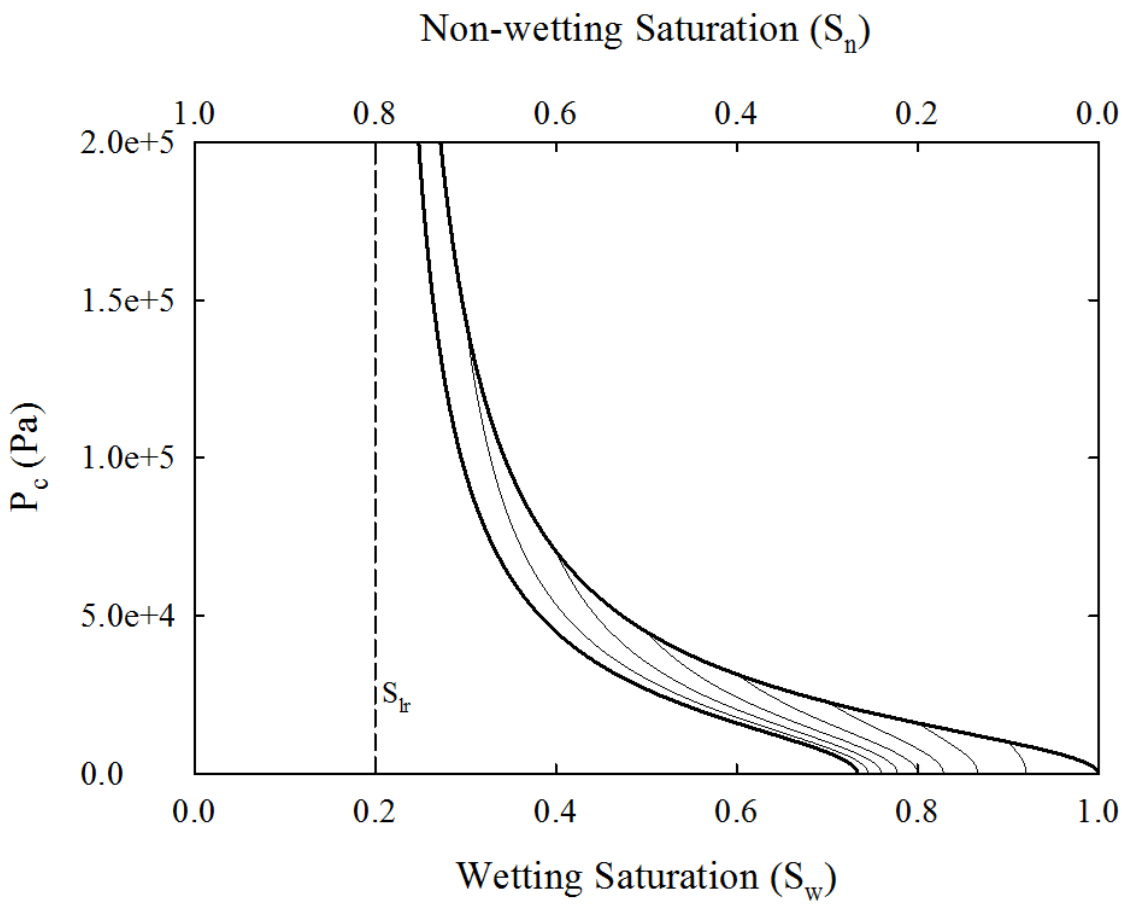

Figure 3.3 Hysteretic capillary pressure curve from Kaluarachchi and Parker (1992) showing multiple imbibition branches for arbitrary turning-point saturations.

Capillary pressure curve parameter	Parameter value
N	2
S_{lr}	0.2
α	0.539
S_{nr} max	0.26667

Table 3.4: Hysteretic capillary pressure curve parameters used in figure 3.3.

The numerical difficulties from a sharp transition from main wetting phase drainage to first-order wetting phase imbibition were addressed by Fagerlund et al. (2008) and alleviated by an addition to their model to smooth the transition. Non-wetting phase residual saturation for their main wetting phase drainage branch was zero but upon process reversal to wetting phase imbibition, S_{nr} was calculated using the Land (1968) model (eq. 3.5). The first-order wetting phase imbibition scanning curves were based on the modifications to the dependent-domain theory by Mualem (1984) made by Niemi and Bodvarsson (1988):

$$S_w = S_w^{\min} + \frac{\left(S_w^f - S_w^{\min}\right)}{\left(S_w^{f\min} - S_w^i(P_c^\Delta)\right)}\left(S_w^i(P_c) - S_w^i(P_c^\Delta)\right) \qquad \textbf{(3.10)}$$

where S_w^f is the final wetting phase saturation on the scanning curve and is equal to $1-S_{nr}$, $S_w^{f\min}$ is the minimum value of S_w^f and is equal to $1-S_{nr}^{\max}$, $S_w^i(P_c^\Delta)$ is the wetting phase saturation as predicted from the main imbibition curve at P_c^Δ, P_c^Δ represents the capillary pressure at the turning-point, and $S_w^i(P_c)$ is the wetting phase saturation as predicted from the main imbibition curve for the current capillary pressure.

First, a value for $S_w^i(P_c)$ is solved for using eq. 3.10, then $P_c\left(S_w^i\right)$ is calculated by inverting the van Genuchten capillary pressure function (eq. 3.1) using the main wetting phase imbibition parameters.

Eq. 3.10 indicates that S_w on the scanning wetting phase imbibition is predicted from a scaled portion of the main wetting phase imbibition curve which lies between

$S_w^i(P_c^\Delta)$ and $S_w^{f\,\min}$ (Fagerlund et al. 2008). This portion of the curve is scaled to start at turning-point wetting phase saturation and end at S_w^f (Fagerlund et al. 2008). In a similar way, S_w can also be predicted from the portion of the main wetting phase drainage curve between the turning-point wetting phase saturation and 0, scaled to the end at the final wetting phase saturation on the wetting phase imbibition scanning curve. That equation takes the following form:

$$S_w = S_w^{\min} + \frac{\left(S_w^f - S_w^{\min}\right)}{\left(1 - S_w^{\min}\right)}\left(S_w^d(P_c) - S_w^{\min}\right) \qquad \textbf{(3.11)}$$

where $S_w^d\left(P_c\right) =$ the wetting phase saturation on the main wetting phase drainage branch

Now a value for $S_w^d\left(P_c\right)$ is calculated from eq. 3.11 and then $P_c\left(S_w^d\right)$ is calculated from eq. 3.1. Finally, P_c is calculated as a weighted sum of the capillary pressures predicted from equations 3.10 and 3.11, i.e., $P_c\left(S_w^i\right)$ and $P_c\left(S_w^d\right)$, respectively:

$$P_c = a^k P_c\left(S_w^d\right) + \left(1 - a^k\right) P_c\left(S_w^i\right) \qquad \textbf{(3.12)}$$

where a^k determines the weighting. a depends linearly on S_w so that it is 0 at $S_w = S_w^f$ and equals 1 at $S_w = S_w^{\min}$ (Fagerlund et al. 2008):

$$a = \frac{S_w^f - S_w}{S_w^f - S_w^{\min}} \qquad \textbf{(3.13)}$$

As a result, the first-order scanning wetting phase imbibition curve resembles the main wetting phase drainage curve near the turning-point but further away, with

increasing wetting phase saturation, the curve takes the shape of the original Mualem (1984) model (eq. 3.1) (Fagerlund et al. 2008). Careful consideration must be taken when choosing the value for k as it determines the weight of the summation. A high enough value should be chosen so that the resulting scanning wetting phase imbibition curve resembles the original Mualem (1984) model but low enough to ensure a smooth transition from wetting phase drainage to wetting phase imbibition at the turning point (Fagerlund et al. 2008). This method can provide a scanning wetting phase imbibition curve with the same slope as the main wetting phase drainage curve, resulting in better stability and performance with the T2VOC (Falta et al. 1995) numerical simulator used (Fagerlund et al. 2008).

Doughty (2007) employed extensions to the hysteretic formulations to ensure numerical stability. They include a power-law extension to the van Genuchten capillary pressure function to account for dissolution of trapped CO_2 and a cubic splice in the relative permeability function to smoothly connect the drainage branch to the imbibition branch (Doughty 2007).

For the models implemented in Fagerlund et al. (2008), reversal from wetting phase drainage to wetting phase imbibition only occurs once, implying that second-order wetting phase drainage is not considered. Mualem (1984) gives expressions for first- and second-order scanning curves which are implemented and expanded to third-order scanning curves by Niemi and Bodvarsson (1988). Doughty (2007) used this interpolation between scanning curves and it is recommended the reader refer to the

literature for a detailed discussion on higher-order scanning curves (Niemi and Bodvarrson 1988).

3.5 New hysteretic model

As an alternative to producing a sharp transition at the turning-point in the characteristic curves or developing a more complex model in order to smooth the function at turning-point transitions, a simple technique for incorporating the key hysteretic effects in relative permeability and capillary pressure curves has been developed. The resulting curves are always smooth, and continuously differentiable, leading to good numerical performance in numerical codes such as TOUGH2.

The new hysteretic model is based on a continuously variable value for S_{nr} calculated from the linear trapping model (eq. 3.6) where S_n^i will be accounted for by the maximum obtained value of S_n in each grid-block ($S_n^{\max}$) which is continuously updated during a simulation. Alternatively, the trapping model from Land (1968) is used, where $\left(1-S_w^{\min}\right) = S_n^{\max}$. With either trapping model, continuously updating the value of S_{nr} in the relative permeability and capillary pressure curves ensures a continuous function at drainage-imbibition turning-points. The continuous function is a requirement for smooth numerical differentiation during the Newton-Raphson iteration technique utilized by multiphase codes such as TOUGH2.

Continuously updating the value of residual non-wetting phase saturation during wetting phase drainage results in an alteration of the shape of the curve. Therefore adjusting the model parameters is necessary to fit the main drainage curve to other models. An example of the Mualem (1976) relative permeability function with a constant

S_{nr} value of zero is plotted with the same function modeled with a continuously updated value of S_{nr} in figure 3.4. Both curves use the same parameters; they only differ in the calculation of S_{nr}. The dashed curve is modeled with a continuously updated value of S_{nr} based on the linear trapping model (eq. 3.6). By continuously updating the value of S_{nr}, the shape of the curve is brought down. This illustrates the need to adjust the model parameters of the new hysteretic model to fit other models accordingly. Figure 3.5 shows an example of a relative permeability curve with a continuously updated value of S_{nr} fitted to a traditional relative permeability curve with a constant value of 0 for S_{nr}. Parameter values for both the non-hysteretic curve and the fitted hysteretic curve are given in table 3.5.

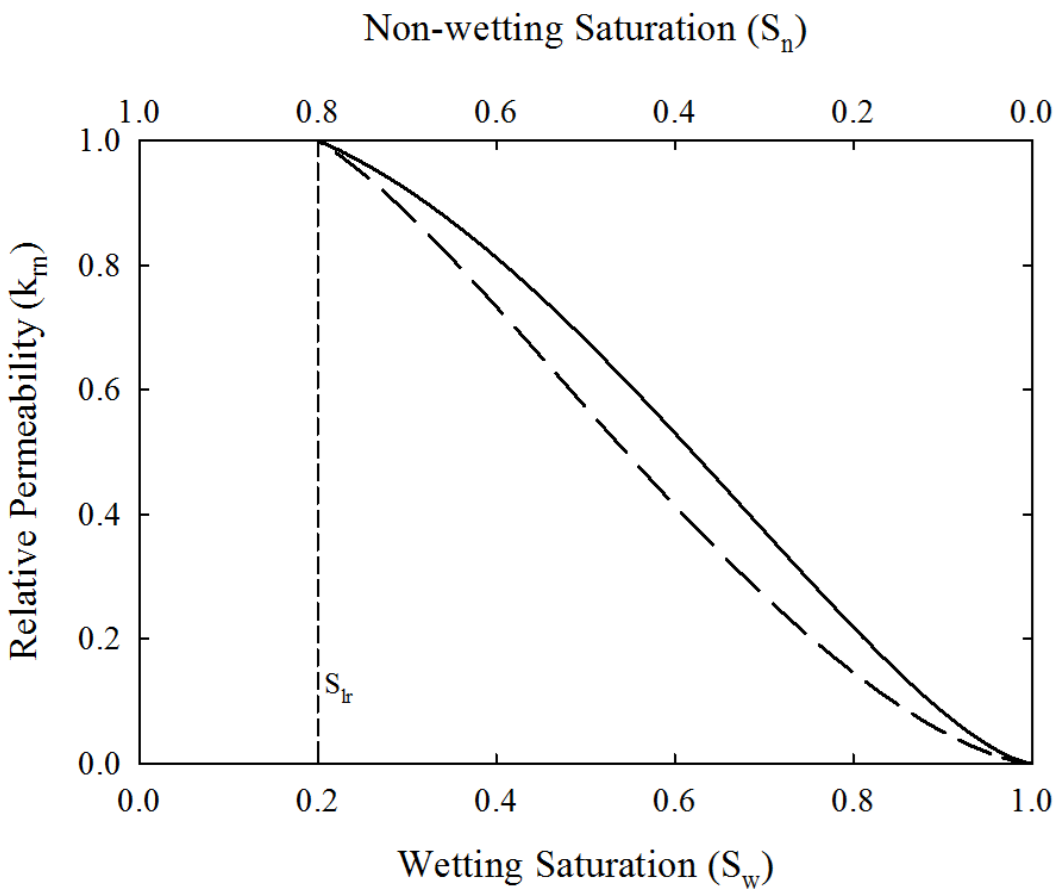

Figure 3.4 Example of Mualem (1976) relative permeability with a constant S_{nr} value of 0 (solid line) and a constantly updated value of S_{nr} based on the linear trapping model (eq 3.6) with an f_r value of 0.3125 (dashed line).

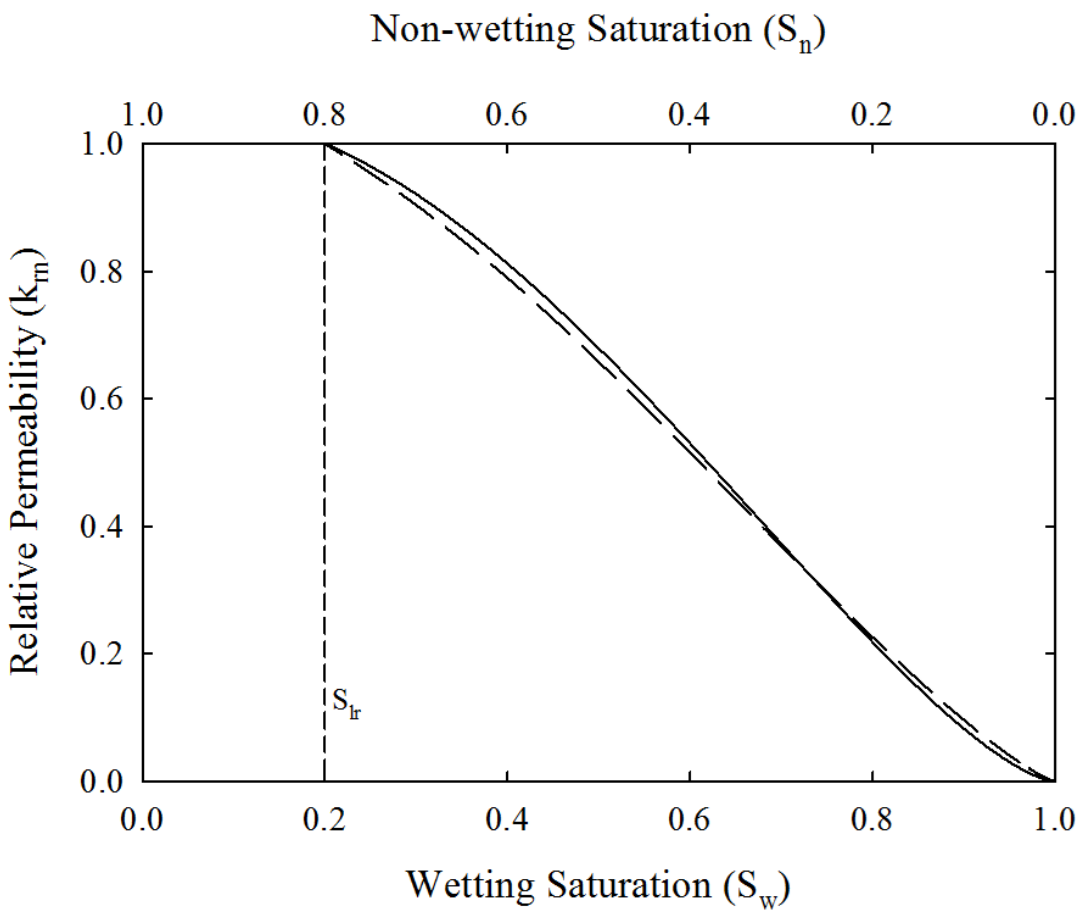

Figure 3.5 Example of an adjusted relative permeability curve with a continuously updated S_{nr} value to a curve with a constant S_{nr} value of 0.

Relative permeability curve parameter	Parameter value for fitted curve	Parameter value for non-hysteretic curve
n	1.6	2
S_{lr}	0.2	0.2
J_r	0. 25	-
S_{nr}	-	0

Table 3.5: Relative permeability curve parameters used in figure 3.5.

The non-wetting phase relative permeability curve is based on the 2-phase expression from Mualem (1984) with modifications made by Charbeneau (2007):

$$k_{rn}\left(S_n\right)=\sqrt{S_n}\left(1-\overline{S}_w^{\,1/m}\right)^{2m} \tag{3.14}$$

where $\overline{S}_w$ represents the wetting phase saturation (S_w) scaled with respect to irreducible wetting phase saturation (S_{lr}) and residual non-wetting phase saturation (S_{nr});

$$\overline{S}_w=\frac{S_w-S_{lr}}{1-S_{nr}-S_{lr}}$$

Upon comparison of Mualem's original function (eq. 3.1) to Charbeneau's modified function (eq. 3.14), the modification is in the tortuosity term (the first term on the right side of the equation) and the scaled saturation includes S_{nr}. The inspiration for this modification is that using the effective wetting phase saturation in Mualem's model (eq. 3.1) yields a k_{rn} value of 1 at the maximum S_n value, or at $S_w = S_{lr}$. The reasoning for the modification is to limit the maximum value of k_{rn} when S_{lr} is greater than zero since some of the pores are still occupied by the wetting phase and the non-wetting phase may not be flowing at single-phase permeability. Thus, S_n is used in place of the effective wetting phase saturation, so its value ranges from S_{nr} to 1-S_{lr} (Charbeneau 2007).

The Land (1968) trapping model includes a parameter for the maximum S_{nr}, but in order to ensure consistency in the maximum value of S_{nr} calculated between the linear trapping model and the Land (1968) trapping model, the value of f_r must be altered according to the value of S_{lr}. The value of f_r should be adjusted so that it is equal to the maximum desired S_{nr} divided by $\left(1-S_{lr}\right)$.

Examples of the new hysteretic relative permeability models are shown using a linear trapping model (fig. 3.6) and using the trapping model by Land (1968) (fig. 3.7) with different turning point saturation values. The parameters for the curves in figures 3.6 and 3.7 are given in tables 3.6 and 3.7, respectively.

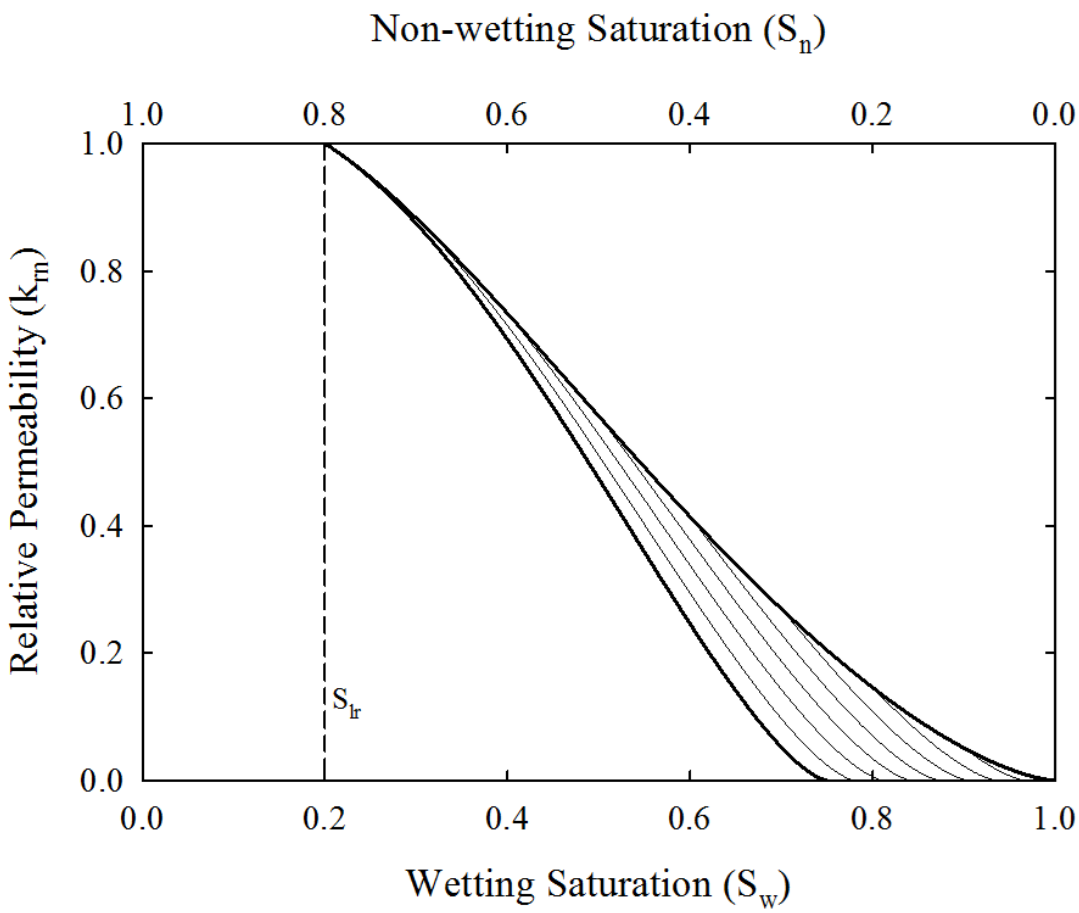

Figure 3.6 Example of the new hysteretic non-wetting phase relative permeability curve using the linear trapping model. Multiple potential wetting phase imbibition branches are shown for different turning-point saturations.

Relative permeability curve parameter	Parameter value
n	2
S_{lr}	0.2
J_r	0.3125

Table 3.6: Hysteretic relative permeability curve parameters used in figure 3.6.

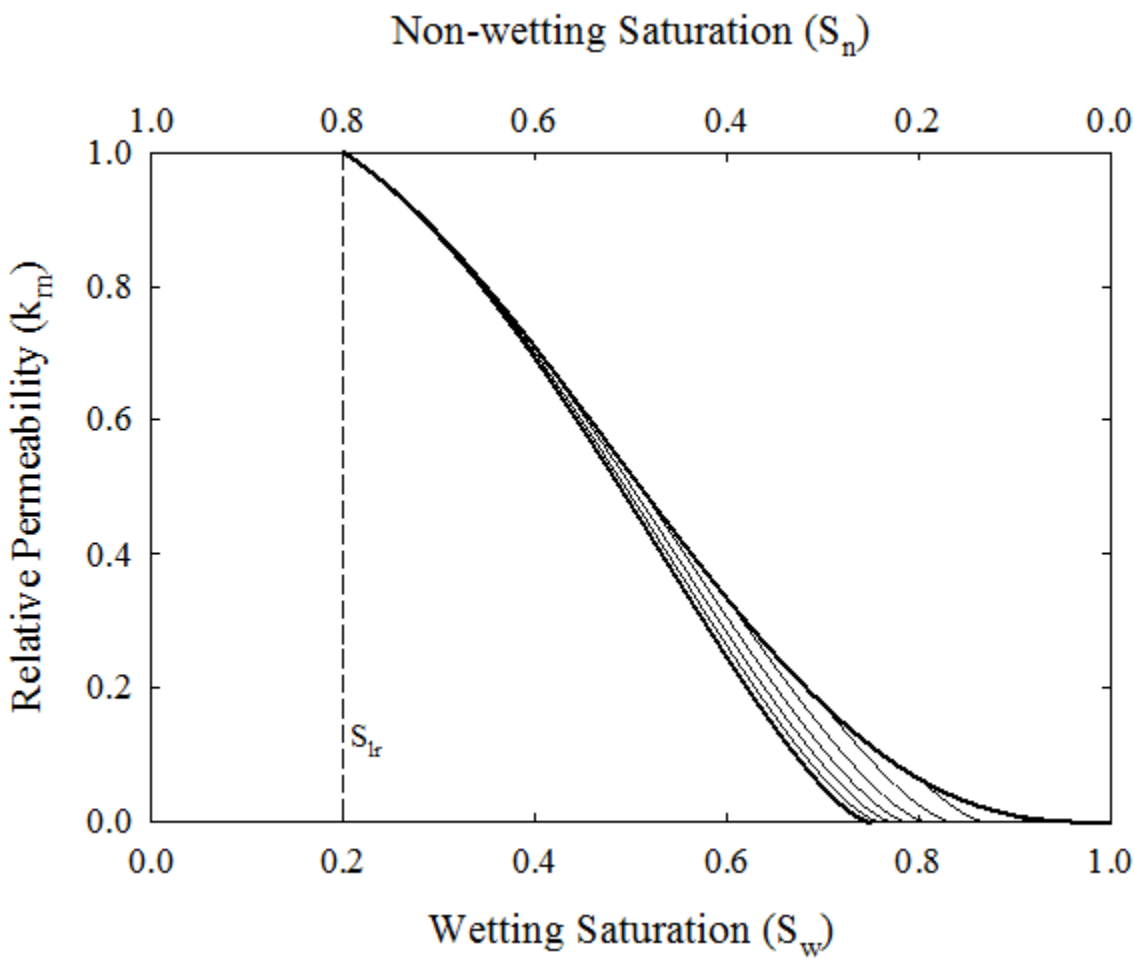

Figure 3.7 Example of the new hysteretic non-wetting phase relative permeability curve using the trapping model by Land (1968). Multiple potential wetting phase imbibition branches are shown for arbitrary turning-point saturations.

Relative permeability curve parameter	Parameter value
n	2
S_{lr}	0.2
S_{nr} max	0.25

Table 3.7: Hysteretic relative permeability curve parameters used in figure 3.7.

The capillary pressure curve used for the new hysteretic model is based on van Genuchten's equation (eq. 3.4). Figure 3.8 shows a hysteretic capillary pressure curve using the linear trapping model with different turning-point saturation values. Figure 3.9 shows a hysteretic capillary pressure curve using the trapping model by Land (1968) with different turning-point saturation values. The parameters for the models in figures 3.8 and 3.9 are shown in tables 3.8 and 3.9, respectively. It is important to note the continuous slope in the function at drainage-imbibition turning points.

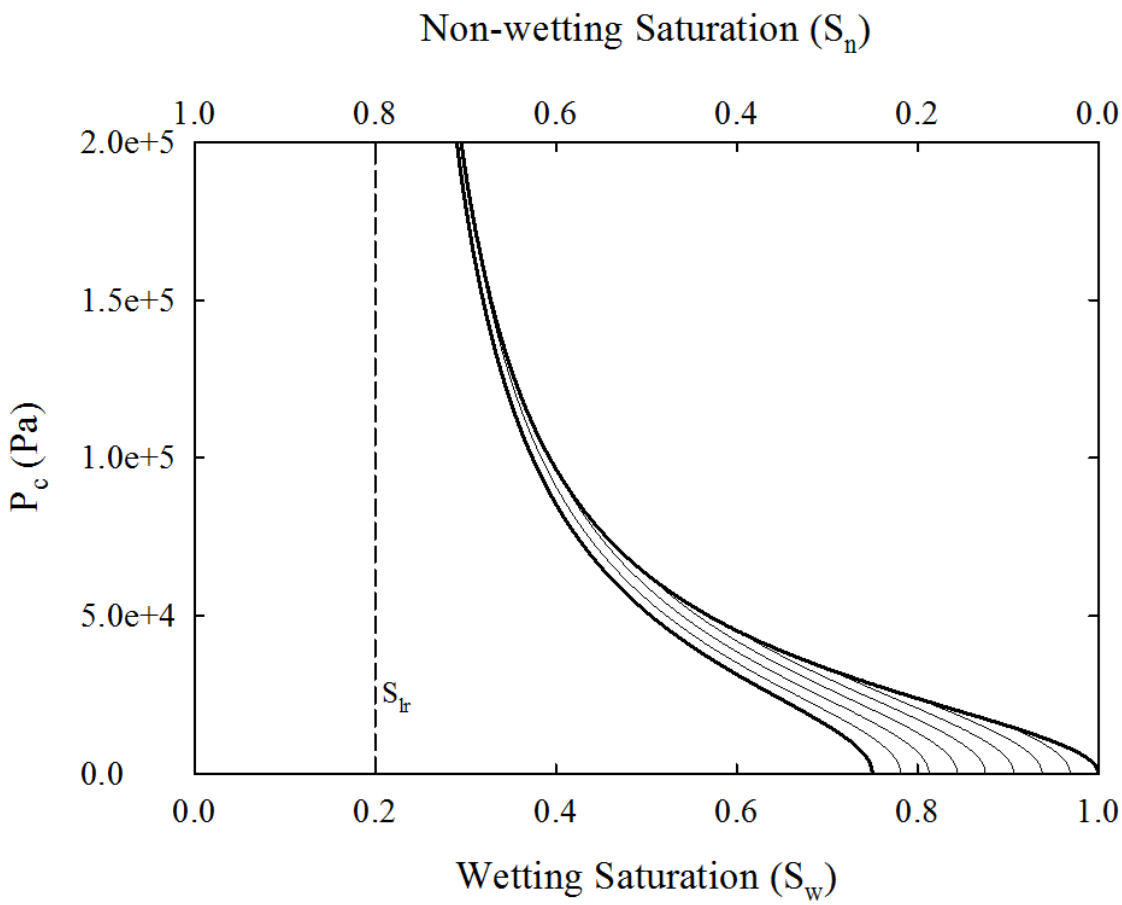

Figure 3.8 Example of the new hysteretic capillary pressure curve using a linear trapping model. Multiple potential wetting phase imbibition branches are shown for different turning-point saturations.

Capillary pressure curve parameter	Parameter value
n	2
S_{lr}	0.2
α	0.539
J_r	0.3125

Table 3.8: Hysteretic capillary pressure curve parameters used in figure 3.8.

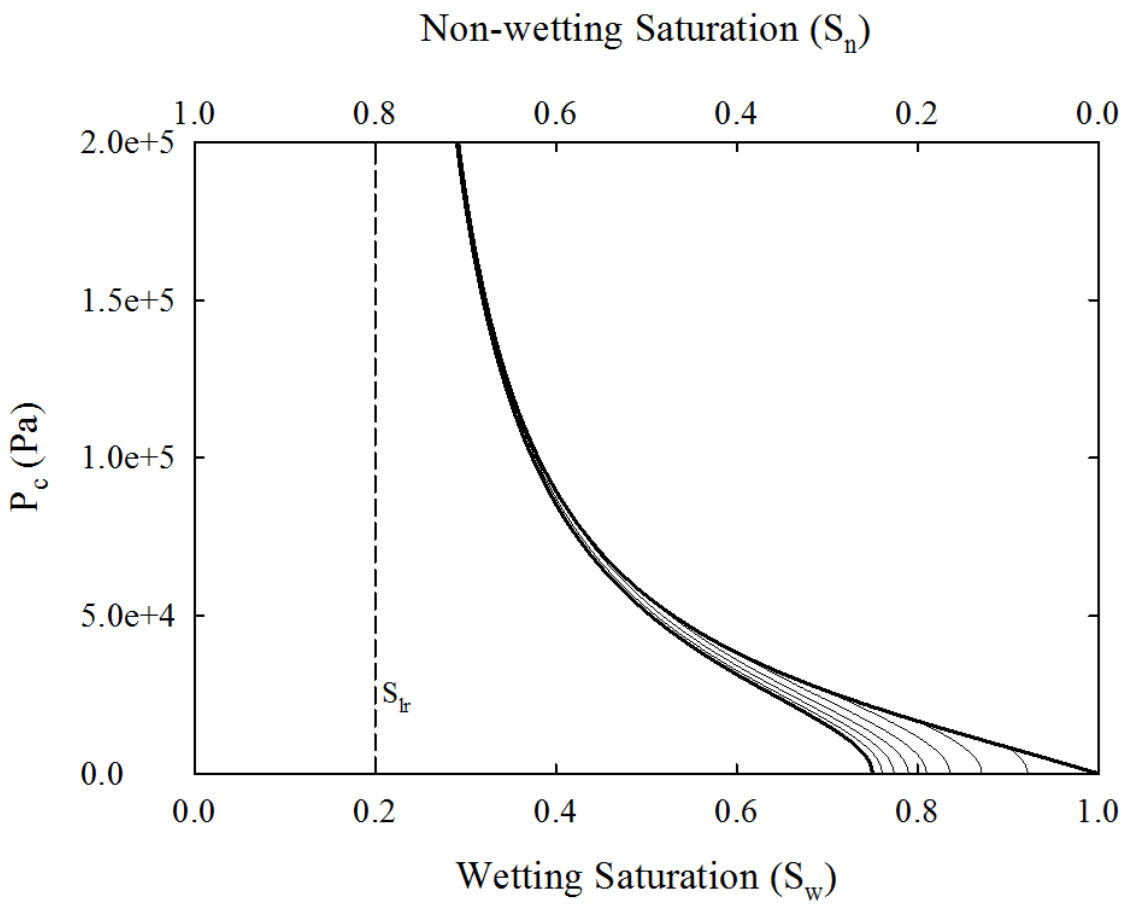

Figure 3.9 Example of the new hysteretic capillary pressure curve using the Land (1968) trapping model. Multiple potential wetting phase imbibition branches are shown.

Capillary pressure curve parameter	Parameter value
n	2
S_{lr}	0.2
α	0.539
S_{nr} max	0.25

Table 3.9: Hysteretic non-wetting phase capillary pressure curve parameters used in figure 3.9.

4.0 NUMERICAL SIMULATORS AND NEW MODEL IMPLEMENTATION

The numerical simulators used in this project are ECO2N (Pruess 2005) and TMVOC (Pruess and Battistelli 2002), both of which are modules of the TOUGH2 (Pruess 1999) numerical codes developed at the Lawrence Berkeley National Laboratory. These codes are capable of simulating multi-dimensional fluid and heat flows of multiphase, multicomponent fluid mixtures through porous and fractured media. ECO2N is specifically designed for applications to geologic sequestration of CO_2 in saline aquifers, capable of modeling isothermal or non-isothermal single phase or two-phase fluid mixtures of water, CO_2, and NaCl. The chemical reactions modeled by ECO2N include equilibrium phase partitioning of water and carbon dioxide between liquid and gaseous phases, and precipitation and dissolution of solid salt. TMVOC is capable of modeling non-isothermal flow of water, gas, and multicomponent mixtures of volatile organic chemicals (VOCs). A brief discussion of the numerical formulation of TOUGH2 is presented here.

4.1 Governing equations

TOUGH2 uses an integral finite difference method for solving mass and energy balance equations. The general form of the basic mass and energy balance equations can be written:

$$\frac{d}{dt}\int_V M^k dV = \int_\Gamma F^k \bullet n d\Gamma + \int_V q^k dV$$

where V represents an arbitrary flow volume, Γ is the surface area of V, k is the mass component or heat, F represents the flux term for mass or heat, q is the sink/source term, and n is a normal vector acting on surface element dΓ, pointing inward into V.

The general form of the mass accumulation term for the water or non-condensable components is

$$M^k = \phi \sum_\beta S_\beta \rho_\beta X_\beta^k$$

where ϕ represents the porosity of the medium, S_β is the saturation of phase β, ρ_β is density of phase β, X_β^k is the mass fraction of component k present in phase β

The advective mass flux is a sum over phases,

$$F^k = \sum_\beta F_\beta$$

where F_β represents the mass flux in phase β.

The individual phase fluxes are given by a multiphase extension of Darcy's law:

$$F_\beta = \rho_\beta q_\beta = -k \frac{k_{r\beta} \rho_\beta}{\mu_\beta} \left(\nabla P_\beta - \rho_\beta g \right)$$

where q_β is the darcy flux in phase β, k is the single phase permeability, $k_{r\beta}$ is the relative permeability to phase β, μ_β is the viscosity of phase β, ∇P_β is the pressure gradient in phase β, and g is the vector of gravitational acceleration.

The fluid pressure in phase β is given by

$$P_\beta = P + P_{c\beta}$$

where P is the pressure of a reference phase (usually the gas phase) and $P_{c\beta}$ is the capillary pressure of phase β.

The non-linear coupled mass balance equations are spatially and temporally discretized using the integral finite difference method. An iterative Newton-Raphson technique is implemented to linearize the equations. The resulting linear equations are solved with either a direct or iterative solver. For a more detailed discussion on the numerical solution methods used in the TOUGH2 codes, the reader should refer to Pruess et al. (1999).

4.2 New model implementation into TOUGH2

. During each Newton-Raphson iteration, the maximum non-wetting phase saturation is treated as a "secondary" variable, that is continuously updated during the iteration process as the primary variables change, so that the effect of the variable nonwetting trapping are fully incorporated in the Jacobian Matrix. At the end of each time step, the variable representing the maximum non-wetting phase saturation is updated accordingly, and stored in a different array. At the end of a simulation, the value of the maximum nonwetting saturation in each gridblock is written to the "SAVE" file so that a simulation may be restarted with the historical saturation values known.

In the case of CO_2 or NAPL dissolution, if the value of non-wetting phase saturation drops below the value of residual non-wetting phase saturation, the value of maximum non-wetting phase saturation is reset according to:

$$S_{n\max} = \frac{S_n}{f_r}$$

When preparing to run a simulation with TOUGH2, the characteristic curves and associated curve parameters for each material type are specified in the input file.

Different relative permeability curves and capillary pressure curves can be used by identifying unique call numbers that are associated with the appropriate subroutines in the source code. Separate options were given to use either the linear trapping model or the Land (1968) trapping model.

5.0 MODEL ASSESSMENT

5.1 One-dimensional simulations

The first assessment made with the new model was to simulate an experiment by Johnston and Adamski (2005). The objective of their experiment was to explore the relationship between maximum NAPL saturation and residual NAPL saturation using a decane retention cell. For the experiment, the water represented the wetting phase while the decane (or light non-aqueous phase liquid) represented the non-wetting phase. The experimental results are relevant to CO_2 modeling because CO_2 behaves similar to LNAPL in a deep saline formation where the CO_2 forms a separate phase that is less dense than the native brine. The multiphase saturation relationships between CO_2 and brine can be treated in a similar fashion to that of the NAPL and water. The results from the experiment showed a linear relationship between the maximum NAPL saturation and residual NAPL saturation.

5.1.1. Experiment overview

Figure 5.1 shows a diagram for the experiment, in which a retention cell held a core sample with a water reservoir and a decane reservoir connected to either end. The minimally disturbed Texas City 3.66 – 4.27 core sample measured 47 mm in diameter

and 50 mm in length and was classified as sand texture. A hydrophilic ceramic plate separated the core from the water reservoir while a hydrophobic ceramic plate separated the core from the decane reservoir. The plates were placed to ensure that decane would not leak into the water reservoir and that water did not leak into the decane reservoir. The elevation of the decane reservoir remained constant to ensure consistent pressure on the decane end of the cell, while the elevation of the water reservoir was varied to apply and release capillary pressure within the cell. The retention cell was subjected to cycles of subsequently increasing water suction to allow decane to flow into the core. The suction was released in between cycles to return capillary pressure back to zero and allow water to imbibe into the core, expelling the decane out of the core. Equilibration times for each step in the experiment ranged up to 1 month.

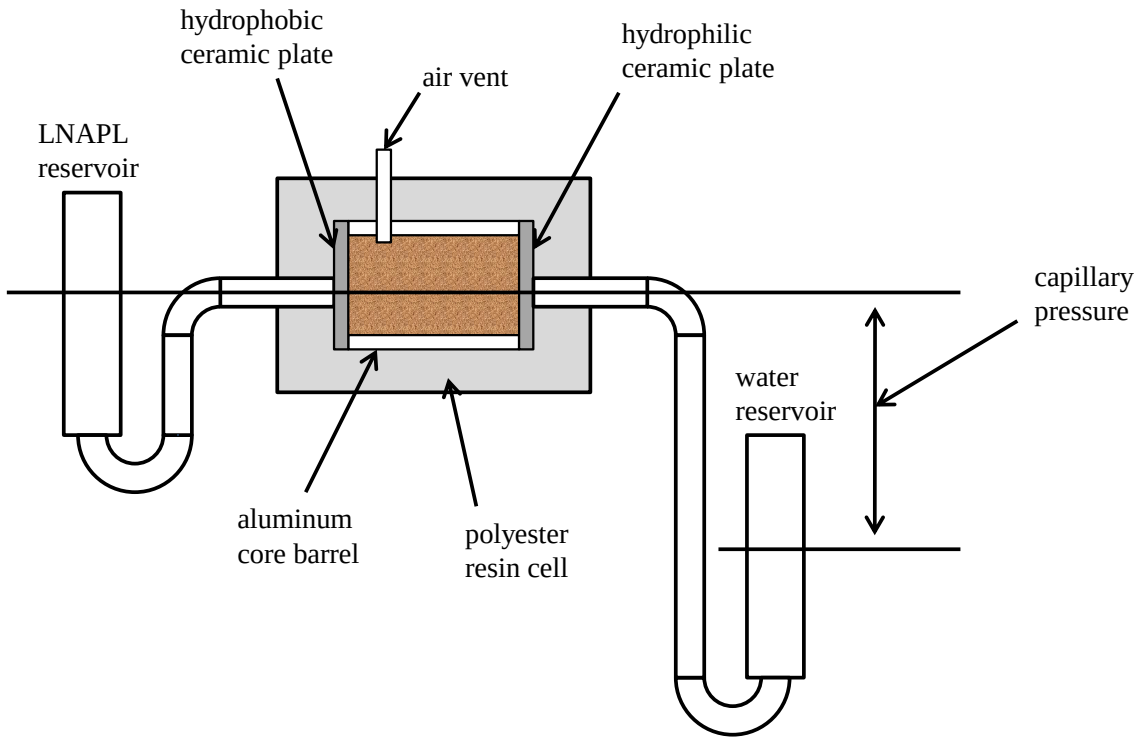

Figure 5.1 Experimental set up for Johnston and Adamski (2005) (adapted from Steffy et al. 1997).

Calculations for phase saturations were made by measuring the volume of water displaced from the sample, the volume of decane imbibed, and the total volume of decane in the core at the end of the experiment. The volumes were calculated from weight measurements of the reservoirs and core sample. Control reservoirs were maintained to account for evaporative losses.

Over the span of about 90 days, 6 NAPL flooding cycles were performed on the Texas City 3.66 – 4.27 m core sample. The measurements of residual NAPL saturations showed an approximate linear relationship with the measurements of the maximum

NAPL saturations. A value of 0.394 was given as the slope of the linear function (eq 3.6) for the Texas City 3.66 – 4.27 m core sample.

5.1.2. Modeling Approach

A 1-dimensional model was set up with TOUGH2-TMVOC to simulate this experiment. The Texas City 3.66 – 4.27 m core sample was represented by 10 grid-blocks in the center of the model, the ceramic plates were each represented by 2 grid-blocks on both ends of the core cells, and the reservoirs were each represented by 1 grid-block on both ends of the model. The cross-sectional area of the model was kept consistent with that of the core sample — 1.66E-03 m^2.

The hydraulic properties of the ceramic plates and the intrinsic permeability of the core sample were unknown, so estimated values were used for these parameters in the simulation (table 5.1).

The grid-blocks representing the core sample were initially fully saturated with water. The grid-blocks representing the water and decane reservoirs were initially fully saturated in water and decane, respectively, and were held at the desired conditions— the decane reservoir grid-block kept at a constant pressure while the pressure of the water reservoir was controlled to match the experimental conditions. The actual times and values of pressure change were obtained through personal communication with Colin Johnston (2010) and were used in the pressure control for the water reservoir grid-block.

Model parameter	Parameter value
Grain density of core sample	2600 kg/m^3
Porosity of core sample	0.384
Permeability of core sample	5.00E-12 m^2
Grain density of ceramic plates	2600 kg/m^3
Porosity of ceramic plates	0.7
Permeability of ceramic plates	1.00E-15 m^2

Table 5.1: Model parameters for the materials used to simulate experiment by Johnston and Adamski (2005).

5.1.3. Characteristic curves

The grid-blocks representing the hydrophilic plate were given a high non-wetting phase entry pressure in order to repel the decane and the grid-blocks representing the hydrophobic plate were given a large negative capillary pressure to repel water. The value of f_r from Johnston and Adamski (2005) was used to calculate S_{nr} in the hysteretic relative permeability function. The fitted van Genuchten parameters from Johnston and Adamski 2005 were used for the capillary pressure function (which was not hysteretic in this simulation). Table 5.2 shows the characteristic curve parameters used for the end plates and the core sample in the simulation.

Material	α (Pc)	n (k_r, Pc)	S_{nr}(k_r, Pc)	f_r (k_r, Pc)	S_{lr} (k_r, Pc)
Core	2.44	7.12, 7.12	n/a, 0	0.394, n/a	0.2, 0.2
Hydrophilic Plate	0.8	9, 15	0, 0	n/a, n/a	0.89, 0.5
Hydrophobic plate	-0.8	9, -15	0, 0	n/a, n/a	0, 0.5

Table 5.2: Characteristic curve parameters for the material types used in the simulation of Johnston and Adamski (2005).

5.1.4. Results and Discussion

The simulation of the experiment was run with non-hysteretic characteristic curves to demonstrate the inaccuracy the use of non-hysteretic curves has on the prediction of the saturation in the core sample. Figure 5.2 shows the result of a non-hysteretic simulation run with a single S_{nr} value of 0. During intermittent times of applied suction, the NAPL saturation returns to 0. Figure 5.3 shows the result of a non-hysteretic simulation run with a single S_{nr} value of 0.15. It is clear from the results that the non-hysteretic simulations are unable to predict the variable value of trapped NAPL saturation in the core sample.

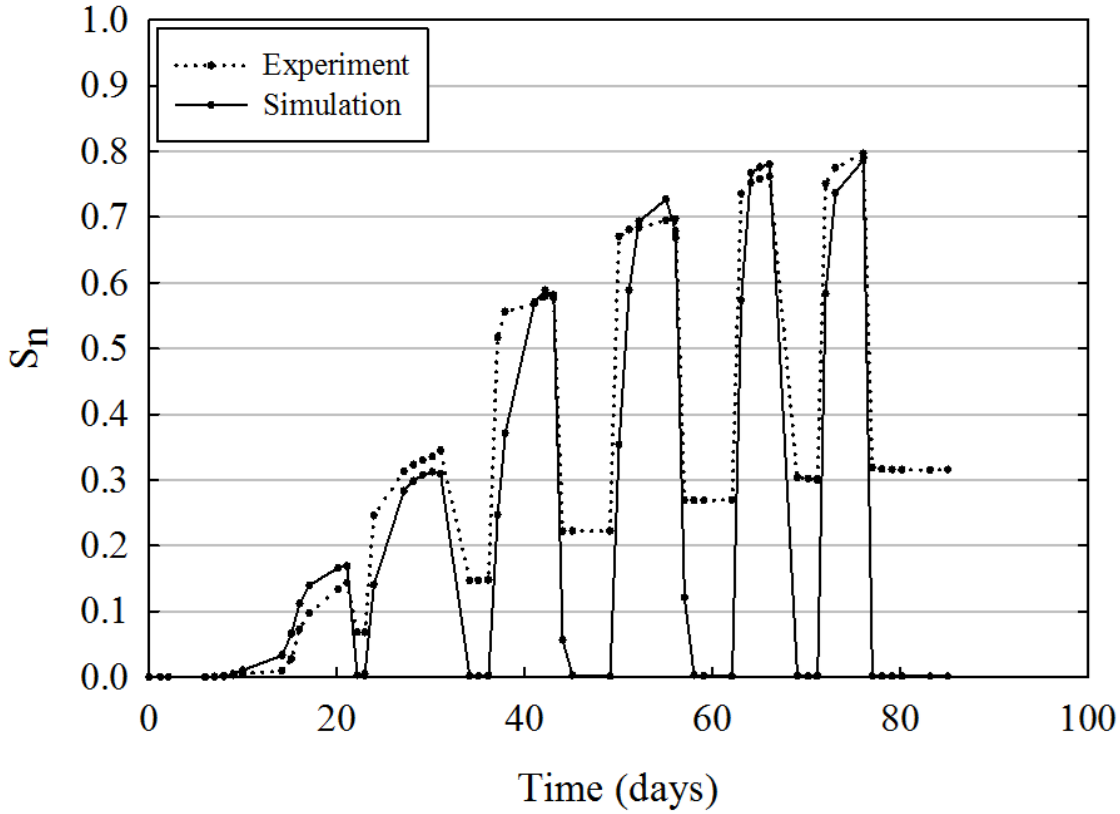

Figure 5.2 Results from a non-hysteretic simulation of the experiment by Johnston and Adamski (2005) using a single S_{nr} value of 0.

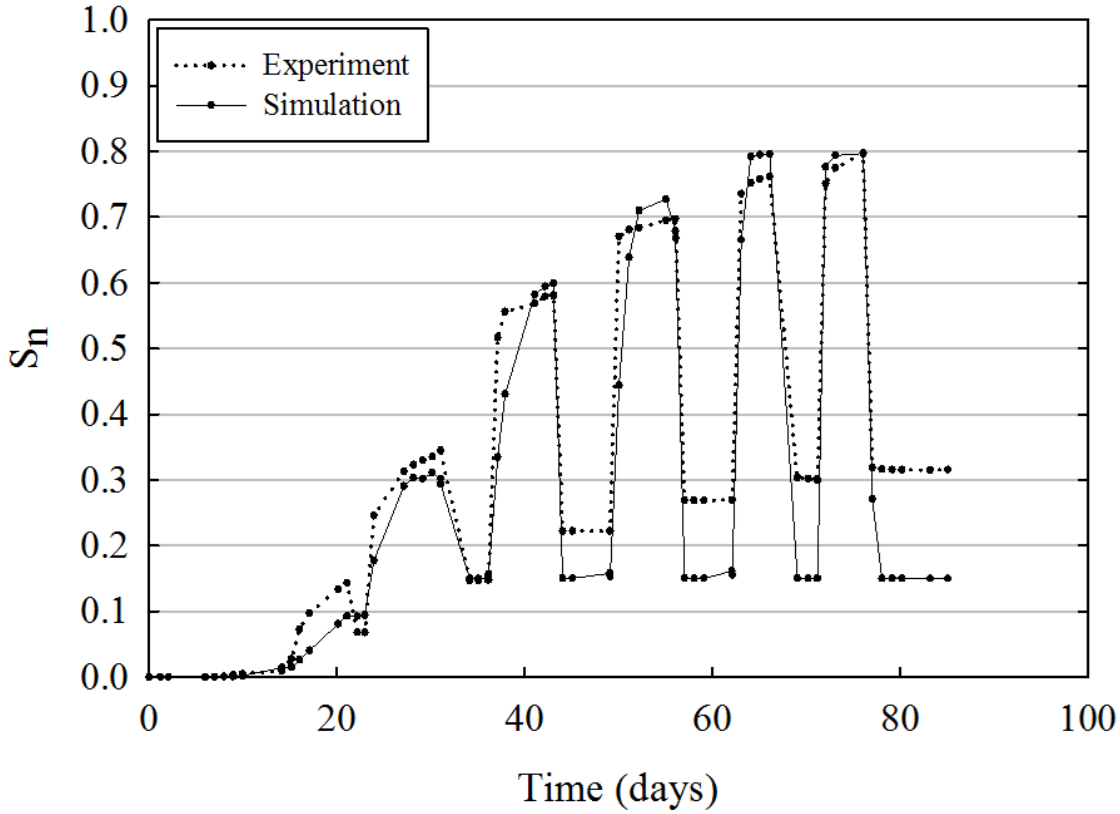

Figure 5.3 Results from a non-hysteretic simulation of the experiment by Johnston and Adamski (2005) using a single S_{nr} value of 0.15.

Results from the simulation using the new hysteretic relative permeability function compare favorably to the experimental results (figure 5.4). The slight differences between the simulated and experimental results can be seen specifically around 40 days- where the simulated NAPL saturation in the core sample does not reach the next maximum NAPL saturation as quickly as the experimental results show. This difference could be due to the use of estimated values of intrinsic permeability for the ceramic plates and core sample in the simulation. Another discrepancy between the simulated and

experimental results lies in the slight difference in some of the values of initial- and residual NAPL saturation. This is most likely the result of the use of the approximate value of the slope of the linear relationship between initial- and residual NAPL saturation obtained from the experimental results used as the exact slope of the linear function for the calculation of residual NAPL saturation for the simulation.

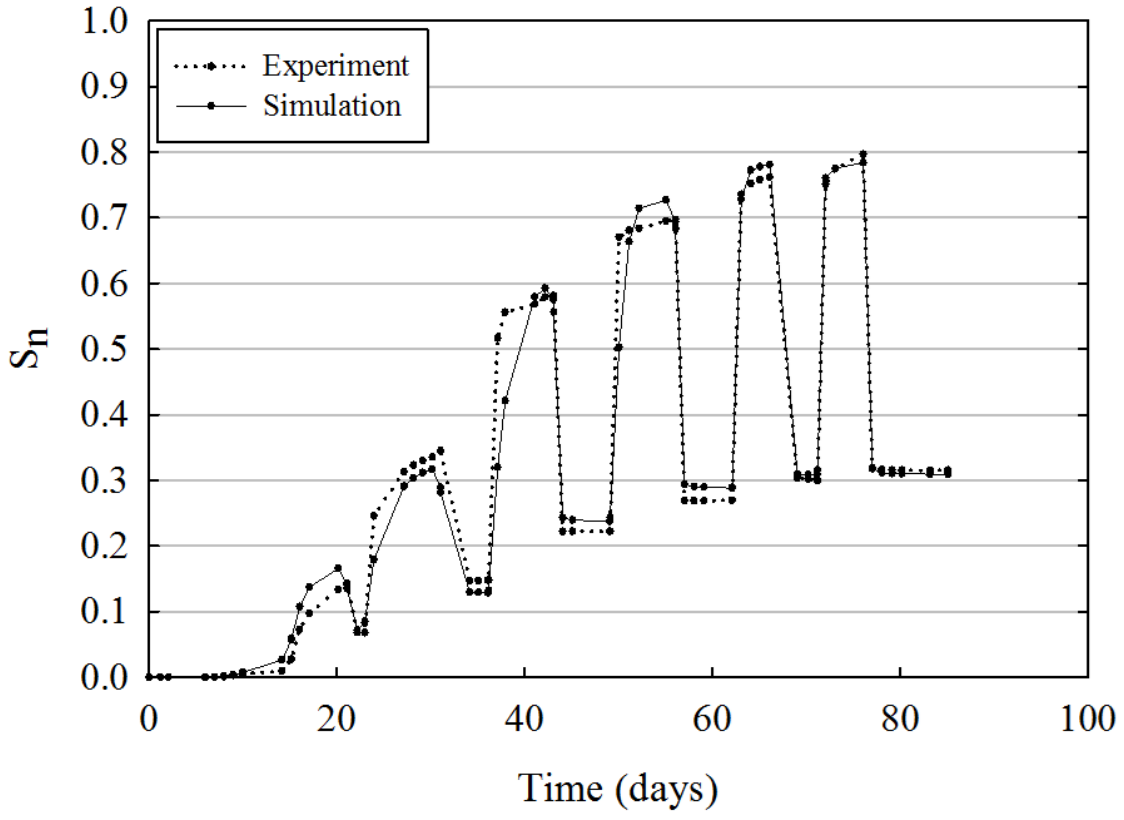

Figure 5.4 Simulation results plotted with experimental results from Johnston and Adamski (2005). Data from the experiment are shown by the measurements of water flowing out of the retention cell.

5.2 Two-dimensional simulations

The second assessment made with the new hysteretic model was to compare simulation results to a similar hysteretic simulation by Doughty (2007). The objective of Doughty's study was to compare the behavior of simulations of CO_2 injection using her hysteretic characteristic curves and using typical non-hysteretic characteristic curves. The simulation from her study that was recreated was a 2-dimensional simulation of CO_2 injection and leakage from the storage formation to the surface.

5.2.1. Modeling Approach

Doughty's model was a 2-dimenstional injection into a 100 m thick interval with leakage through a homogeneous zone 1000 m thick. Her model extended radially to 40,000 m, and was divided into 61 layers each with 41 gird-blocks. The layers were 20 m thick except for a few thinner layers near the surface. The grid-blocks were 20 m wide extending to 600 m, and then increased steadily to produce an infinite acting model. Both her injection formation and overlying formation were homogeneous, with a vertical permeability of 100 md and horizontal permeability of 200 md. The model was initially fully brine-saturated with a salinity of 100,000 ppm. The model was non-isothermal and followed a geothermal gradient of 30°C/km with the surface and bottom of the model held constant at 15°C and 48°C, respectively. Her simulation began by injecting 900,000 tons of CO_2 over a period of 30 days, with redistribution for 1,000 years.

To help ensure an accurate comparison of the behavior of the hysteretic formulations, we used the TOUGH2 input files for her simulation (Doughty, personal communication, 2010). It was noticed that her published simulations were carried using

ECO2, an older version of the TOUGH2 module ECO2N. A major difference between the two modules is that ECO2N includes the density-effect that CO_2 has in the aqueous phase once dissolved. This turns out to have a significant effect on the results at late simulation times. Doughty (personal communication, 2010) also provided an updated simulation using ECO2N and shared her new (unpublished) results. The comparison shown here uses these new simulations results.

In addition to running a simulation with the new hysteretic characteristic curves, two non-hysteretic cases were simulated to further illustrate the comparison between the new hysteretic model and the hysteretic model from Doughty (2007). The same input files were used for the simulation to ensure consistency between the hysteretic and non-hysteretic models. One non-hysteretic case used a residual gas phase saturation (S_{gr}) value of zero and the other case used an S_{gr} value of 0.25. Doughty (2007) employed similar non-hysteretic simulations to illustrate that non-hysteretic models are unable to fully capture the dynamic plume evolution. The non-hysteretic simulations here are run with the Charbeneau (2007) relative permeability function and van Genuchten (1980) capillary pressure function. Other than the constant value of S_{nr}, model parameters are kept consistent with that of the hysteretic simulations.

5.2.2. Fitting the characteristic curves

The new hysteretic method used here alters the shape of the primary drainage relative permeability and capillary pressure curves. In order to account for this, the parameter values in our characteristic curves were adjusted so that the primary wetting phase drainage curves were similar to those used in Doughty's model. Also, to be

consistent with Doughty's approach, the same method for calculating residual CO_2 saturation was used. Eq. 3.9 shows the modified version of the Land 1968 trapping model used in both Doughty's simulation and ours. Figures 5.5 and 5.6 show the curves that were fit to Doughty's capillary pressure curve and non-wetting phase relative permeability curve, respectively. Table 5.3 shows both the fitted parameters used for our hysteretic capillary pressure curve and the parameters used in Doughty's hysteretic capillary pressure curve. Table 5.4 shows both the fitted parameters used for our hysteretic non-wetting phase relative permeability curve and the parameters used in Doughty's hysteretic non-wetting phase relative permeability curve. In an effort to achieve comparable CO_2 plume migration in our simulation, the characteristic curves were fit the closest at low CO_2 saturation (0-5% S_g).

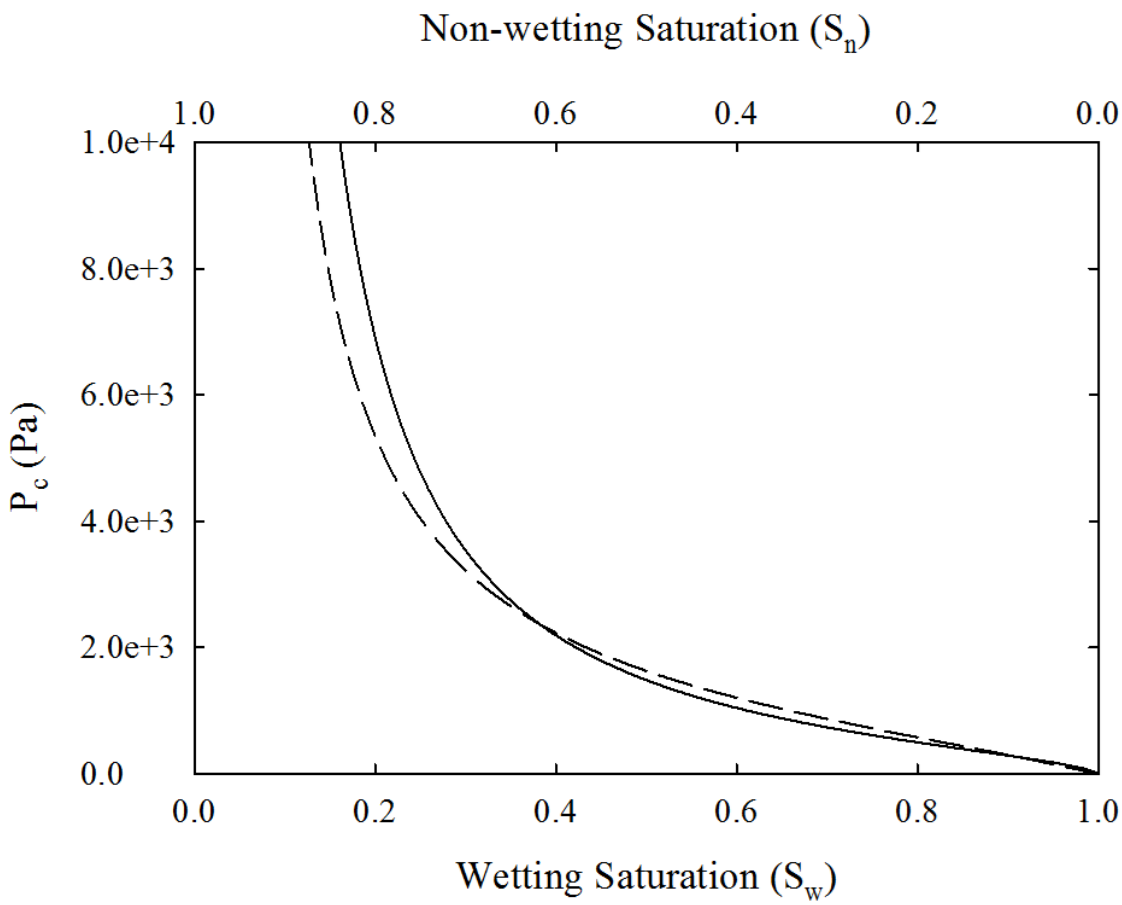

Figure 5.5: Main wetting phase drainage capillary pressure curve based on van Genuchten (1980) (dashed line) that best fit the main wetting phase drainage capillary pressure curve (solid line) from Doughty (2007).

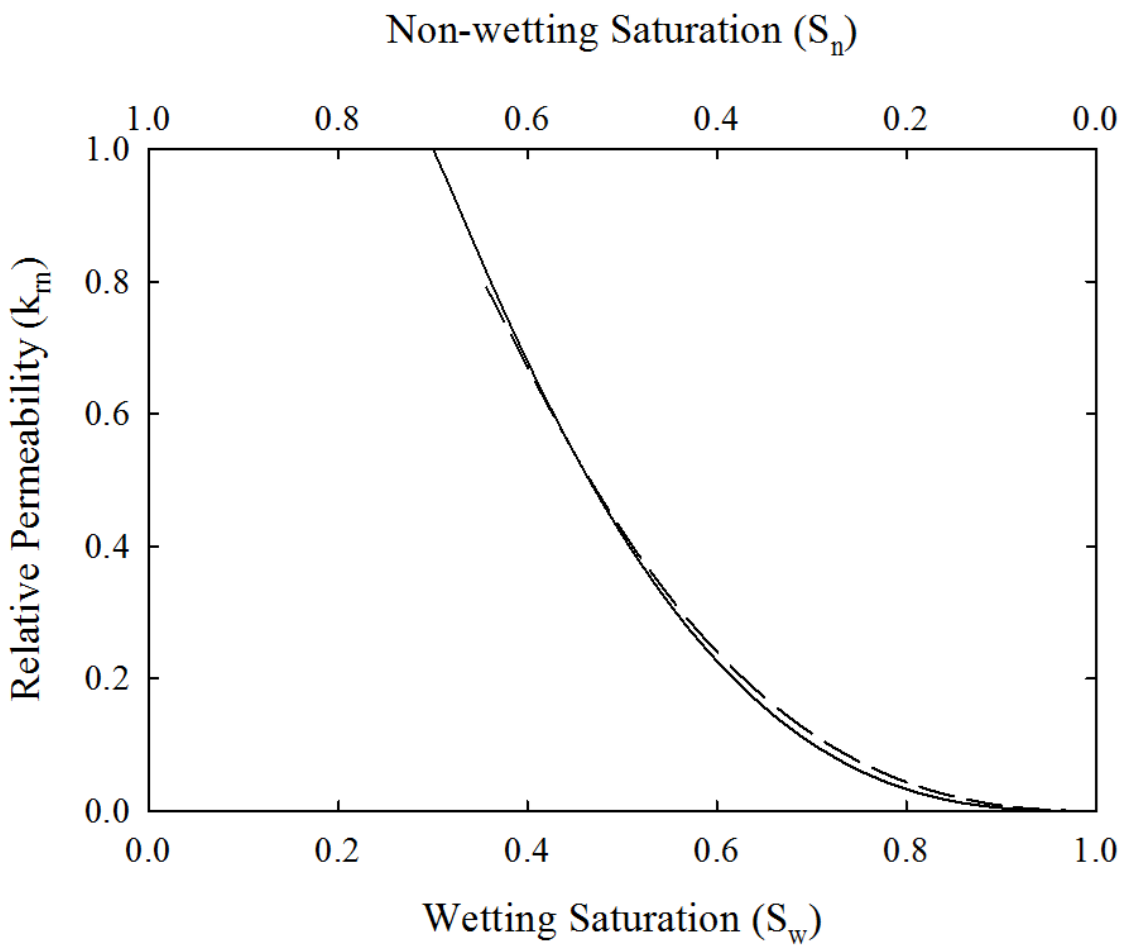

Figure 5.6 Main wetting phase drainage non-wetting phase relative permeability curve based on Charbeneau (2007) (dashed) that best fit the main wetting phase drainage non-wetting phase relative permeability curve (solid line) from Doughty (2007).

Model parameter	Fitted value	Doughty (2007) value
n	2.94	1.7
S_{lr}	0.2	0.03
α	0.53933	0.737293
S_{gr} max	0.25	0.25

Table 5.3: Hysteretic capillary pressure curve parameters for both the fitted curve and the curve used in Doughty (2007).

Model parameter	Fitted value	Doughty (2007) value
n	2.083	12
S_{lr}	0.3	0.3
S_{gr} max	0.25	0.25

Table 5.4: Hysteretic relative permeability curve parameters for both the fitted curve and the curve used in Doughty (2007).

5.2.3. Results and Discussion

Figure 5.7 shows the results from the non-hysteretic simulations; one case with an S_{gr} value of zero and another case with an S_{gr} value of 0.25. The first case ($S_{gr} = 0$) predicts a completely mobile CO_2 plume, and by 1,000 years all of the CO_2 has leaked to the surface. The second case ($S_{gr} = 0.25$) shows a fairly immobile plume, the CO_2 never reaches the surface and remains trapped indefinitely.

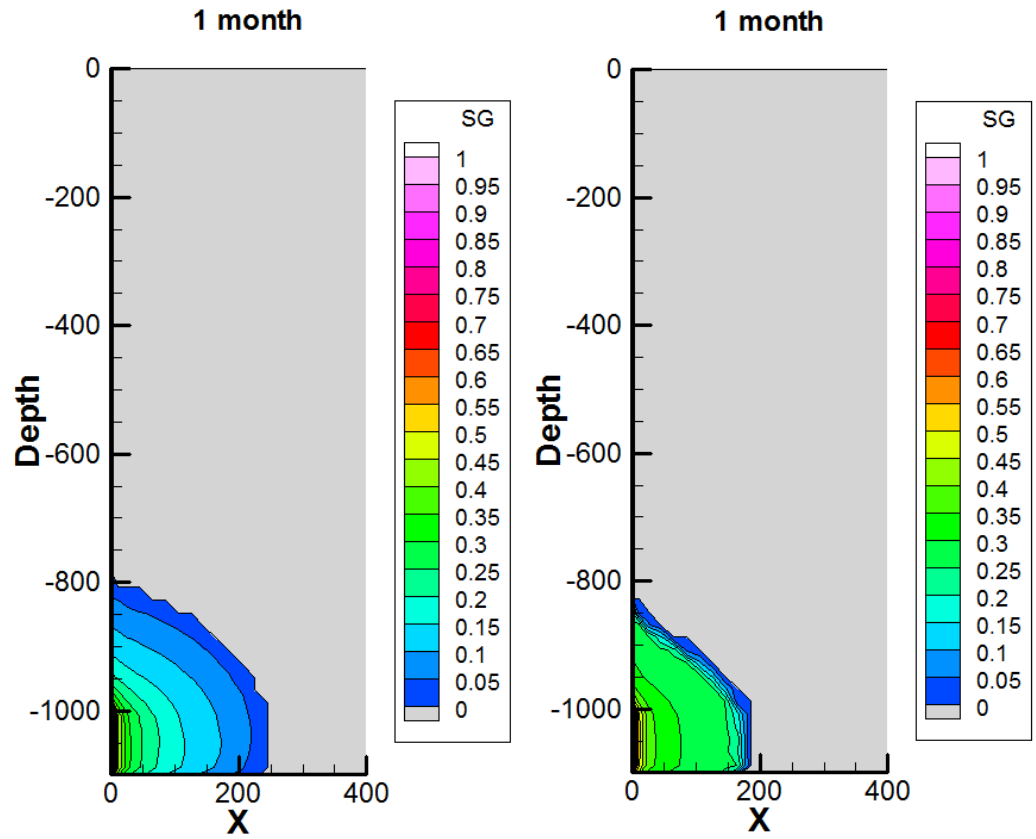

Figure 5.7 (a & b) Non-hysteretic simulations with S_{gr} = 0 (on left) and S_{gr} = 0.25 (on right).

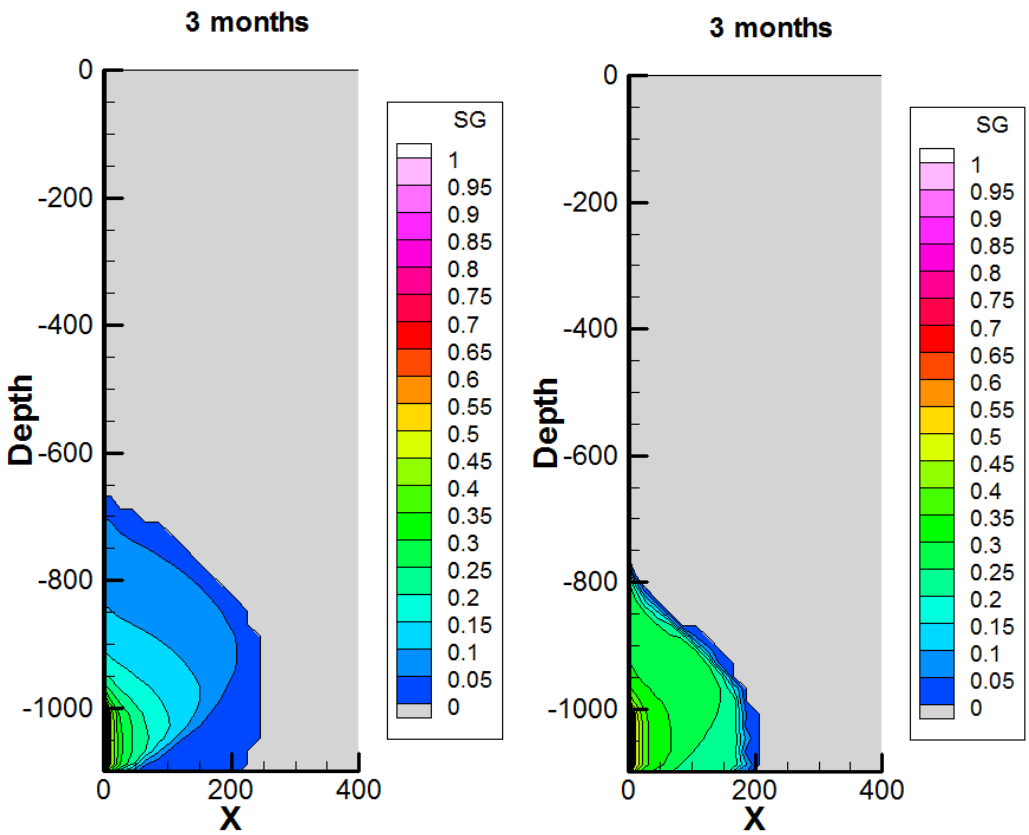

Figure 5.7 (c & d) Non-hysteretic simulations with S_{gr} = 0 (on left) and S_{gr} = 0.25 (on right).

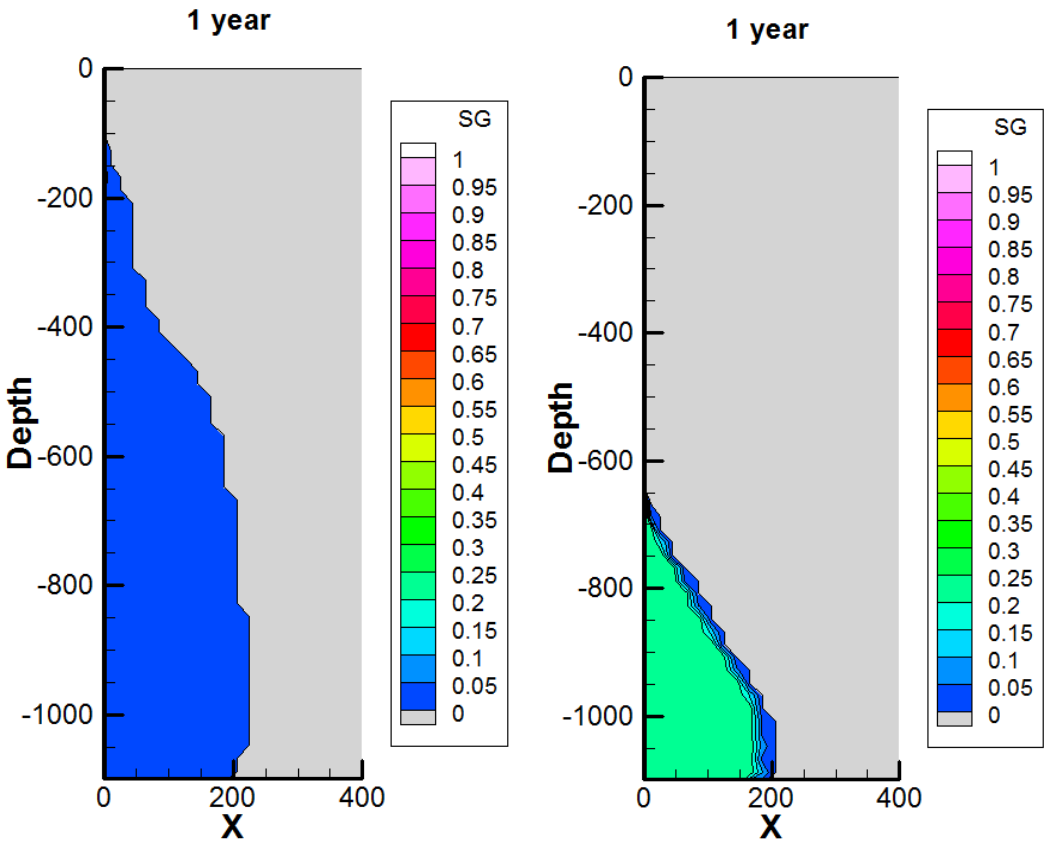

Figure 5.7 (e & f) Non-hysteretic simulations with S_{gr} = 0 (on left) and S_{gr} = 0.25 (on right).

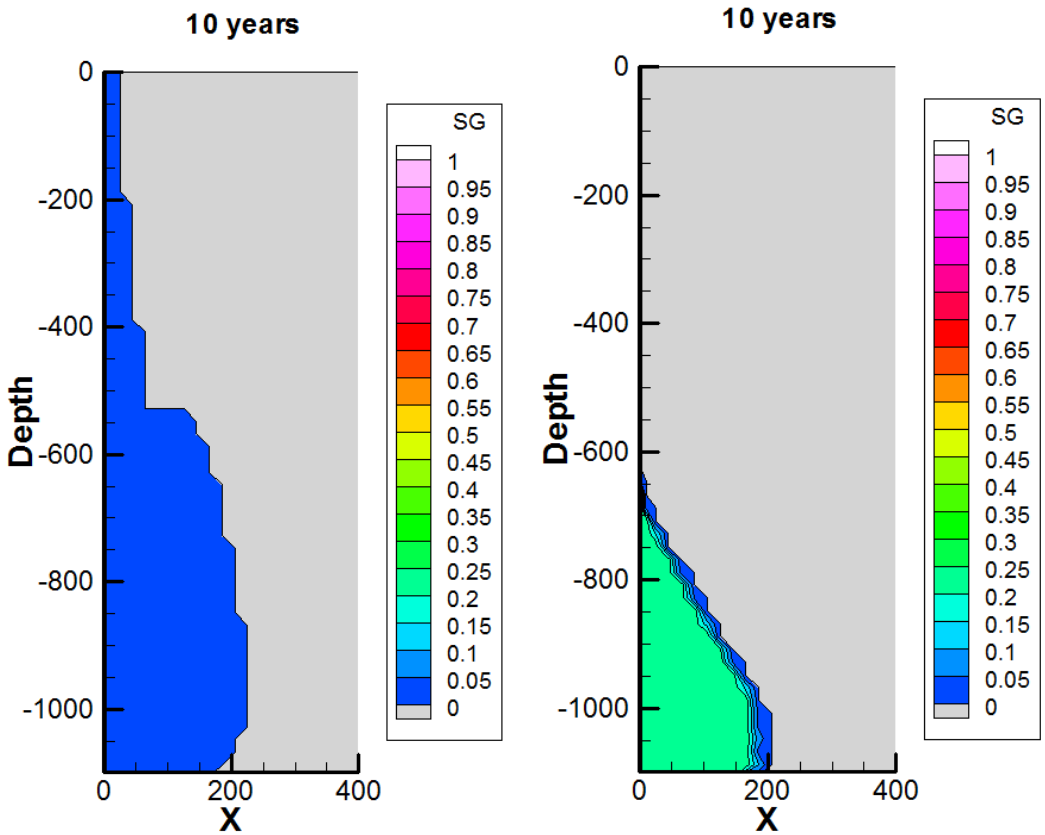

Figure 5.7 (g & h) Non-hysteretic simulations with S_{gr} = 0 (on left) and S_{gr} = 0.25 (on right).

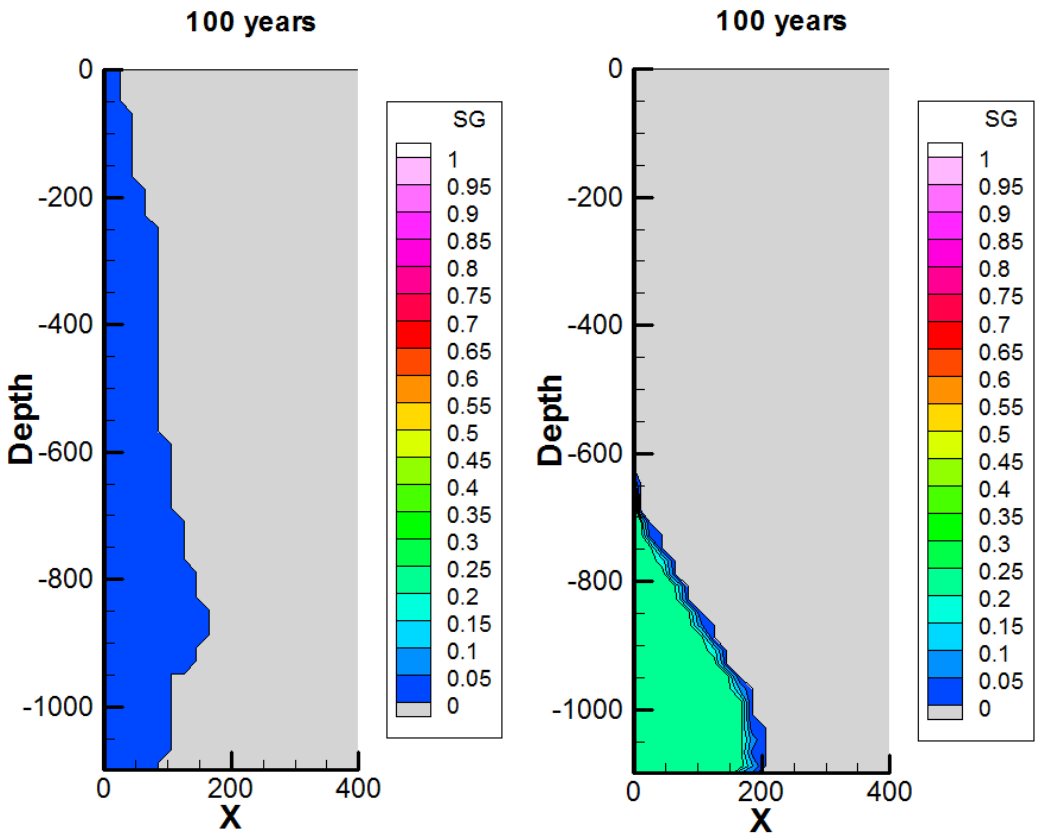

Figure 5.7 (i & j) Non-hysteretic simulations with S_{gr} = 0 (on left) and S_{gr} = 0.25 (on right).

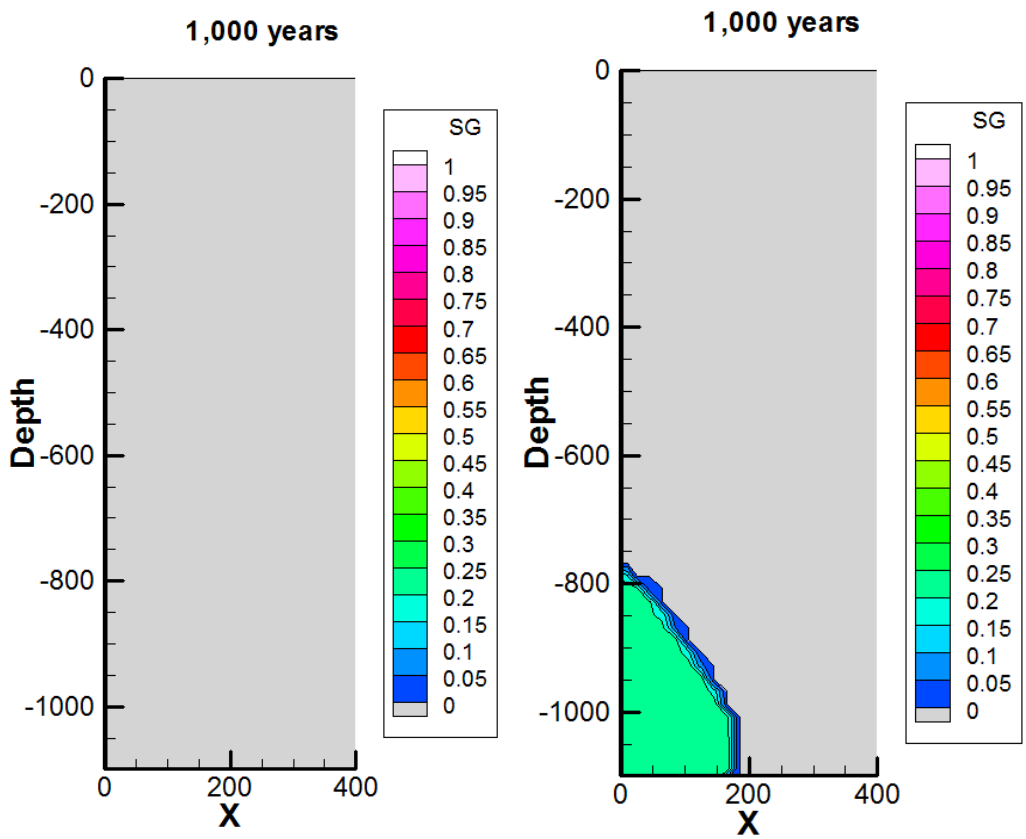

Figure 5.7 (k & l) Non-hysteretic simulations with S_{gr} = 0 (on left) and S_{gr} = 0.25 (on right).

Figure 5.8 shows the results of both Doughty's simulation and our simulation. Both models from Doughty (2007) and the new hysteretic model predict CO_2 plumes of an intermediate mobility compared to the non-hysteretic simulations. Doughty's model predicts a slighty more mobile CO_2 plume than our model predicts; seen at 10 and 100 years, where the 5% CO_2 saturation contour reaches a depth of about 500 m for Doughty's simulation and a depth of about 600 m for our simulation. The new model predicts a CO_2 plume of similar shape to Doughty's model, and the final snapshot at 1,000 years shows a comparable size of CO_2 plume. The simulation results compare favorably and confirm that the new and simplified hysteretic CO_2 trapping function is able to reproduce the essential features of more complicated hysteretic models.

Plots of CO_2 saturation as a function of time for three distinct elements on the simulation grid further show the difference between the non-hysteretic simulations and the hysteretic simulations. The locations chosen represent depths of 700 m and 900 m on the radial axis of the grid (figures 5.9 and 5.10, respectively) and a 1,000 m depth at 100 m away from the radial axis (figure 5.11). The four models predict the highest CO_2 saturations at early simulation time, then variable behavior as simulation time progresses. The non-hysteretic high S_{gr} case retains CO_2 saturation around 25% for most of the simulation, but at 700 m of depth on the radial axis the CO_2 saturation drops to 0 due to dissolution of the CO_2 phase. The non-hysteretic low S_{gr} case predicts that CO_2 saturation quickly drops to 0 due to the S_{gr} being set to 0. The two hysteretic cases show predictions of CO2 saturation with intermediate behavior, but complete CO_2 dissolution by 1,000 year simulation time.

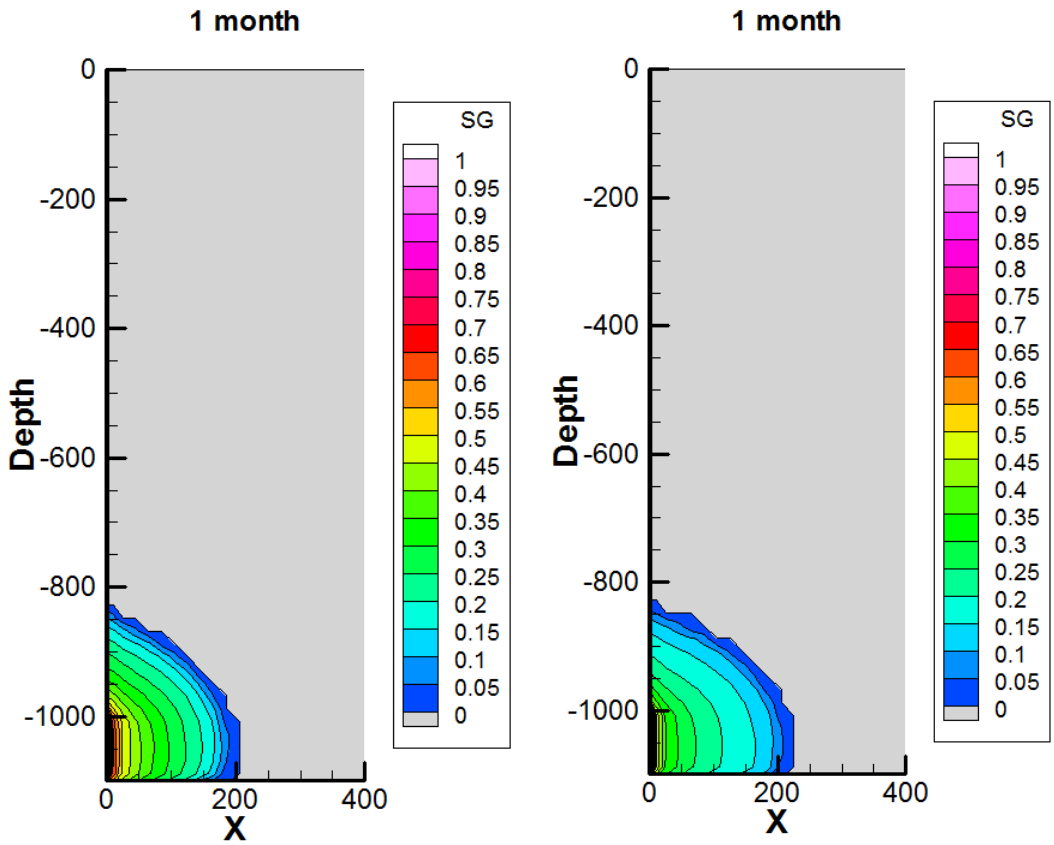

Figure 5.8 (a & b) Simulation results from Doughty (2007) on left, and the new hysteretic simulation on right.

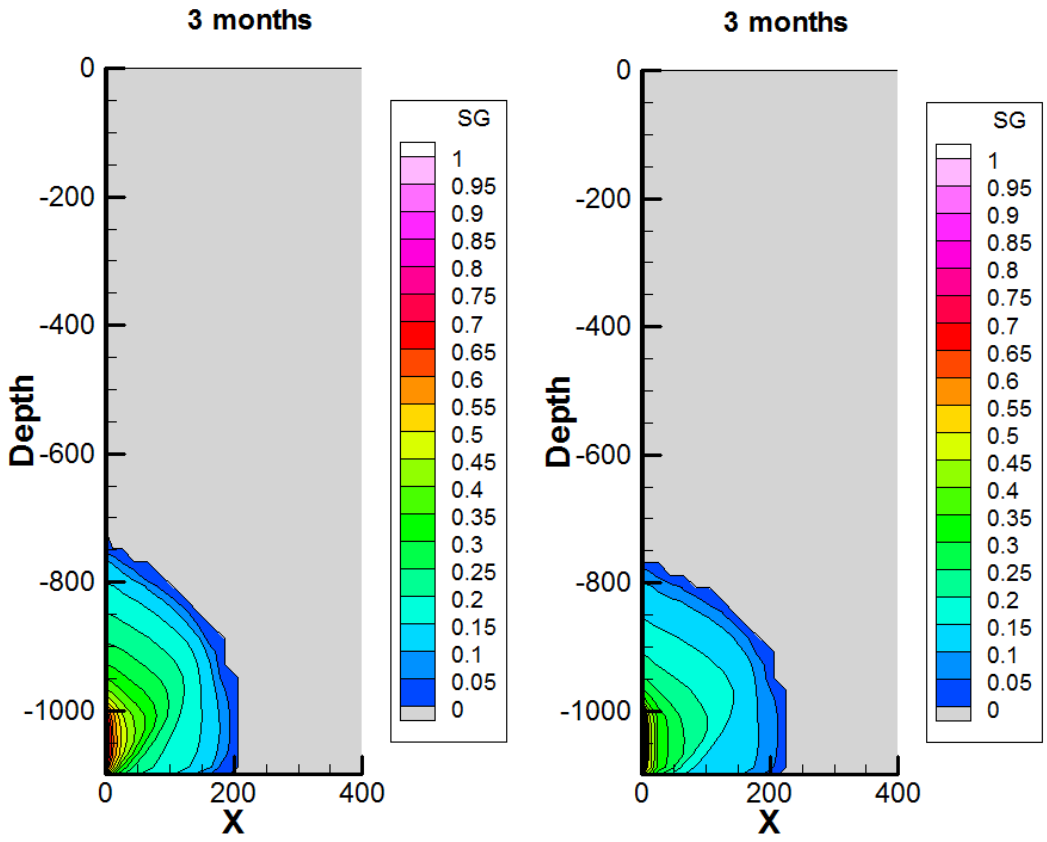

Figure 5.8 (c & d) Simulation results from Doughty (2007) on left, and the new hysteretic simulation on right.

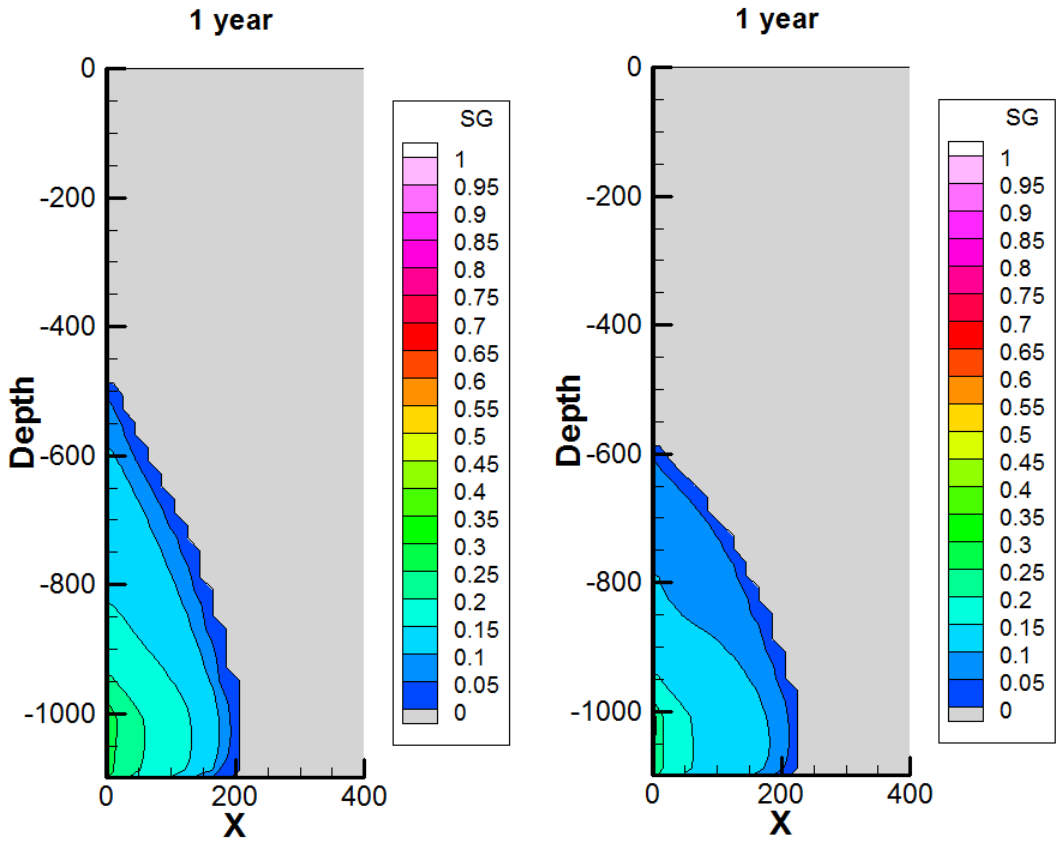

Figure 5.8 (e & f) Simulation results from Doughty (2007) on left, and the new hysteretic simulation on right.

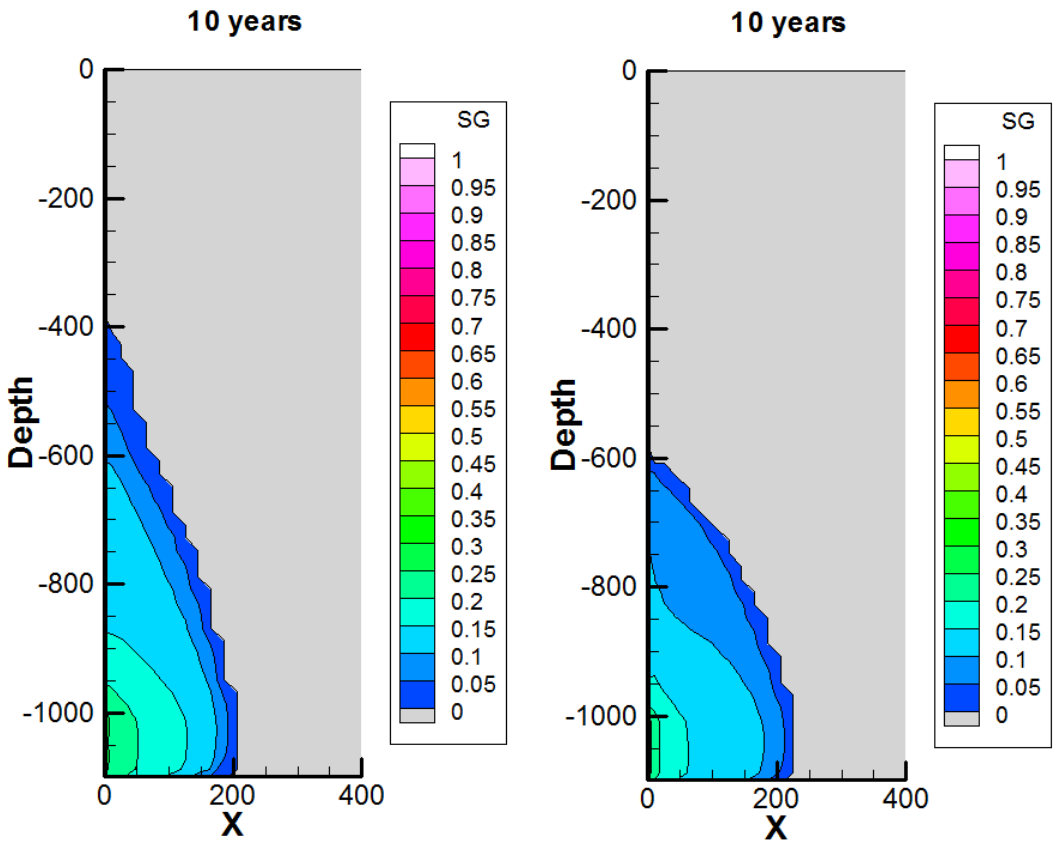

Figure 5.8 (g & h) Simulation results from Doughty (2007) on left, and the new hysteretic simulation on right.

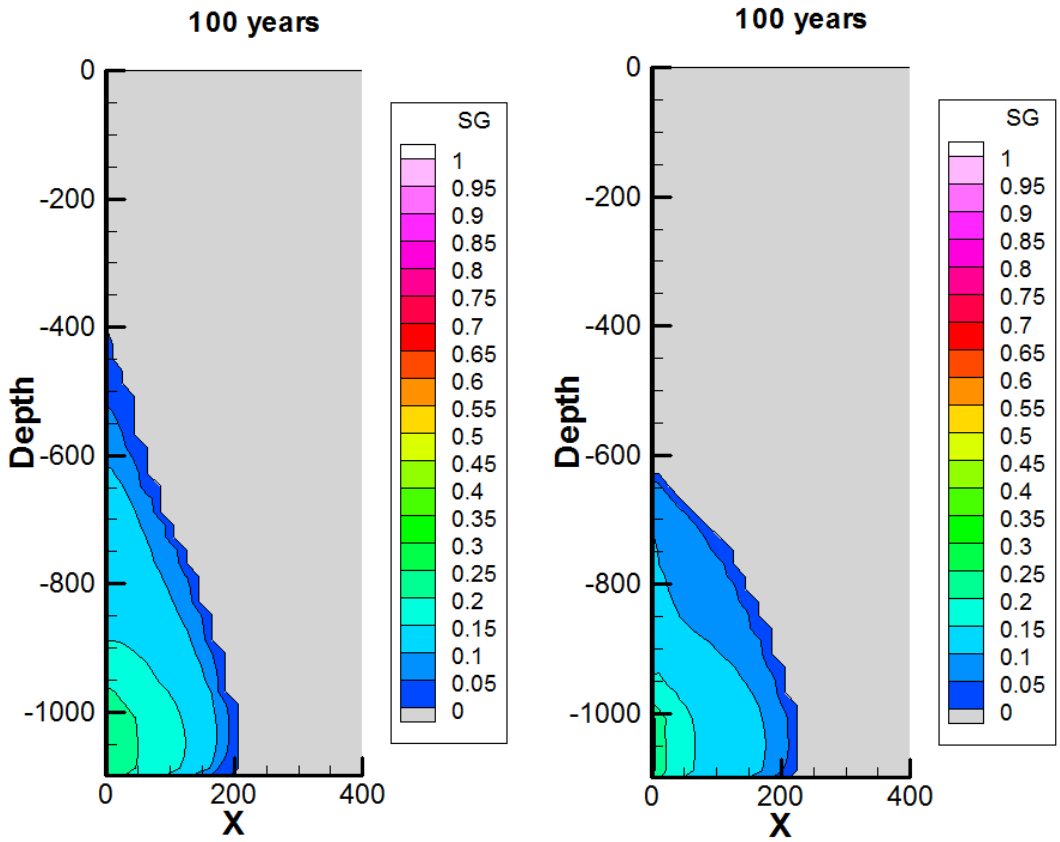

Figure 5.8 (i & j) Simulation results from Doughty (2007) on left, and the new hysteretic simulation on right.

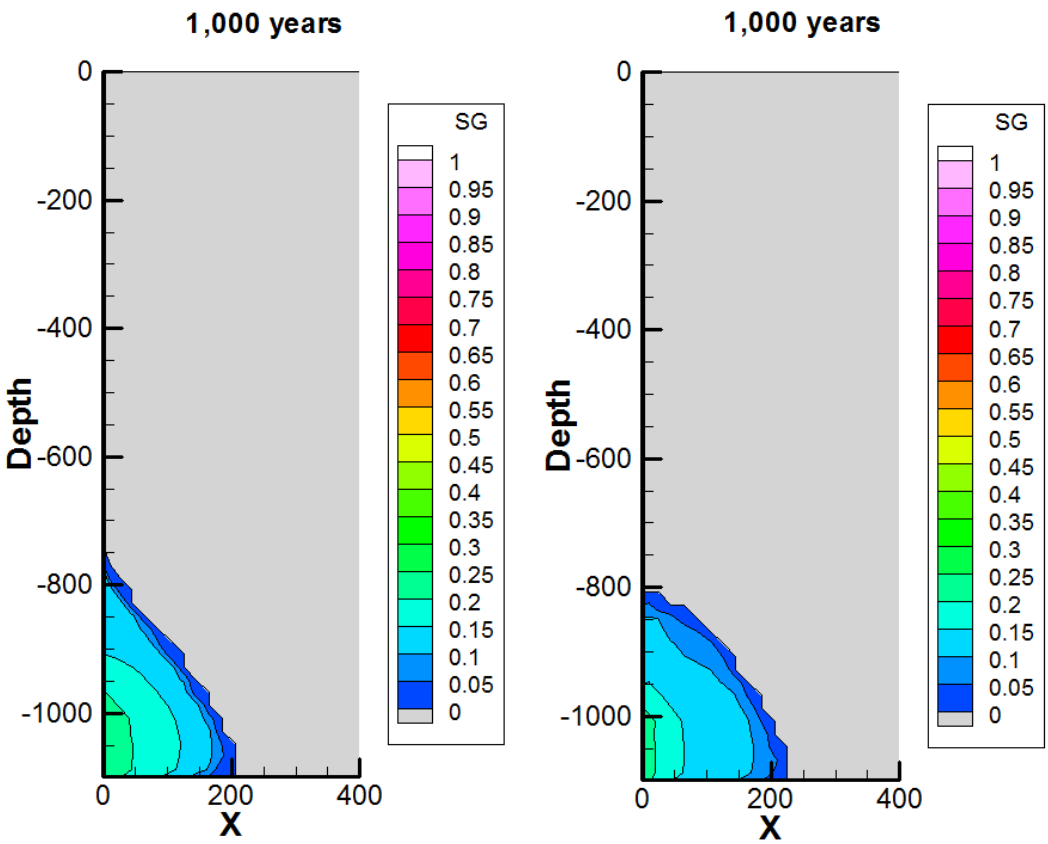

Figure 5.8 (k & l) Simulation results from Doughty (2007) on left, and the new hysteretic simulation on right.

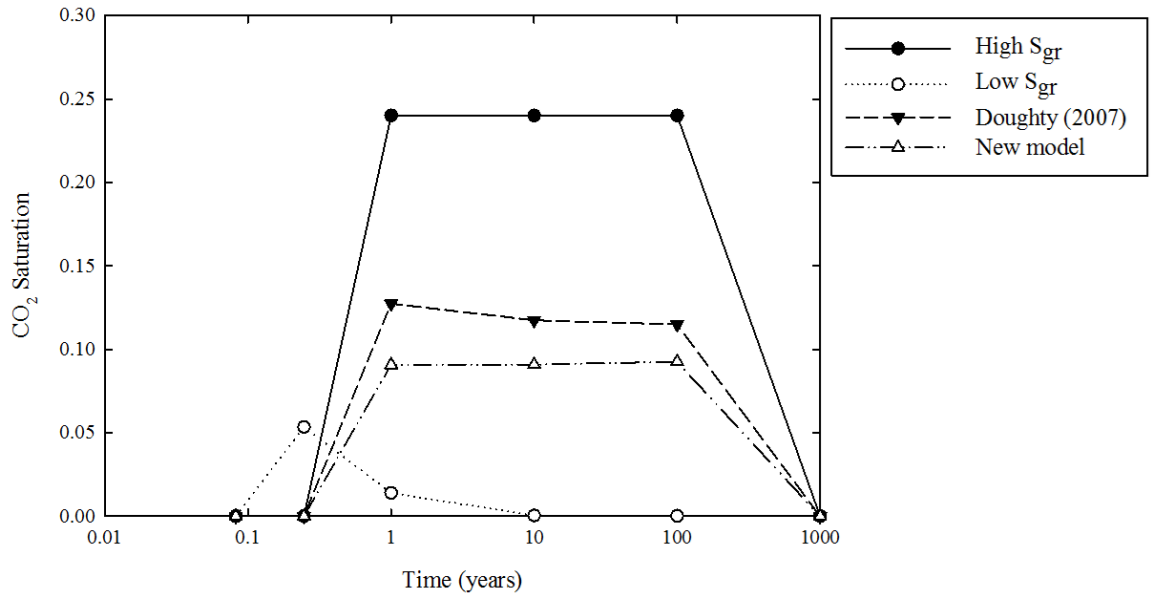

Figure 5.9 Plot of CO_2 saturation over time at a depth of 700 m at the center of the simulation grid.

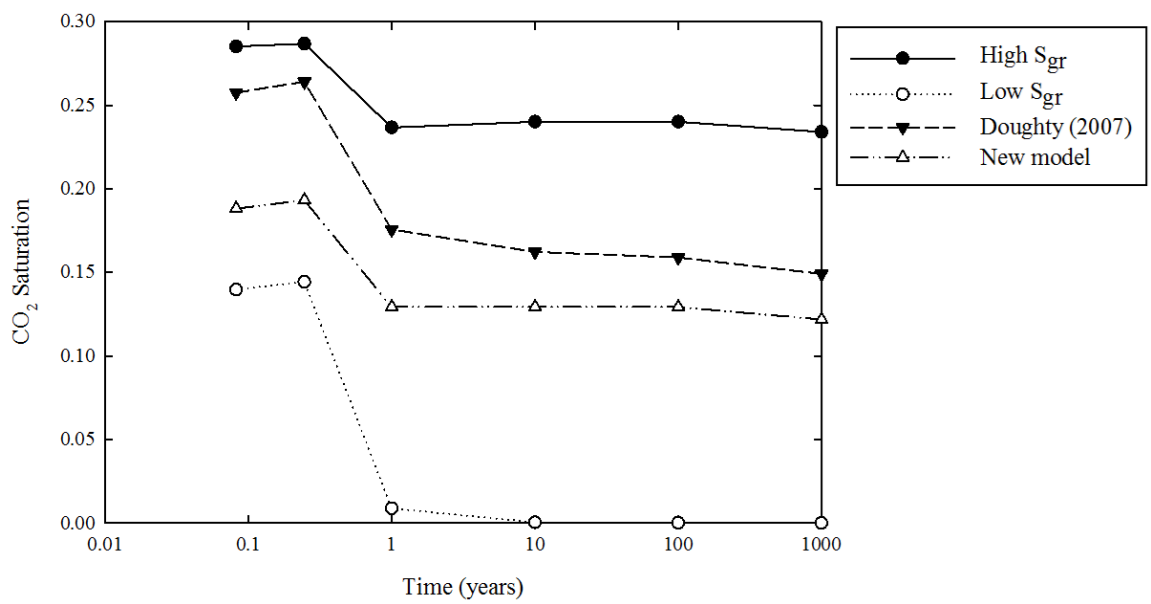

Figure 5.10 Plot of CO_2 saturation over time at a depth of 900 m at the center of the simulation grid.

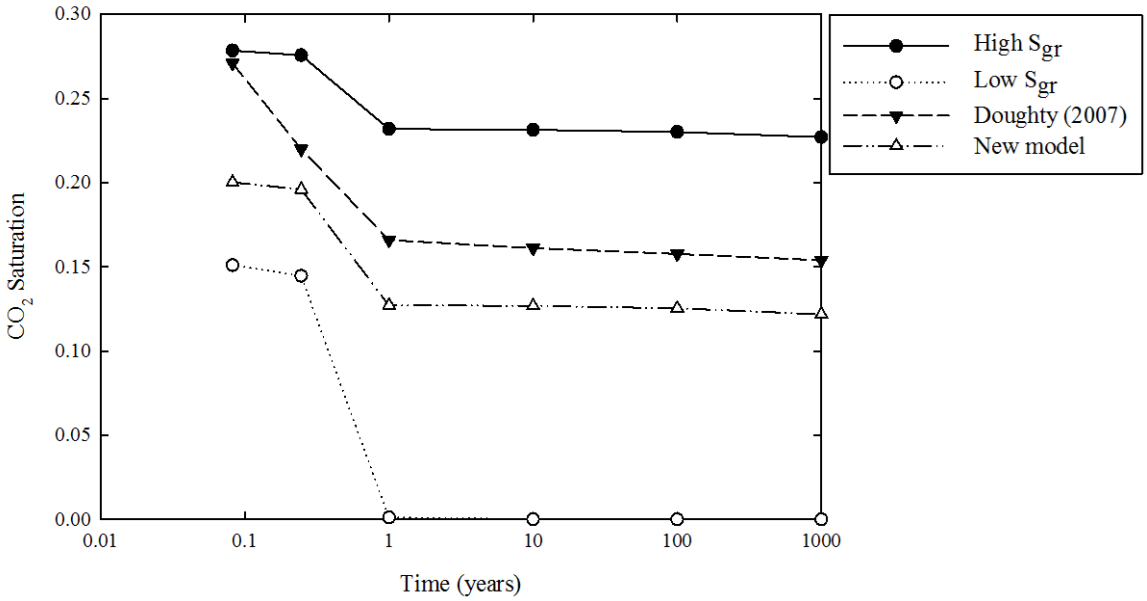

Figure 5.11 Plot of CO_2 saturation over time at 1,000 m depth at a radius of100 m from.

5.3 Three-dimensional simulations

For the third assessment of the new model, a 3-dimensional model of CO_2 injection and storage into a heterogeneous geologic formation was set up and run three different times each using three different sets of characteristic curves. The characteristic curve parameters were kept consistent and the behavior of the CO_2 plume confirms the mobilities expected from the shape of the characteristic curves. The purpose of these simulations was to explore the effect the characteristic curves have on CO_2 plume mobility.

5.3.1. Modeling approach

The 3-dimensional model considers a pilot-scale CO_2 injection and storage in a 3 km by 3 km by 100 m thick formation. The model was discretized into 20 layers, each containing 900 grid-blocks. The temperature of the formation was 50° C at the top and 50.6° C at the bottom, representing a formation at a depth range of 1000- 1100 m following a geothermal gradient of 25° C/ km. The pressure of the formation at the top was 1.18 MPa and 1.28 MPa at the bottom. The top 4 layers represented a less permeable zone. The model was initially fully saturated with brine. CO_2 was injected at a rate of 1000 tons/day for 20 years, and then simulation time continued to 100 years. The properties of the materials used for the model are shown in table 5.5. It is important to note that the permeability for the materials was the base value for which the permeability modifiers were applied to in order create a heterogeneous permeability field.

Hydraulic property	Value for storage formation	Value for confining layer
Rock grain density	2300 kg m^{-3}	2600 kg m^{-3}
Porosity	0.15	0.1
Mean x- y- permeability	1.0E-14 m^2	1.0E-17 m^2
Mean z- permeability	1.0E-16 m^2	1.0E-17 m^2

Table 5.5: Hydraulic properties for the materials used in the 3-dimensional model.

5.3.2. Generation of stochastically heterogeneous permeability modifiers

In order to represent a heterogeneous grid, each grid-block was assigned a permeability modifier which was a value multiplied to the intrinsic permeability for that grid-block. The permeability modifiers were generated using the Geostatistical Software Library (GSLIB) (Deutsch and Journel 1992) routine within iTOUGH2 (Finsterle 2000)- a computer program that provides inverse modeling capabilities for the TOUGH2 codes. A heterogeneous, random, spatially correlated field of permeability modifiers was generated using the sequential Gaussian simulation subroutine, then mapped onto the TOUGH2 grid. Synthetic values for the spherical semivariogram model parameters were chosen in order to generate a grid to represent long, lateral interbedded lenses of high-permeability sands and low-permeability shales. The permeability modifiers ranged from a value of 0.0575X to 40.7X. Figure 5.12 shows the permeability modifier grid used for the 3-dimensional simulations.

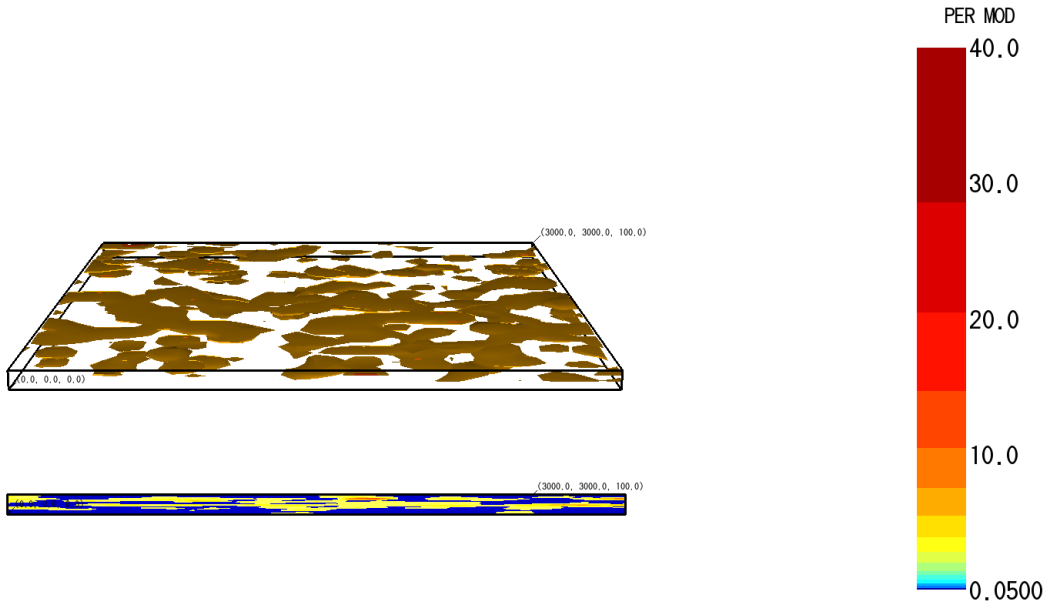

Figure 5.12 Permeability modifiers mapped onto TOUGH2 grid using iTOUGH2 GSLIB.

5.3.3. Characteristic curves

The characteristic curve parameters for the model were chosen to create reasonably shaped curves, and remained consistent between the three different simulations ran using different characteristic curves. The parameters for the relative permeability curves are shown in table 5.6, while examples of the relative permeability curves are plotted in figures 5.13a-c. The three cases considered are 1) a hysteretic simulation using the linear trapping equation, 2) a hysteretic simulation using the trapping model by Land 1968, and 3) a non-hysteretic version of the Charbeneau 2007 relative permeability and 1980 van Genuchten capillary pressure functions. It is apparent from the shape of the curves that the non- hysteretic relative permeability function will predict the least mobile CO_2 plume while the hysteretic model using the linear trapping

equation will predict the most mobile CO_2 plume. Due to the nature of the Land 1968 trapping model, higher amounts of residual CO_2 saturations are calculated at lower turning point CO_2 saturations. This also brings the main wetting phase drainage curve downwards considering that the value of residual gas saturation is constantly updated during wetting phase drainage.

Model parameter	**Case 1**	**Case 2**	**Case 3**
M	0.547	0.547	0.547
S_{lr}	0.2	0.2	0.2
f_r	0.3125		
S_{nr} max	-	0.25	-
S_{nr}	-	-	0.25

Table 5.6: Non-wetting phase relative permeability curve parameters for the 3 3-dimensional simulation cases.

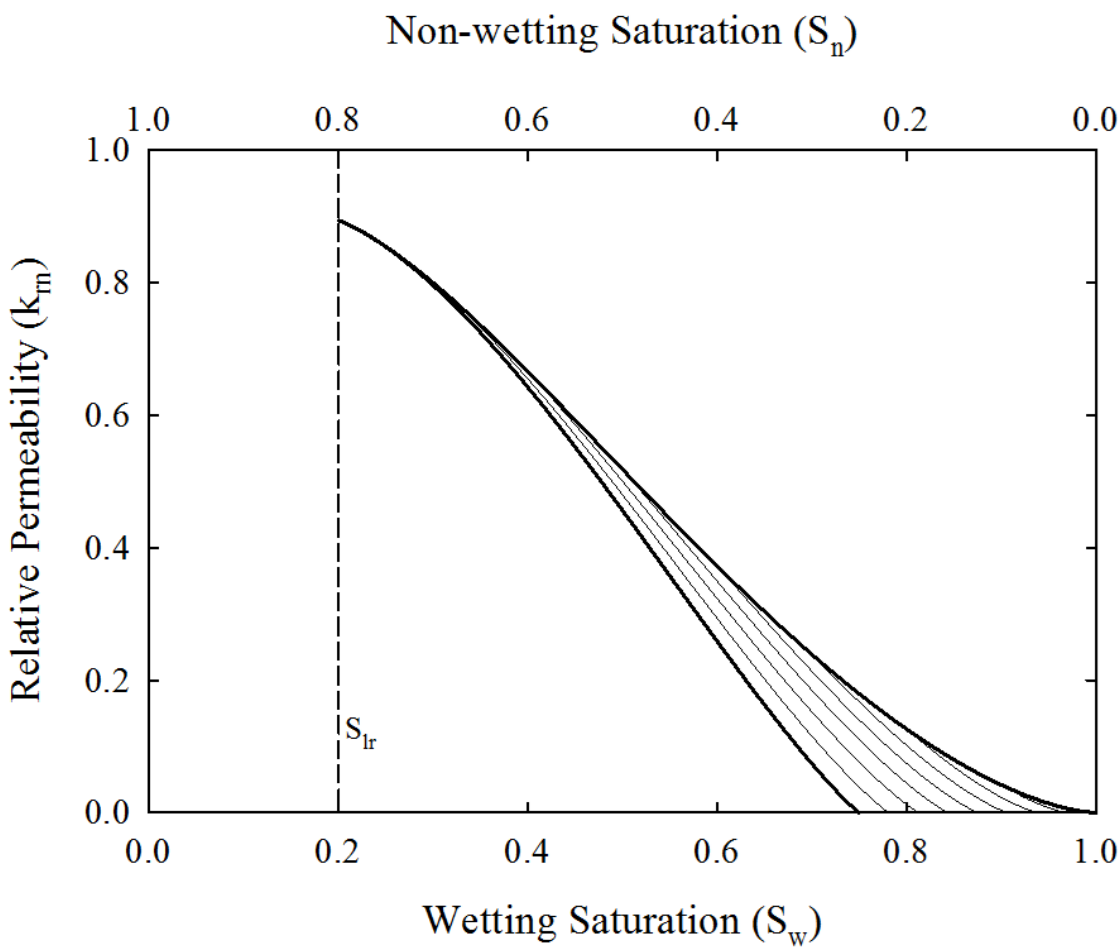

Figure 5.13 Non-wetting phase relative permeability curves for Case 1(a).

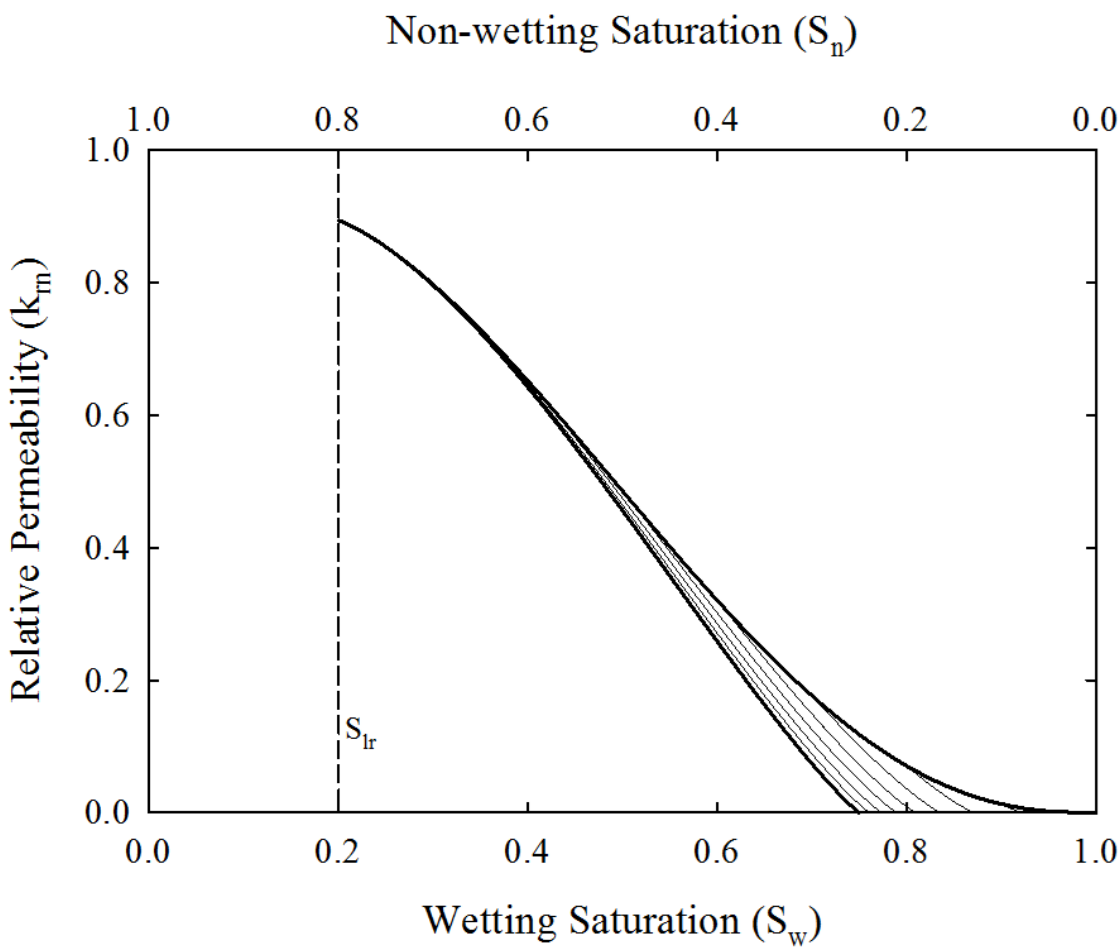

Figure 5.13 Non-wetting phase relative permeability curves for Case 2(b).

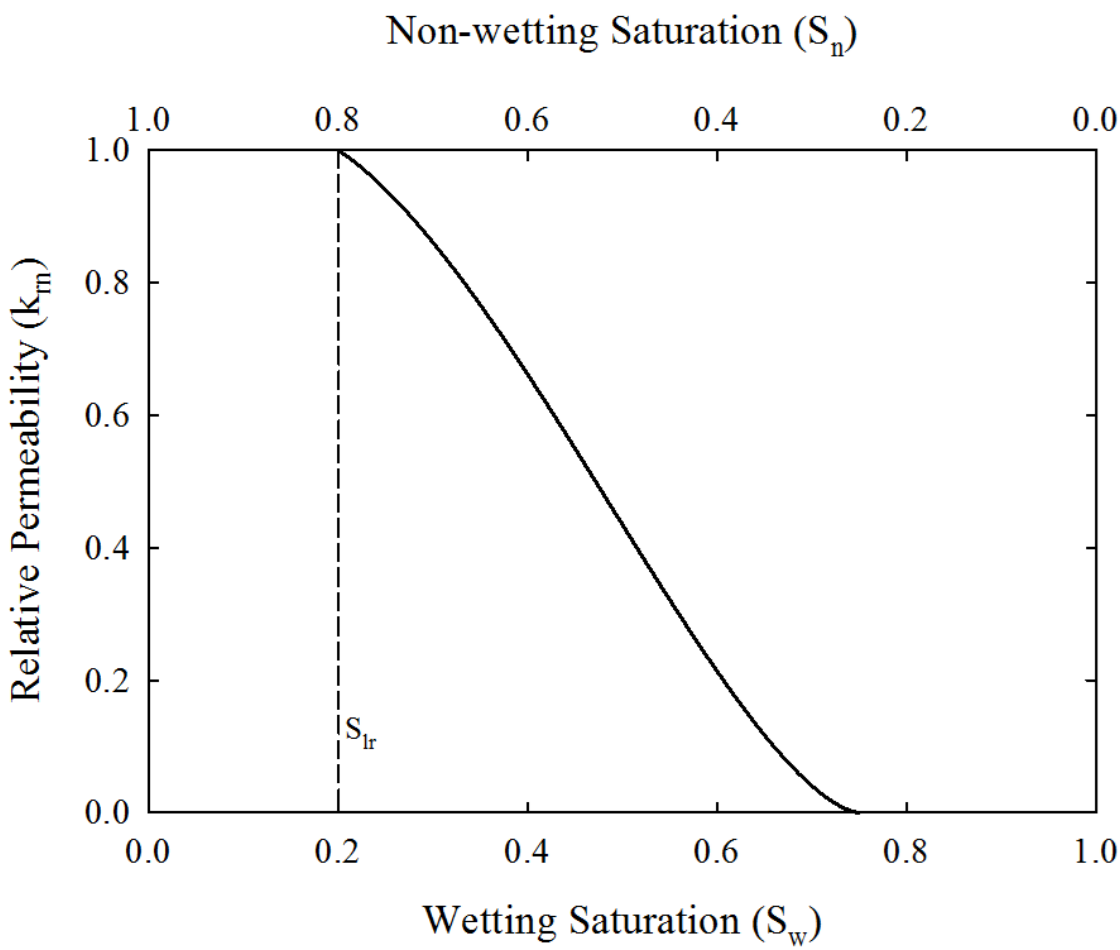

Figure 5.13 Non-wetting phase relative permeability curves for Case 3(c).

5.3.4. Results and Discussion

The results of the three simulations (figure 5.14) represent CO_2 plume mobilities that would be expected from examining plots of the characteristic curves. Case 1 with the hysteretic characteristic curves using the linear trapping model shows the most mobile CO_2 plume, while case 3 using the non-hysteretic characteristic curves represents the least mobile CO_2 plume. Case 2 using the hysteretic characteristic curves using the Land 1968 trapping model shows a CO_2 plume of intermediate mobility. The results confirm that the new hysteretic model can perform as expected for 3-dimensional simulations. It is apparent that the numerical nature of the characteristic curves has a significant impact on the overall mobility of the CO_2 plume and therefore it is necessary to consider realistic parameters for characteristic curves used.

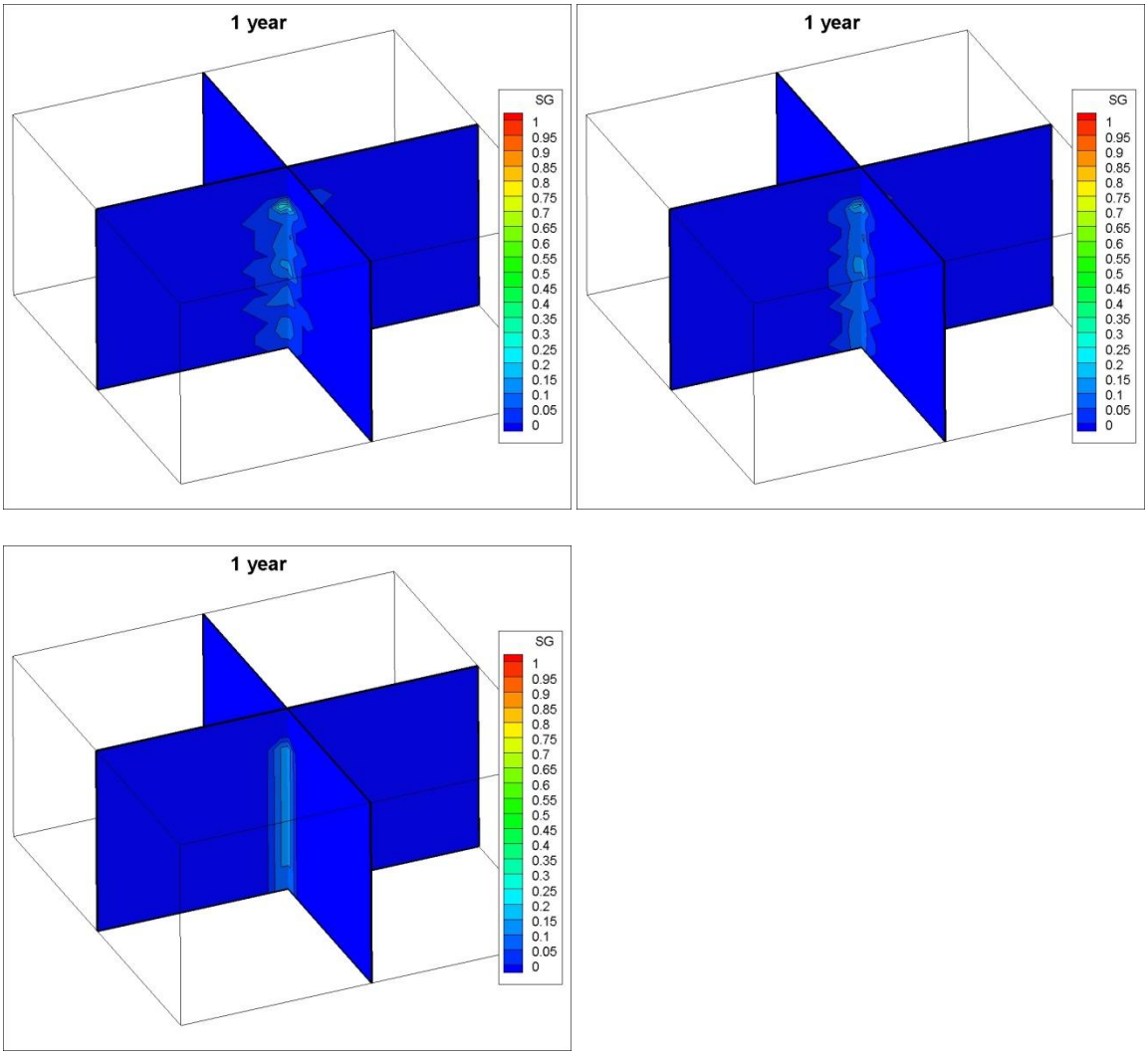

Figure 5.14 (a-c) Results from the 3-D simulations using a hysteretic model using the linear trapping model (top left), hysteretic model using the Land trapping model (top right), and a non-hysteretic model (bottom).

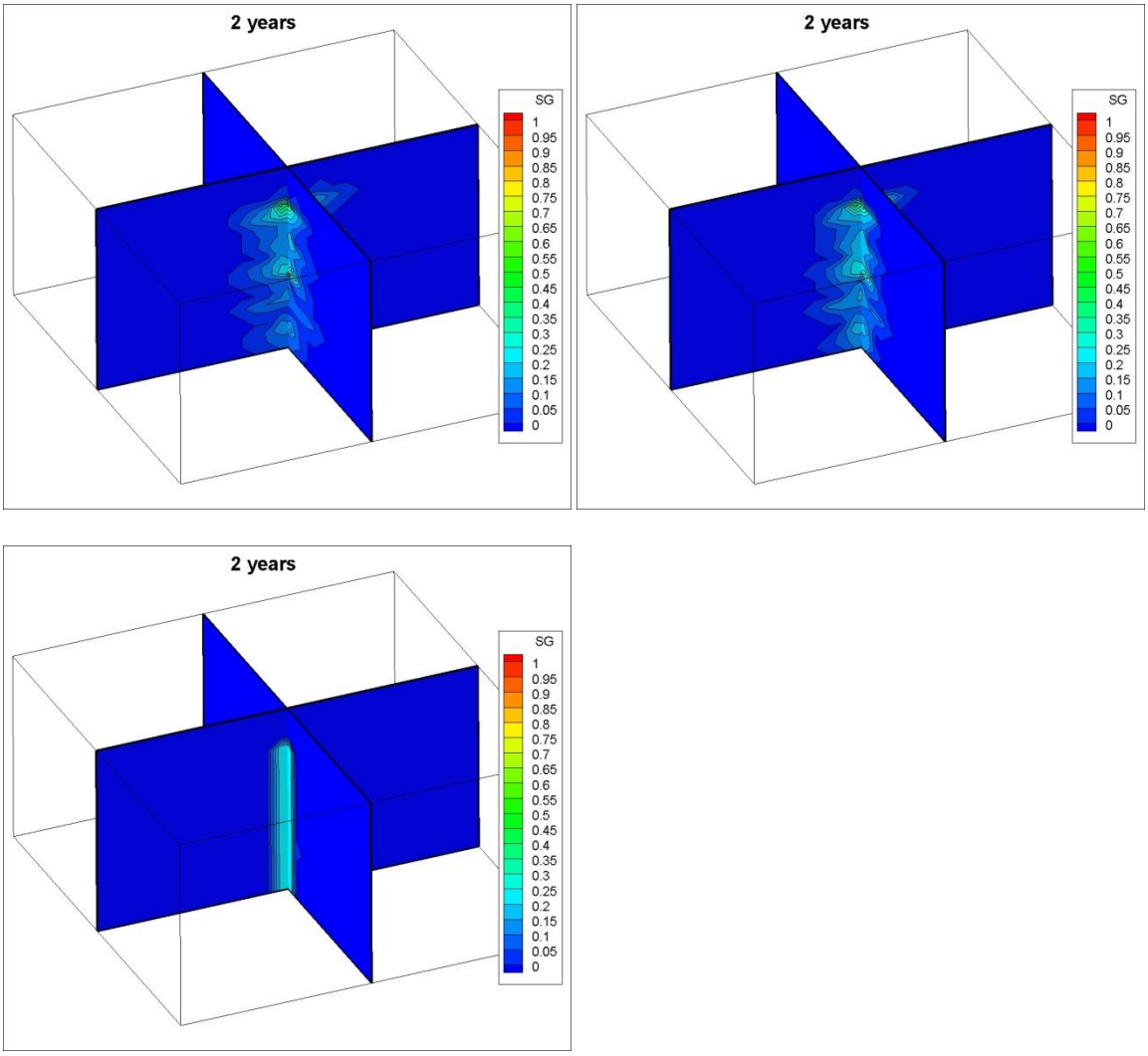

Figure 5.14 (d-f) Results from the 3-D simulations using a hysteretic model using the linear trapping model (top left), hysteretic model using the Land trapping model (top right), and a non-hysteretic model (bottom).

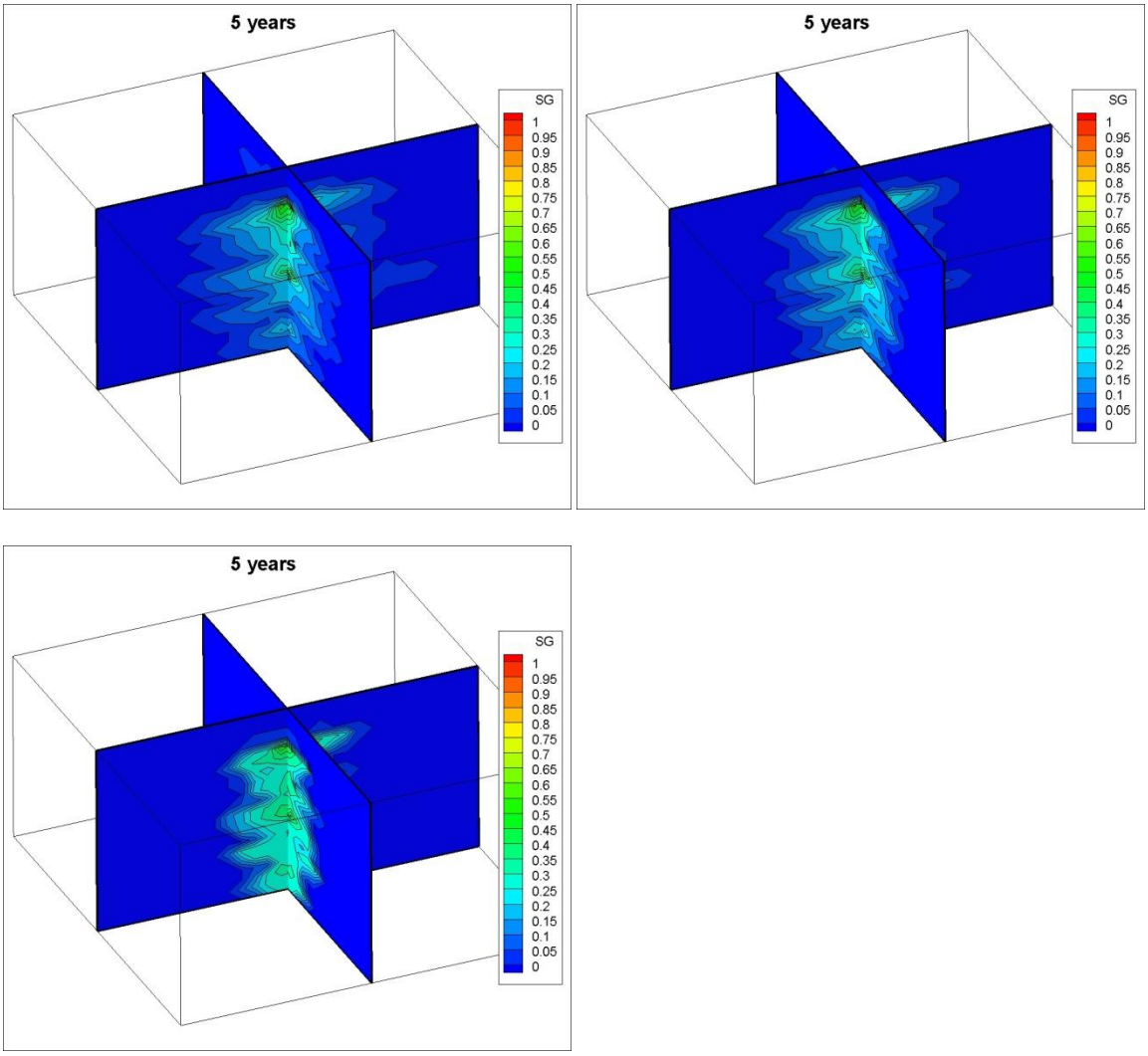

Figure 5.14 (h-j) Results from the 3-D simulations using a hysteretic model using the linear trapping model (top left), hysteretic model using the Land trapping model (top right), and a non-hysteretic model (bottom).

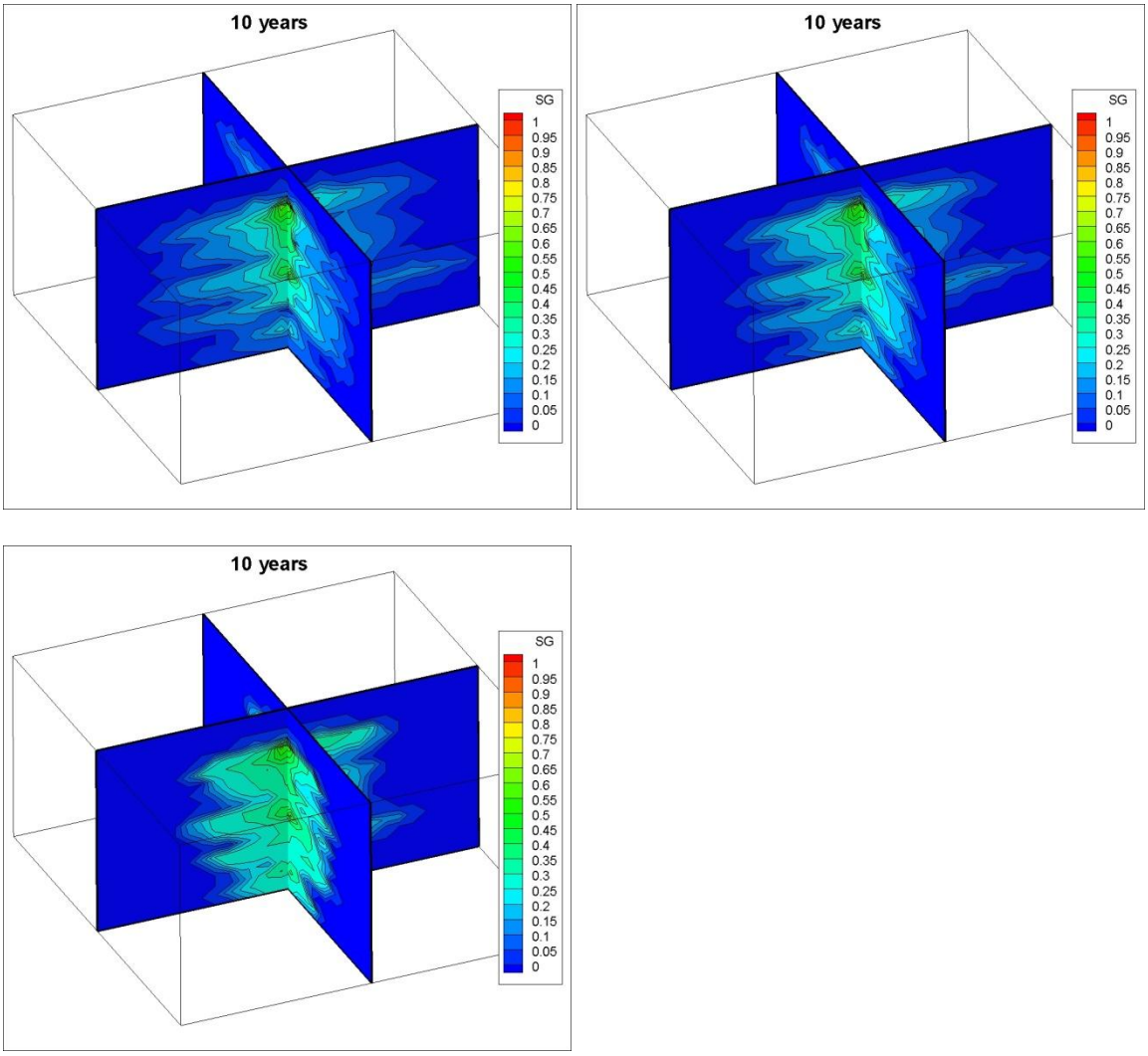

Figure 5.14 (k-m) Results from the 3-D simulations using a hysteretic model using the linear trapping model (top left), hysteretic model using the Land trapping model (top right), and a non-hysteretic model (bottom).

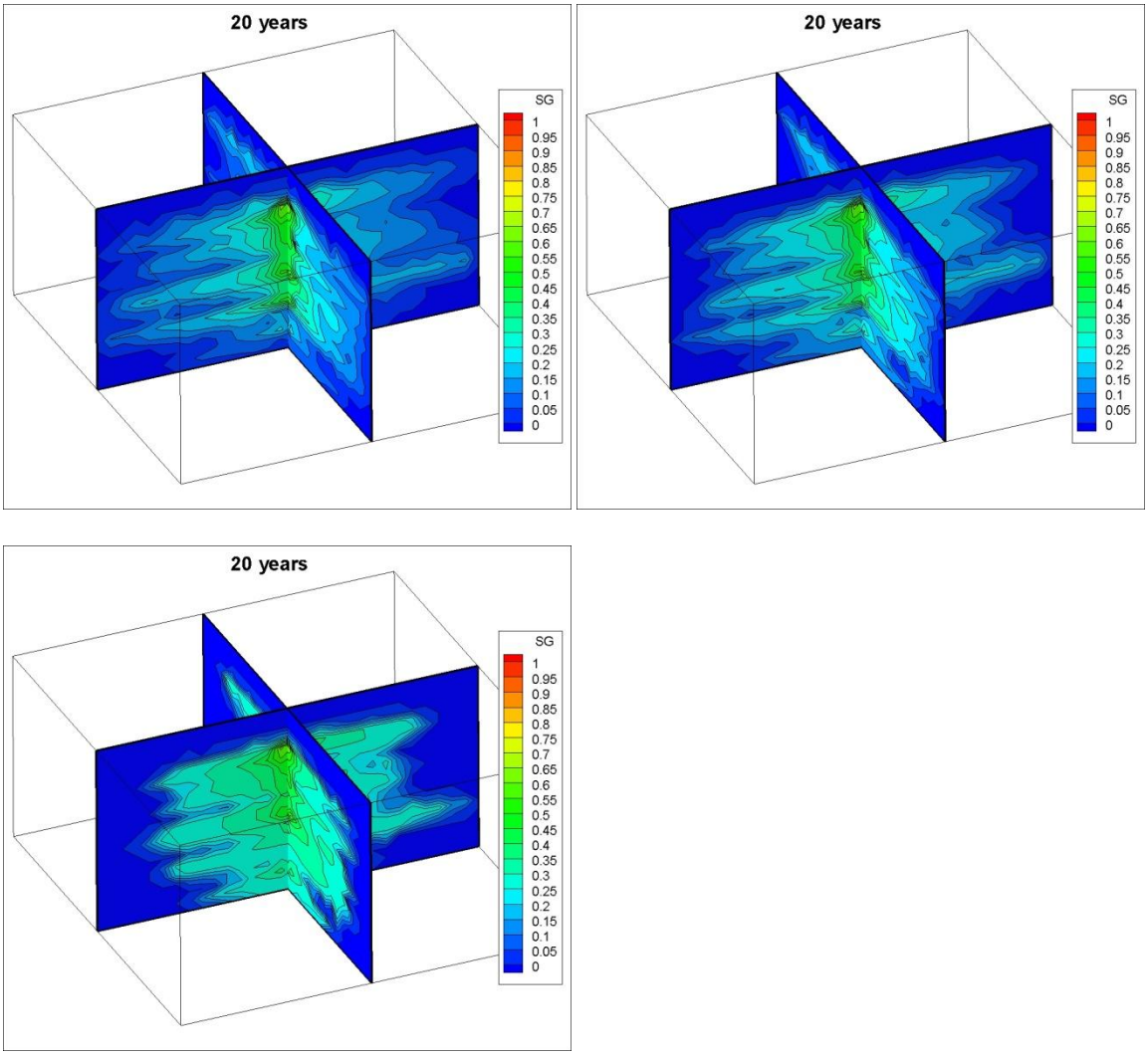

Figure 5.14 (n-p) Results from the 3-D simulations using a hysteretic model using the linear trapping model (top left), hysteretic model using the Land trapping model (top right), and a non-hysteretic model (bottom).

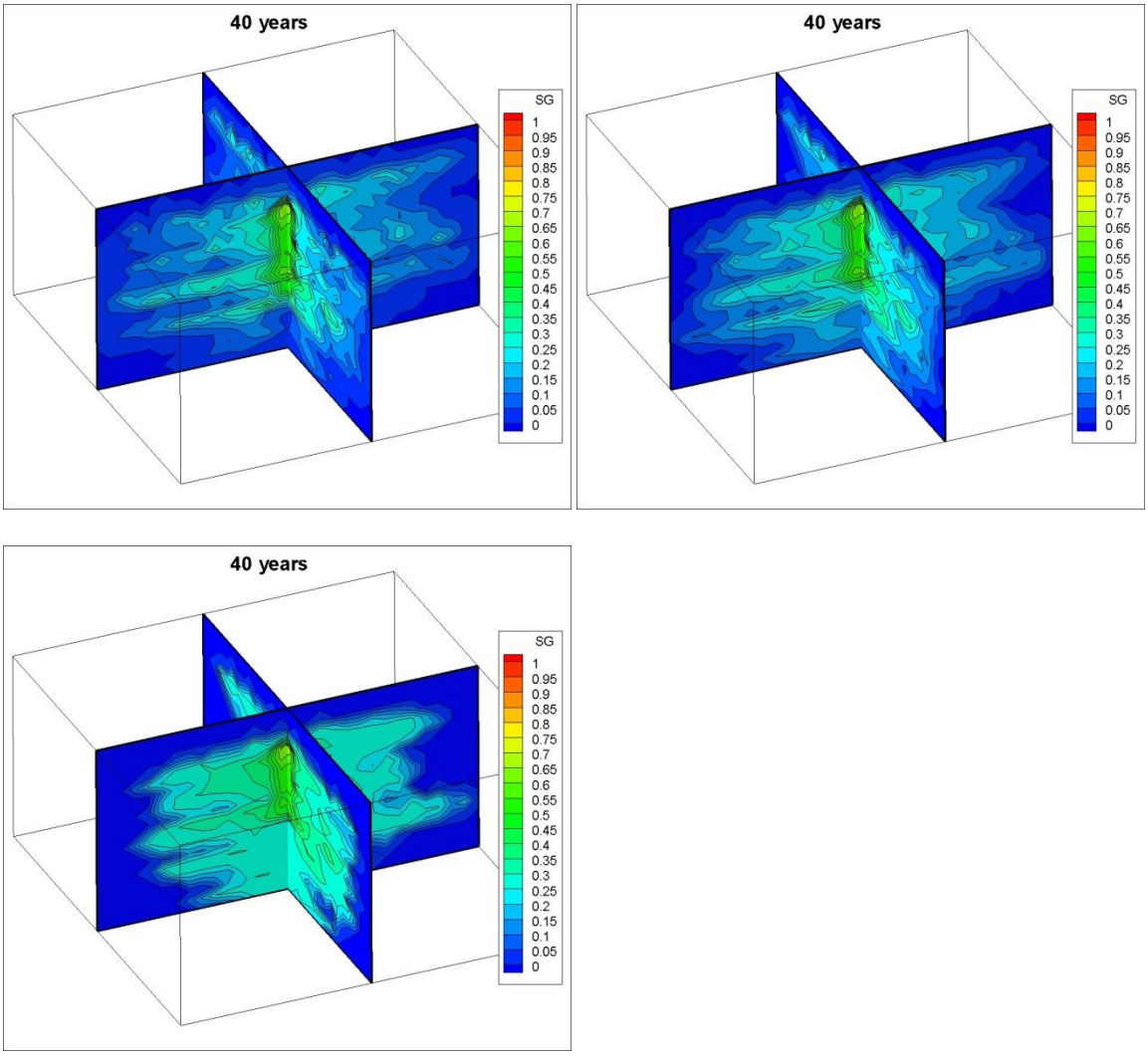

Figure 5.14 (q-s) Results from the 3-D simulations using a hysteretic model using the linear trapping model (top left), hysteretic model using the Land trapping model (top right), and a non-hysteretic model (bottom).

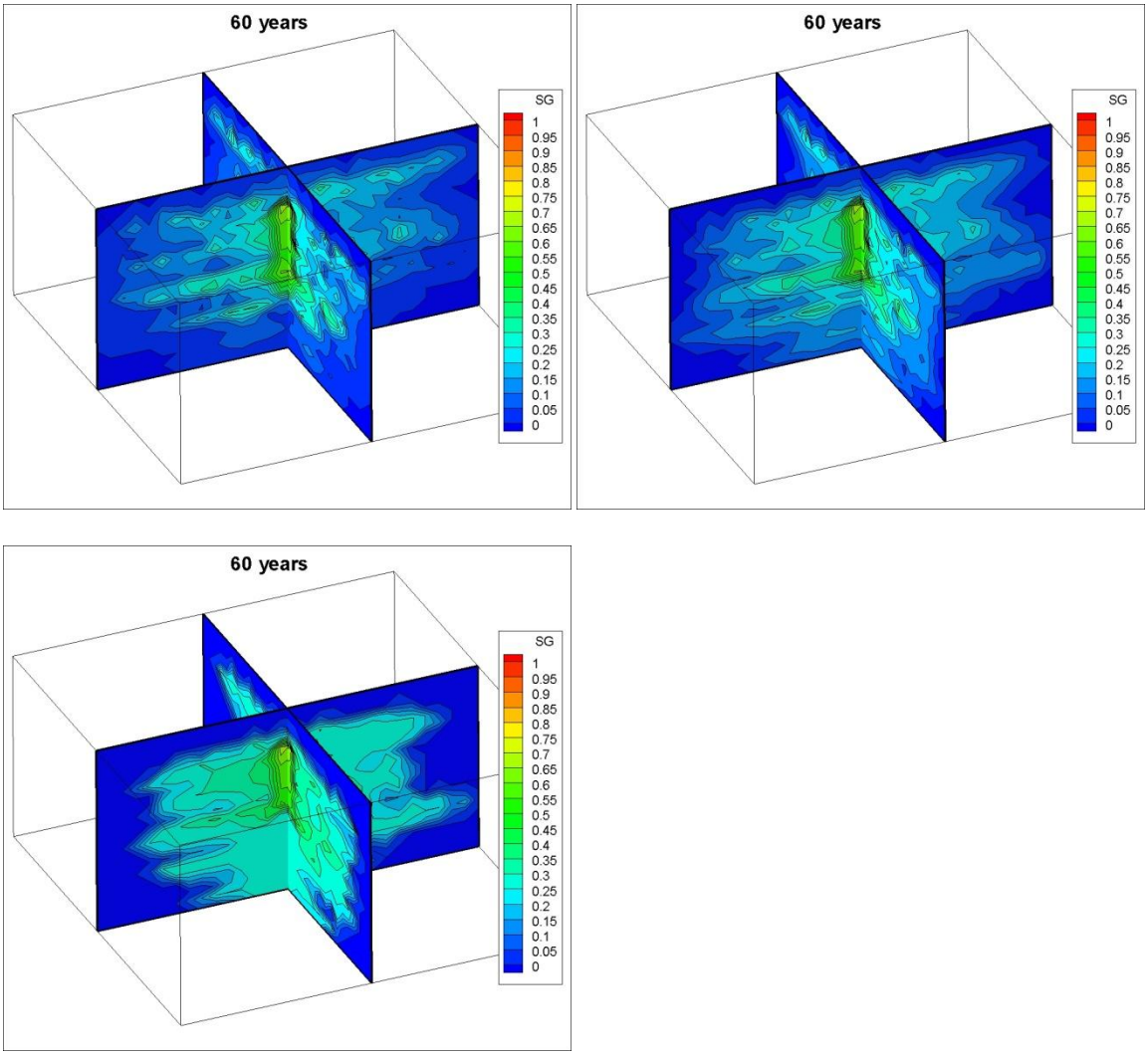

Figure 5.14 (t-v) Results from the 3-D simulations using a hysteretic model using the linear trapping model (top left), hysteretic model using the Land trapping model (top right), and a non-hysteretic model (bottom).

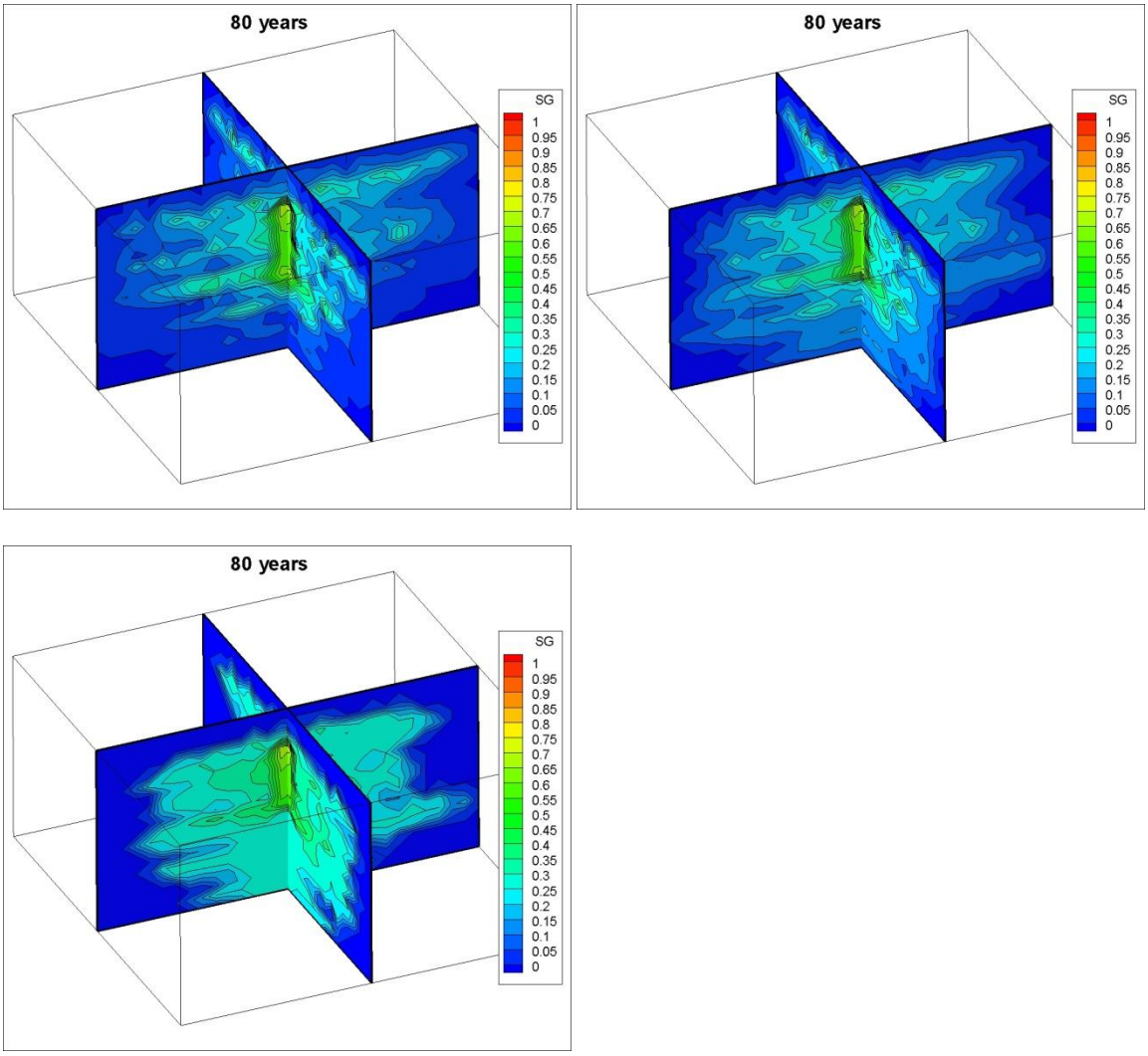

Figure 5.14 (w-y) Results from the 3-D simulations using a hysteretic model using the linear trapping model (top left), hysteretic model using the Land trapping model (top right), and a non-hysteretic model (bottom).

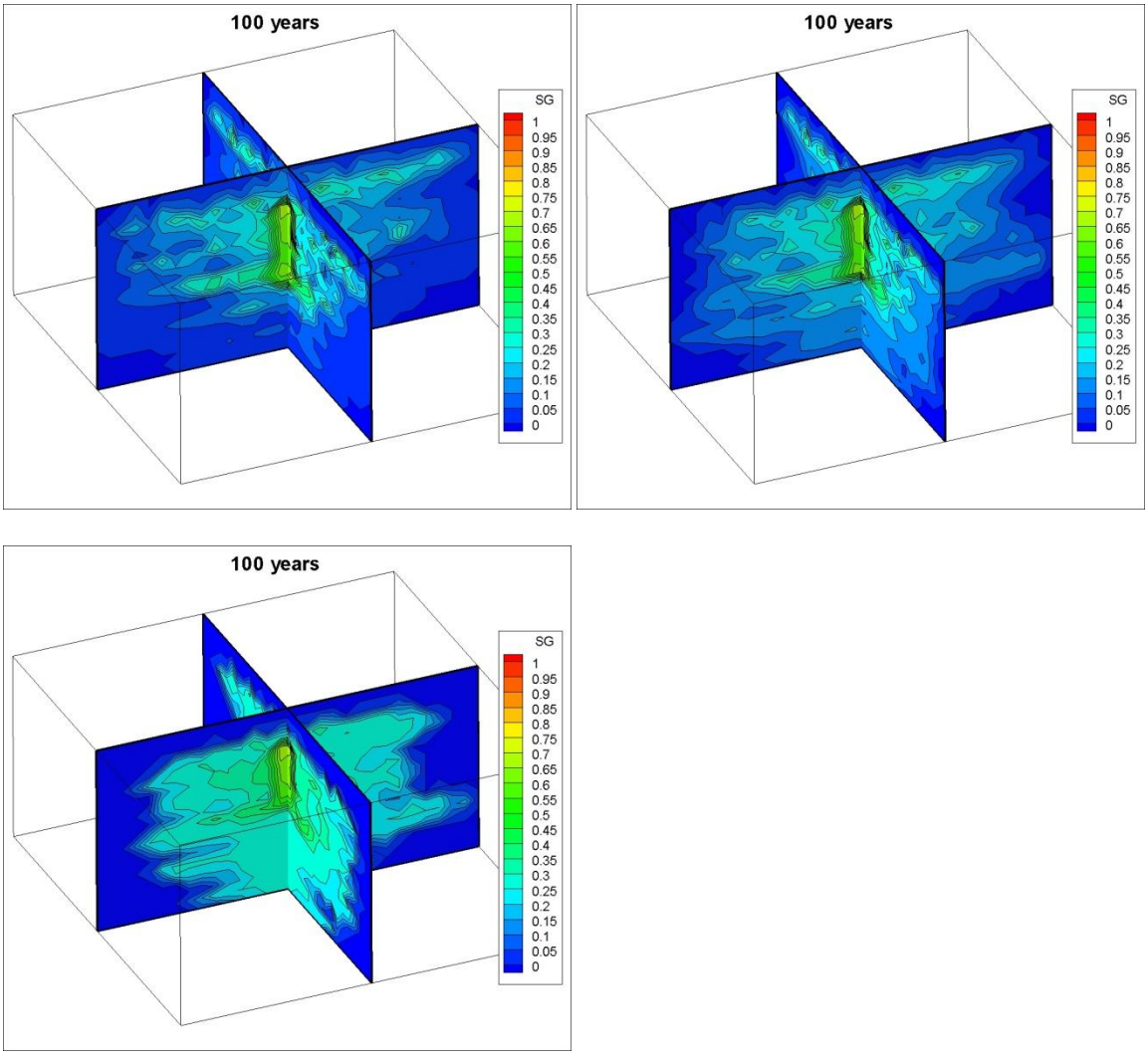

Figure 5.14 (z-ab) Results from the 3-D simulations using a hysteretic model using the linear trapping model (top left), hysteretic model using the Land trapping model (top right), and a non-hysteretic model (bottom).

5.4 Recommended work

The characteristic curves in a numerical simulation have a significant effect on the mobility of fluids as they migrate the subsurface. Multiphase relationships for relative permeability-saturation and capillary pressure-saturation for supercritical CO_2 and brine at reservoir temperatures and pressures need to be further investigated in order to improve the accuracy of numerical models. Relationships between initial- and residual-CO_2 saturations for supercritical CO_2 – brine mixtures could be explored — similar to the study published by Johnston and Adamski (2005). This work may allow for more accurate use of hysteretic characteristic curve parameters used in numerical simulations of CO_2 injection and migration.

6.0 CONCLUSIONS

The use of hysteretic characteristic curves greatly impacts the results of numerical simulations of multiphase flow by controlling the mobility of the fluids. The most important part of a hysteretic characteristic curve is the calculation of a variable value of residual saturation, which represents the saturation of the non-wetting phase that has become immobilized due to capillary forces.

A new, efficient and straight-forward hysteretic model is described to simulate the trapping processes during multiphase flow simulation. The numerical nature of the new model ensures continuously differentiable saturation turning-points which eases performance in numerical codes such as TOUGH2. An advantage of this new method of tracking hysteresis in the multiphase flow characteristic curves is the fact that there is no need for additional characteristic curve parameters. The new hysteretic model is capable of irreversible saturation paths using the same number of parameters that a simple non-hysteretic model would employ.

The new model was assessed by comparison to experimental results and published simulation results, as well as through the comparison of various non-hysteretic characteristic curve approaches for both homogeneous and heterogeneous grids. The results confirm that the new model performs favorably is capable of reproducing the essential features of more complex hysteretic models used for multiphase modeling.

REFERENCES

Alley, R., T. Berntsen, N.L. Bindoff, Z. Chen, A. Chidthaisong, P. Friedlingstein, J. Gregory,G. Hegerl, M. Heimann, B. Hewitson, B. Hoskins, F. Joos, J. Jouzel, V. Kattsov, U. Lohmann, M. Manning, T. Matsuno, M. Molina, N. Nicholls, J. Overpeck, D. Qin, G. Raga, V. Ramaswamy, J. Ren, M. Rusticucci, S. Solomon, R. Somerville, T.F. Stocker, P. Stott, R.J. Stouffer, P. Whetton, R.A. Wood, D. Wratt, 2007, Climate change 2007: The physical science basis, Summary for policymakers, IPCC WGI Fourth Assessment Report, Intergovernmental panel on climate change, Cambridge University Press, Cambridge, U.K.

Burdine, N.T., 1953, Relative permeability calculations from pore size distribution data, Trans. Am. Inst. Min. Meterol. Eng., 198, 71-78

Charbeneau, R., 2007, LNAPL Distribution and Recovery Model (LDRM) Volume 1: Distribution and Recovery of Petroleum Hydrocarbon Liquids in Porous Media, American Petroleum Institute API Publication 4760.

Deutsch, C.V., and A.G. Journel, 1998, GSLIB: Geostatistical software library and user's guide: Oxford University Press, New York, 2nd ed., p. 368

Doughty, C., 2007, Modeling geologic storage of carbon dioxide: comparison of non-hysteretic and hysteretic characteristic curves, Energy Conversion and Management, 48, 1768-1781.

Doughty, C., 2010, personal communication with Christine Doughty.

Fagerlund, F., A. Niemi, and T.H. Illangasekare, 2008, Modeling of nonaqueous phase liquid (NAPL) migration in heterogeneous saturated media: Effects of hysteresis and fluid immobility in constitutive relations, Water Resources Research, 44, W03409.

Falta, R.W., K. Pruess, S. Finsterle, and A. Battistelli, 1995, T2VOC user's guide, Rep. LBL-36400, Lawrence Berkeley National Laboratory, Berkeley, California.

Finsterle, S., 2000, iTOUGH2 user's guide, Rep. LNBL-40040, 2nd rev., Lawrence Berkeley National Laboratory, Univ. of Calif., Berkeley, Calif.

Johnston, C., and M. Adamski, 2005, Relationship between initial and residual LNAPL saturation for different soil types, Proceedings of the 2005 Petroleum Hydrocarbons and Organic Chemicals in Groundwater®: Prevention, Assessment, and Remediation Conference. 17-19 August, Costa Mesa, 29-42.

Johnston, C., 2010, personal communication with Colin Johnston.

Juanes, R., E.J. Spiteri, F.M. Orr Jr., and M.J. Blunt, 2006, Impact of relative permeability hysteresis on geological CO_2 storage, Water Resources Research, 42, W12418.

Juanes, R., C.W. MacMinn, and M.L. Szulczewski, 2010, The footprint of the CO_2 plume during carbon dioxide storage in saline aquifers: storage efficiency for capillary trapping at the basin scale, Transp Porous Med, 82, 19-30.

Kaluarachchi, J.J., and J.C. Parker, 1992, Multiphase flow with a simplified model for oil entrapment, Transport in Porous Media, 7, 1-14.

Kueper, B.H., D. Redman, R.C. Starr, S. Reitsma, and M. Mah, 1993, A field experiment to study the behavior of tetrachloroethylene below the water table: spatial distribution of residual and pooled DNAPL, Ground Water, 31: 5, 756-766.

Land, Carlon S., 1968, Calculation of imbibition relative permeability for two- and three-phase flow from rock properties, Transactions, 243, 149-156.

Lenhard, R.J., and J.C. Parker, 1987, A model for hysteretic constitutive relations governing multiphase flow: 2. Permeability-saturation relations, Water Resources Research, 23:10, 2197-2206.

Lenhard, R.J., and J.C. Parker, 1987, Measurement and prediction of saturation-pressure relationships in three-phase porous media systems, Journal of Contaminant Hydrology, 1, 407-424.

Lenhard, R.J., 1992, Measurement and modeling of three-phase saturation-pressure hysteresis, Journal of Contaminant Hydrology, 9, 243-269.

Mualem, Y., 1976, A new model for predicting the hydraulic conductivity of unsaturated porous media, Water Resources Research, 12:6, 513-522.

Mualem, Y., 1984, A modified dependent-domain theory of hysteresis, Soil Science, 137:5, 283-291.

NETL, 2007, Carbon Sequestration Atlas of the United States and Canada, U.S. Department of Energy, National Energy Technology Laboratory. Available from http://www.netl.doe.gov/technologies/carbon_seq/refshelf/atlas/ATLAS.pdf

Niemi, A., and G.S. Bodvarsson, 1988, Preliminary capillary hysteresis simulations in fractured rocks, Yucca Mountain, Nevada, Journal of Contaminant Hydrology, 3, 277-291.

Parker, J.C., and R.J. Lenhard, 1987, A parametric model for constitutive properties governing multiphase flow in porous media, Water Resources Research, 23: 4, 618-624.

Pruess, K., C. Oldenburg, and G. Moridis, 1999, TOUGH2 user's guide, version 2.0, Rep. LBNL-43134. Berkeley: Lawerence Berkeley National Laboratory.

Pruess, K. and A. Battistelli, 2002, TMVOC, A numerical simulator for three-phase non-isothermal flows of multicomponent hydrocarbon mixtures in saturated-unsaturated heterogeneous media, LBNL-49375, Lawrence Berkeley National Laboratory, Berkeley, CA.

Pruess, K., 2005, ECO2N: A TOUGH2 fluid property module for mixtures of water, NaCL, and CO_2, LBNL-57952, Earth Sciences Division, Lawrence Berkeley National Laboratory, University of California, Berkeley, CA.

Steffy, D.A., D.A. Barry, and C.D. Johnston, 1997, Influence of antecedent moisture content on residual LNAL saturation, Soil and Sediment Contamination: An International Journal, 6: 2, 113-147.

Van Geel, P.J., and S.D. Roy, 2002, A proposed model to include a residual NAPL saturation in a hysteretic capillary pressure-saturation relationship, Journal of Contaminant Hydrology, 58, 79-110.

van Genuchten, M.T., 1980, A closed-form equation for predicting the hydraulic conductivity of unsaturated soils, Soil Sci. Soc. Am. J., 44, 892-898.

van Genuchten, M.T. and D.R. Nielsen, 1985, On describing and predicting the hydraulic properties of unsaturated soils, Annales Geophysicae, 3:5, 615-628.